



Development of Modular Steel Jacket for Offshore Windfarms

(JABACO)

A large, abstract graphic of blue and white waves occupies the bottom half of the page, creating a dynamic and modern feel.

EUR 30457 EN

Development of Modular Steel Jacket for Offshore Windfarms (JABACO)

European Commission

Directorate-General for Research and Innovation

Directorate D – Clean Planet

Unit D.3 — Low Emission Future Industries

Contact Hervé Martin

E-mail RTD-PUBLICATIONS@ec.europa.eu

European Commission

B-1049 Brussels

Manuscript completed in 2019.

This document has been prepared for the European Commission however it reflects the views only of the authors, and the Commission cannot be held responsible for any use which may be made of the information contained therein.

More information on the European Union is available on the internet (<http://europa.eu>).

Luxembourg: Publications Office of the European Union, 2020

PDF ISBN 978-92-76-25387-7 ISSN 1831-9424 doi:10.2777/147264 KI-NA-30-457-EN-N

© European Union, 2020.

Reuse is authorised provided the source is acknowledged. The reuse policy of European Commission documents is regulated by Decision 2011/833/EU (OJ L 330, 14.12.2011, p. 39).

For any use or reproduction of photos or other material that is not under the EU copyright, permission must be sought directly from the copyright holders.

All pictures, figures and graphs © Rina Consulting – Centro Sviluppo Materiali s.p.a., RFSR-CT-2015-00024 (JABACO)

Research Fund for Coal and Steel

Development of Modular Steel Jacket for Offshore Windfarms

(JABACO)

Giuliana ZILLI (coordinator)

Rina Consulting – Centro Sviluppo Materiali s.p.a.
Via di Castel Romano 100 00128 Rome - Italy

Philippe THIBAUX

Onderzoekscentrum Voor Aandwending van Staal N.V.
President JF Kennedylaan 3 BE-9060 Zelzate - Belgium

Spyros A. KARAMANOS

University of Thessaly
Argonafton Filellinon GR-38221 Volos - Greece

Marc VOßBECK

Ramboll IMS Ingenieurgesellschaft
Stadtdeich 7 - 20097 Hamburg - Germany

Spyros MAVRAKOS

National Technical University of Athen
Heron Polytechniou 9 Zographou Campus GR-15780 Athens - Greece

Cristina RUIZ

Ingegneria y Diseno Europeo
CL Par Cientifico y Tecnologico de Gijon Edificio Idesa 2 ES-33203 Gijon - Spain

Grant Agreement RFSR-CT-2015-00024

01/07/2015 – 31/12/2018

Final Report

TABLE OF CONTENTS

TABLE OF CONTENTS	3
FINAL SUMMARY	7
WP1 - DETERMINATION OF LOADING CONDITIONS AND PRELIMINARY ANALYSIS.....	7
WP2 - MODULAR JACKET LOAD ANALYSIS	8
WP3 - DESIGN OF THE FOUNDATION OF THE MODULAR JACKET	9
WP4 - MANUFACTURING OF STANDARD COMPONENTS FOR TESTING	9
WP5 – EXPERIMENTAL INVESTIGATION ON SELECTED SCALED COMPONENTS.....	10
WP6 - FINITE ELEMENT SIMULATIONS ON THE STANDARD COMPONENTS.....	12
WP7 – IMPACT OF MODULARITY AND QUALITY/COST ANALYSIS.....	12
WP8 – DEVELOPMENT OF JABACO MANUAL AND DISSEMINATION OF RESULTS.....	13
SCIENTIFIC AND TECHNICAL DESCRIPTION OF THE RESULTS.....	14
PROJECT OBJECTIVES.....	14
WP1 - DETERMINATION OF LOADING CONDITIONS AND PRELIMINARY ANALYSIS.....	14
<i>Objectives and main outcomes</i>	14
TASK 1.1 MET-OCEAN DATA AND SOIL CONDITIONS	14
<i>Met-ocean data source</i>	15
<i>Statistical analysis of met-ocean and sea-level data</i>	15
<i>Extreme value analysis (univariate case)</i>	16
<i>Soil data</i>	17
TASK 1.2 SET-UP OF 8MW AND 10MW TURBINE MODEL	18
<i>8 MW wind turbine</i>	19
<i>10 MW wind turbine</i>	20
TASK 1.3 PRELIMINARY DESIGN OF MODULAR JACKET	22
<i>Jackets main dimensions</i>	22
<i>Modular Jackets geometries</i>	23
WP2 - MODULAR JACKET LOAD ANALYSIS	24
<i>Objectives and main outcomes</i>	24
TASK 2.1 FULLY-INTEGRATED TURBINE-MODULAR JACKET MODEL	24
<i>Integrated load simulation tool for 8MW turbine-jacket model</i>	24
<i>Integrated load simulation tool for 10MW turbine-jacket model</i>	25
TASK 2.2 TIME DOMAIN DYNAMIC ANALYSIS	25
<i>Analysis of 8 MW scenarios</i>	25
<i>Analysis of 10 MW scenarios</i>	27
TASK 2.3 DETERMINATION OF LONG-TERM HOT SPOT STRESS RANGE ANALYSIS	30
WP3 - DESIGN OF THE FOUNDATION OF THE MODULAR JACKET	32
<i>Objectives</i>	32
TASK 3.1 IDENTIFICATION OF THE MOST APPROPRIATE FOUNDATION SYSTEM.....	32
TASK 3.2 COMPREHENSIVE FE ANALYSIS OF SELECTED FOUNDATION SYSTEMS.....	34
TASK 3.3 FOUNDATION RESPONSE IN ACCOUNT OF DYNAMIC SOIL-STRUCTURE INTERACTION ..	36

TASK 3.4 DEVELOPMENT OF DESIGN CHARTS	37
WP4 - MANUFACTURING OF STANDARD COMPONENTS FOR TESTING	40
<i>Objectives and main outcomes</i>	40
TASK 4.1 DESIGN OF STANDARD COMPONENTS FOR TESTING	40
TASK 4.2 BASE MATERIAL PROCUREMENT	41
TASK 4.3 WELDING PROCEDURE SPECIFICATION AND QUALIFICATION OF JOINTS	41
<i>Simulation of WPS</i>	42
<i>Nondestructive Tests</i>	44
TASK 4.4 FABRICATION IMPROVEMENTS	45
WP5 – EXPERIMENTAL INVESTIGATION ON SELECTED SCALED COMPONENTS.....	48
<i>Objectives</i>	48
TASK 5.1 MATERIAL CHARACTERIZATION AND RESIDUAL STRESS MEASUREMENTS	48
<i>Base material characterization</i>	48
<i>Residual stresses</i>	49
<i>Hardness measurements</i>	50
<i>Stress raisers</i>	50
<i>Small scale fatigue tests on HFMI treated joints</i>	51
TASK 5.2 AND 5.3 FULL-SCALE TESTING	52
<i>Reference S-N curves</i>	53
<i>Out-of-plane bending</i>	54
<i>In-plane bending fatigue testing</i>	57
<i>Resonant fatigue testing</i>	61
WP6 - FINITE ELEMENT SIMULATIONS ON THE STANDARD COMPONENTS.....	64
<i>Objectives</i>	64
TASK 6.1 DEVELOPMENT OF FINITE ELEMENT MODELS OF THE STANDARD COMPONENTS	64
<i>Out-of-plane bending</i>	64
<i>In-plane bending</i>	65
<i>FE Model for resonance testing</i>	66
TASK 6.2 NUMERICAL SIMULATION OF EXPERIMENTAL RESULTS OF THE STANDARD COMPONENTS	68
<i>Out-of-plane bending</i>	68
<i>In-plane bending</i>	70
<i>Resonance testing</i>	71
TASK 6.3 NUMERICAL PARAMETRIC STUDY	76
<i>SCFs of modular jacket prefabricated joints</i>	76
<i>Influence of assembly imperfections</i>	79
WP7 – IMPACT OF MODULARITY AND QUALITY/COST ANALYSIS.....	82
<i>Objectives and main outcomes</i>	82
TASK 7.1 METHOD OF EXECUTION.....	82
<i>Horizontal Jacket</i>	82
<i>Vertical Jacket Methodology</i>	84
TASK 7.2 MODULARITY CONCEPT DEVELOPMENT	85
<i>Cost analysis model</i>	85

<i>Joints description</i>	87
TASK 7.3 INTEGRATION OF STRUCTURAL COMPONENT IN A QUALITY/COST AND OPTIMIZATION ANALYSIS	90
<i>Cost and Time parameters</i>	90
<i>Cost and time evaluation</i>	93
WP8 – DEVELOPMENT OF JABACO MANUAL AND DISSEMINATION OF RESULTS.....	96
<i>Objectives</i>	96
TASK 8.1 DEVELOPMENT OF JABACO MANUAL.....	96
TASK 8.2 DISSEMINATION OF RESULTS – DEDICATED WORKSOP.....	97
<i>Report from Genoa seminar</i>	97
<i>Report from Edinburgh seminar</i>	99
EXPLOITATION AND IMPACT OF RESEARCH RESULTS	100
<i>Publications and patents</i>	100
LIST OF FIGURES	102
LIST OF TABLES	106
LIST OF SYMBOLS AND ACRONYMS	108
REFERENCES	110

FINAL SUMMARY

WP1 - DETERMINATION OF LOADING CONDITIONS AND PRELIMINARY ANALYSIS

For all combinations of considered offshore locations and turbine sizes (Table 1), feasible jacket designs have been set up. The main and local dimensions have been chosen in view of

- Environmental conditions: wind wave and soil conditions (Task 1.1).
- Prevailing loads generated by the WTG for 8 and 10MW (Task 1.2)

Table 1 - Overview of offshore locations and turbine size.

Wind Turbine	Water depth/Location				
	20 m	30 m	40 m	50 m	60 m
	North Sea	North Sea	North Sea	North Sea	Mediterranean (seismic)
L4	L2	L3a	L3	L1	
8 MW			✓	✓	✓
10 MW	✓	✓	✓		

The choice in rated power 8MW and 10MW reflects the current offshore wind market situation and trend for increased rated powers to cut O&M costs. The models and corresponding controllers are setup in two independent aero-elastic simulation environments Flex5 and hGAST. The feasibility of conducting realistic and stable load simulations has been demonstrated through time series analysis according to IEC standards.

In terms of dimensions, the 10 MW wind turbine is naturally larger than the 8 MW wind turbine. This results in 14m larger rotor diameter and 12 m higher hub heights to assure the required blade tip clearance to the outer platform which leads to both increased thrust forces and longer lever arm, resulting in larger bending moments that need to be transferred into the ground by the foundation.

Both models show a stable behaviour over various wind speed regions as shown in the step response of Figure 1. However, the controller of the 8MW is tuned more aggressively resulting in a visible overshoot of the electrical power after each stepwise increase in mean wind speed before the curve rests at the new stable value. A more aggressive controller will ultimately induce more fatigue loads while achieving higher energy yield due to faster adaptation to changed wind conditions. Tuning of wind turbine controllers is a sophisticated task that each turbine manufacturer conducts carefully in order to balance between desired and undesired effects.

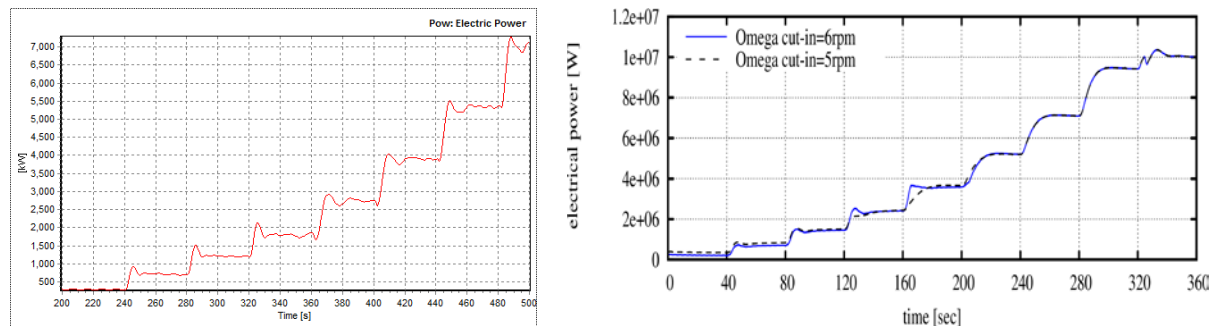


Figure 1 - time series of the electrical power for the step-up load case for the 8MW (left) and 10MW (right) OWT.

Comparing the maximum loads that are transferred at the interface level from the tower bottom to the foundation at different load conditions it is apparent that for both turbines the design driver is DLC 6.2 exhibiting the highest resulting loads. As expected the 10 MW turbine induces higher loads in absolute values than the 8MW turbine. For example, in DLC 6.2 where the turbines experience a 50-year wind gust in idling condition, the maximum results loads Mres (10 MW) with 221MNm exceeds the Mres (8MW) with 143MNm by a factor of 1.55.

Comparing the fatigue loads to be transferred by the foundations of each wind turbine, the fore-aft direction forces and moments are as expected significantly higher for the 10 MW turbines due to the larger rotor size (Figure 2). For jacket design tasks, the level of torsional moments applied at interface level is often driving the design as jacket structures are less stiff than monopiles in the torsional direction. Both turbines show a higher fore-aft bending fatigue than torsional fatigue, in particular the ratio between torsional and fore-aft fatigue loads (M_x/M_z) is approx. 390 % for both

turbine models. Thus it is expected that the foundation design for both turbines foundations will be driven to the same extent by the required stiffness in the torsional direction.

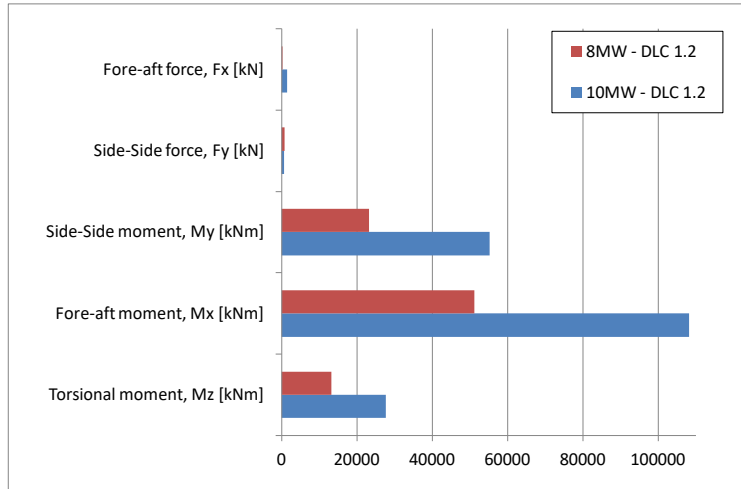


Figure 2 - Comparison of simulated equivalent fatigue loads according to DLC1.2 but different environmental conditions.

The obtained jacket geometries have been analysed leading to the following observations:

The tubular elements (Circular Hollow Sections CHS) geometries, cumulated for all the considered 6 windfarm scenarios, are reported in terms of external diameter OD and wall thickness WT (Figure 3) showing a certain degree of repetitiveness for defined ranges of products.

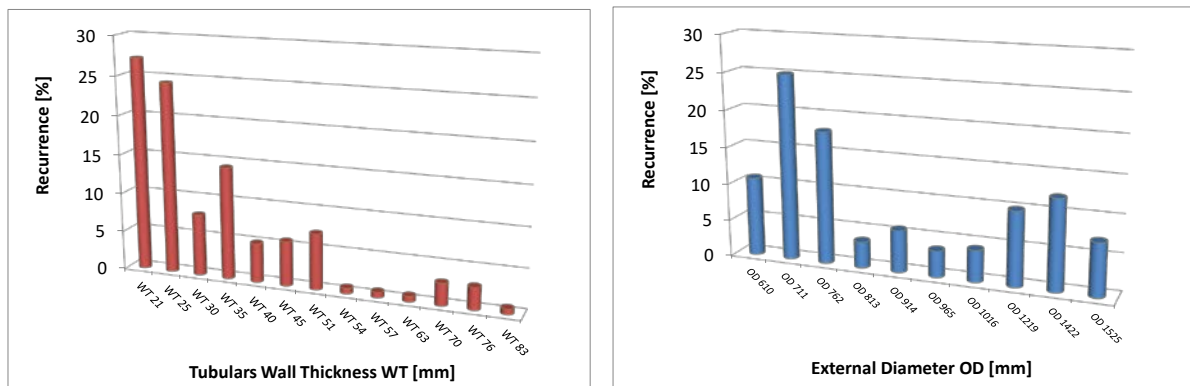


Figure 3 - Recurrence of pipe geometries cumulated for the 6 windfarm scenarios.

The joints typology with the higher degree of recurrence are the X-joints among which there are some geometries (i.e. chord 711x35mm; brace 711x21mm) that repeats in almost all the analysed windfarm scenarios. It is not so for DK-joints and DY-joints that show poor or no repetitiveness throughout the different windfarm scenarios.

WP2 - MODULAR JACKET LOAD ANALYSIS

Time domain simulations for 8MW and 10MW turbines in 6 different water depths have been performed with estimation of the internal loads at the joint-connections.

Two different softwares have been applied for the scope:

1. ROSA and LACFlex software by Ramboll relevant to the 8MW wind turbine.
2. hGAST hydro-servo-aero-elastic software NTUA an in-house developed relevant to the 10MW wind turbine.

A specific load case table is set up for each evaluated location. The jacket design is usually driven by wind fatigue loads of the turbine under operation and during idling. Therefore, the design load cases (DLC) 1.2, 6.1 and 6.2 according to IEC61400-3 have been considered.

The result of each performed simulation consists of time series of sectional forces for all jacked members. The reported sectional forces are characteristic loads, which means that no partial safety factors on loads or material are applied. Probabilities of occurrence for each load case have been extracted from environmental load analysis of Task 1.1.

Stress histograms representative of the different jackets scenarios have been obtained. Estimations of fatigue damage accumulation at selected critical locations of the examined Jackets were conducted. The jacket geometry defined in Task 1.3 and the time history of stress resultants produced in Task 2.2 were used in order to calculate the fatigue damage of selected components.

WP3 - DESIGN OF THE FOUNDATION OF THE MODULAR JACKET

A Finite element model of traditional piled foundation and soil behaviour has been developed and extensively validated against physical model testing and relevant literature demonstrating its effectiveness in describing the overall soil-foundation system response under cyclic loading conditions. Soil constitutive model has been carefully evaluated and among the alternatives the C yield surface was found to best describe the ultimate bearing mechanism and the soil-foundation stiffness in the small-medium strain regime.

The validated model was implemented to analyse the response of the entire soil-foundation-Jacket-OWT System under the combined action of environmental loads. The coupled FEA were found to compare satisfactory well to simplified design procedures. Comparison is better under NC, while for extreme environmental loading, the simplified approach tends to overestimate deformations.

An alternative foundation solution has been considered, that of a suction caisson. Ease of installation is the main advantage of this foundation type. The bearing mechanism of suction caissons was found to be controlled by the properties at the soil-caisson interface. Under perfectly "sealed" conditions (i.e., when suction may be granted), a "reverse end bearing" mechanism is mobilized accompanied by significantly higher resistance values. If the "sealing" is inefficient (i.e., in case of improper installation or when the soil permeability is very high to sustain suction), resistance values reduce as failure occurs only in the form of sliding along the caisson sidewall. For typical soil profiles and caisson dimensions, this decrease may be as high as 40% of the nominal value (assuming full suction). The jacket performance is only marginally affected by the assumed suction conditions. At Normal Sea State, the jacket response under 'suction' or 'no-suction' assumption is completely identical, while even for extreme environmental loads, the differences in the response are not that important. The beneficial effect of suction was found to be marginal also for seismic loading combinations.

An intriguing comparison of 10^{MW} OWT in the seismic Mediterranean Sea location, supported by 4-legged jacket either on piles or suction caisson has been performed. OWTs (being extremely flexible) are generally insensitive to ground shaking when subjected to pure earthquake loading. Alarming conditions for the operability of the turbine may arise when seismic shaking is combined with a non-zero wind force acting at the top of the tower. This wind-induced asymmetry, coupled with the kinematically-generated stressing on the foundation, tends to trigger increasingly high rates of accumulated rotation throughout the duration of the strong seismic shaking.

Design charts for sand and clay sites are provided that: (i) facilitate quick dimensioning of foundation elements (i.e. Diameter and Embedment Length L) in order to achieve specific levels of safety (for a range of soil sites and sea depths) and (ii) correlate amplitude at Jacket supports to maximum foundation deformations (displacement and rotations) for a range of plausible foundation dimensions. The scenarios involved windfarms in the North Sea or the Mediterranean Sea, considering turbines of 8MW and 10MW. For the cohesionless North Sea sites, design charts for piled were provided foundation, while for the North mediterranean sites (where the seabed consists mainly of clayey soils), design charts for suction caissons were delivered.

WP4 - MANUFACTURING OF STANDARD COMPONENTS FOR TESTING

The reference tubular joint geometry has been selected after analysis of the different jackets designed for the 6 windfarm scenarios. In particular it was agreed to focus on the X-brace connection, being the most recurrent joints in the considered windfarm scenarios (WP1).

Both base materials and consumables have been procured with the nominal grade of S355J2 as state-of-the-art material widely used in offshore constructions. Three roll bending performed to produce pipes of the suitable dimensions in accordance with the provided specimens drawings.

The following processes with incremental level of automation have been studied and written Welding Procedure Specifications have been developed on:

- Semi-automatic Arc welding (MAG): state-of-the-art manufacturing process
- Fully Automated Arc Welding (Automatic MAG welding): near future completely automate a welding process in which both the welding head and the steelwork are handled automatically but the welder can tune the parameters during welding (on-fly).

- Robotized Welding (both TIG+MAG and Laser+MAG): a step forward process in which, both the welding head and the steelwork are handled automatically; furthermore the system is programmed and the operator cannot change the process parameters.
- Hammer peening post welding treatment has been applied on 2 X-joints after a study of microstructure and joint to optimize the performance (shape of tool, speed, etc).

A total of 37 joints have been fabricated and characterized according to EN ISO 15614-1. Moreover a 100% radiographic inspections (RT) and penetrant testing (PT) have been performed on the joints showing absence of unacceptable defects according to UNI EN ISO 5817 Quality Level C.

Actual welding parameters recorded during trials have been implemented in the selected Cost model, i.e. AWS-WHB-B5.7 [3] which details are also reported in Task 7.3.

WP5 – EXPERIMENTAL INVESTIGATION ON SELECTED SCALED COMPONENTS

SMALL SCALE TESTING

Geometrical inspections of received X-joints have been performed comparing the semi-automatic welded joints (SA) than for the fully-automatic ones (FA). At saddle location the weld bead angle with respect to the chord is generally higher for the SA weld than for the FA weld. At the crown location crack initiation is in the weld metal in the convex area, this failure behaviour and geometrical raiser is common to both SA and FA welding processes.

Residual stress measurements have been performed with different techniques. Values obtained with X-ray diffraction and Hole drilling on the semi-automatic joints (SA) are consistent varying between + 200 MPa and - 400 MPa (actual base material yield strength is almost 500 MPa). Values obtained for the fully-automatic joints (FA) shows a tendency to higher residual stresses close to the welded joint (HAZ), particularly when compressive residual stresses are considered.

HFMI can increase the fatigue performance of the off-shore jackets. Experiments carried out with small specimens, containing the most aggressive stress raiser of the joint, revealed a fatigue life increase of at least 30%. The average of fatigue life increase was multiplying the original fatigue life by a factor of 3.05 (more than 300% of fatigue performance improvement).

LARGE SCALE TESTING

A total number of 24 X-joints have been tested in full scale. The testing program has been updated (Table 2) to focus on cyclic loading that is the design driving conditions for offshore wind jackets. The testing program has been rearranged to obtain the more as possible number of fatigue data: the monotonic tests (task 5.2) have been substituted with extra fatigue tests (Task 5.3).

Two different testing methods are considered:

- Resonance testing: this testing method is based on the resonant bending principle, where the excitation is caused by an eccentric mass, allowing for the out-of-plane bending and in-plane bending mode by the eccentric mass, in the course of the same test, at a frequency between 20 and 40 Hz.
- Traditional hydraulic testing (both in-plane bending-IPB and out-of-plane bending-OPB): this is a tradition way to test components under cyclic fatigue behaviour. It implies a frequency much lower than the resonance one (e.g. less than 10Hz). The tests are sheared between in-plane and out-of-plane bending tests.

Table 2 - Actual full-scale testing program (Task 5.2 and 5.3)

Fabrication process	In-Plane Bending fatigue	Out-of-Plane Bending fatigue		Resonant fatigue
	Constant amplitude fatigue	Constant amplitude fatigue	Variable amplitude fatigue	Constant amplitude fatigue
Semi automatic (SA)	4	4	2	2
Fully automatic (FA)	4	4	-	2
Post weld treated HFMI	2	-	-	-

Experimental data are compared with standard fatigue design curves (S-N curves) for offshore tubular joints proposed by ISO 19902 and RINA rules, DNV-RP-C203 and API-RP-2A (Figure 4).

The experimental data are generally in good agreement with the design provisions: the experimental data lies on the safe side of the S-N diagrams of standard weld profile. The data have been analysed according to ASTM E739 by considering separately SA and FA joints. FA experimental data show a minor scattered among each other, i.e. the Standard Deviations (SD) obtained are 0.3538 and 0.3768 for FA and SA data respectively. The calculation of standard deviation is affected by the reduced number of available data. The design curves are calculated by applying both experimental standard deviation and reference standard deviation for tubular joints (i.e BS7608 value of SD=0.2484).

HFMI treated SA joints, according with small scale experimental results, show a significant increase of fatigue resistance (i.e. up to 3 times longer fatigue life for the investigated number of cycles).

Variable amplitude SA test data, evaluated according with linear damage accumulation Miner's rule, are consistent with constant amplitude data showing the consistency of linear damage accumulation rules for the number of cycles considered (i.e. between 1E5 and 3E6 cycles).

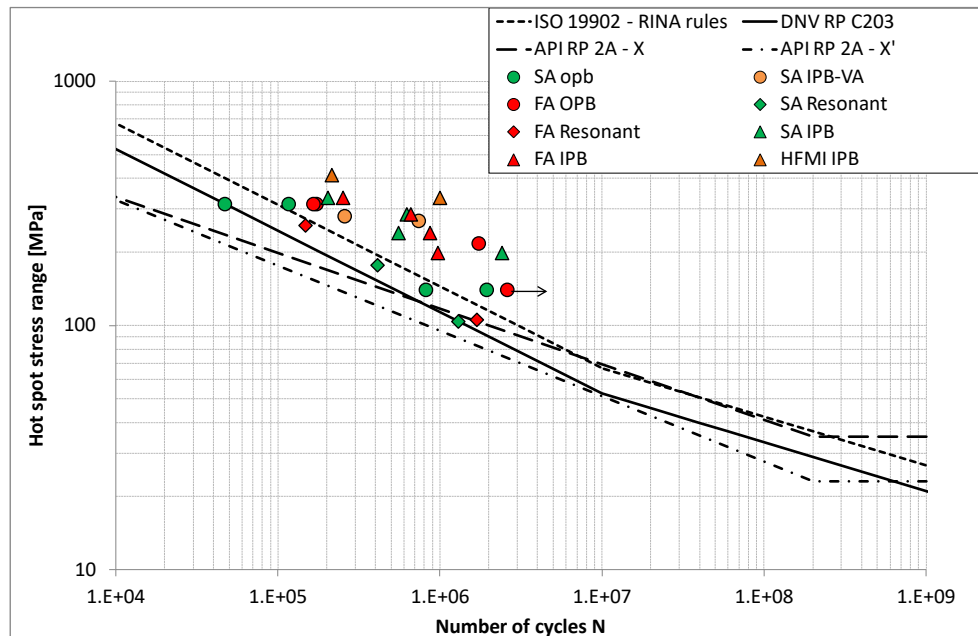


Figure 4 – Experimental data compared with offshore joints fatigue design curves.

SA and FA have been fitted assuming a linear curve with inverse slope equal to 3 (according with DNV-RP-C203 T-curve) in the log-log space Figure 5. By imposing SD from BS 7608 SA data are in good agreement with design provisions while a small improvement in fatigue resistance of FA joints is evaluated. The relevant design S-N curves are obtained by subtracting two standard deviations from the 50% probability curve.

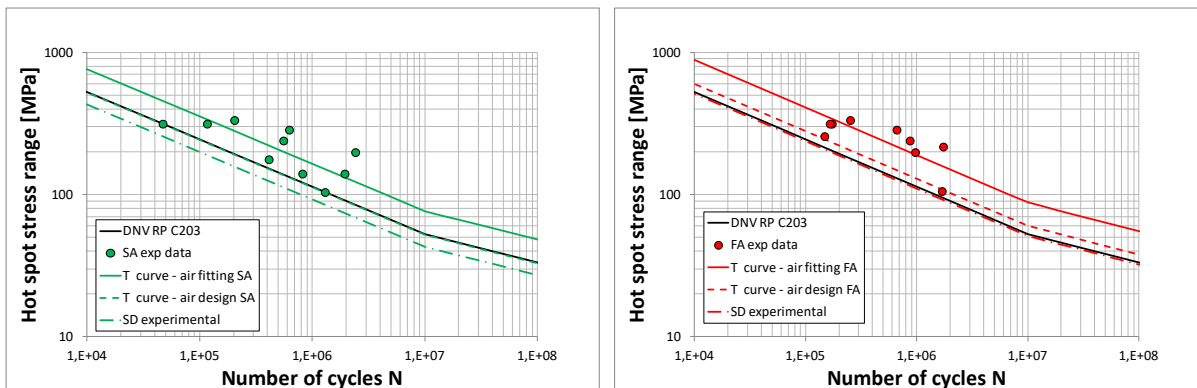


Figure 5 – Experimental data fitting of semi automatic (SA) and fully automatic (FA) welded joints.

The so obtained S-N curves have been then used to recalculate fatigue life of the reference joints according to the calculation procedure implemented in Task 2.3 leading to a potential increment around 40% in fatigue life at low number of cycles (i.e. between 1E5 and 3E6 cycles).

WP6 - FINITE ELEMENT SIMULATIONS ON THE STANDARD COMPONENTS

Three finite element models have been developed with the aim of set up the different full scale tests under consideration (WP5). The models have been fine tuned upon experimental data and strain gauge measurements during testing (task 5.2-5.3). In particular deep modelling of the weld shape has been implemented showing the beneficial effect of this modelling technique.

The tuned finite element models have been used to for parametric analysis (task 6.3) by which tuned SCFs for the prefabricated joints geometries for the different windfarm scenarios have been obtained. The final fatigue damage was then re-evaluated also considering experimental S-N curve of the fully automated (FA) production. Although by considering actual standard deviation affected by reduced number of data available there is no improvement of fatigue life, if we assume the standard BS 7608 value for the standard deviation it is possible to obtaining a sensible reduction of the fatigue damage factor (over 40%) (Figure 6):

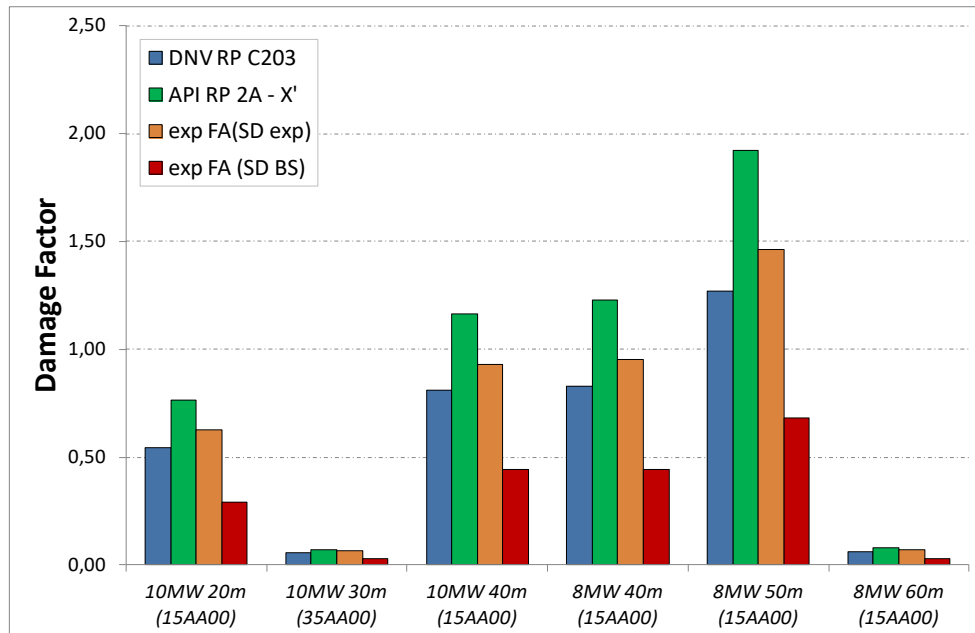


Figure 6 – Damage Factor calculated for the selected critical locations and impact of automated productions benefits (experimental FA values).

A study on the effect of assembly misalignment has been done, the SCF can be significantly affected by assembly imperfections of 10% of diameter, with an SCF variation of 15-16% in magnitude.

WP7 – IMPACT OF MODULARITY AND QUALITY/COST ANALYSIS

With the aim of evaluate on the jacket execution method of the Modular Jacket concept, possible alternatives jacket execution methods are draft, starting from state-of-the-art jacket execution and taking into consideration the availability of pre-fabricated subassemblies. The outcome is the partitioning of fabrication into different stages with different potential impact of prefabrication approach. In particular The following fabrication phases with potentially sensitive to prefabrication are identified:

- Circular hollow sections (CHS) manufacturing, actually done by three roll bending and manual welding;
- Subsets assembly stage for fabrication of X-brace joints and connection of CHS with different dimensions.

The impact of prefabrication is firstly assessed for specific components (Task 7.2), i.e. tubular butt joint and tubular X-joints, via the detailed simulation of welding process on the basis of parameters recorded during trials (Task 4.4). Welding times and costs have been evaluated according to AWS cost model. In particular:

- tubular X-joint a reduction of 24% in total costs and 30% in welding time is estimated applying a fully automated MAG process;
- tubular butt joint for which different process improvements are considered the average savings are reported in the following table:

PROCESS	FA-MAG V edge prepar	FA-MAG U edge prepar	LBW+MAG VV edge prepar
---------	-------------------------	-------------------------	---------------------------

Cost reduction	-18%	-57%	-35%
Time reduction	-25%	-62%	-41%

The average process parameters have been applied to the relevant jacket fabrication phases and a picture of total jacket assembly costs has been obtained for the different scenarios analysed. In particular the following conclusions have been drawn:

- Large part of the jacket costs comes from the circular hollow section manufacturing. The use of LSAW welding reduces the CHS manufacturing cost by 36-46% and manufacturing times by 39-51%. Welding consumables have a higher cost but are compensated by the higher deposition rate of fully automatic welding.
- The use of fully automatic MAG welding for prefabrication of X-joints and legs is implemented at the Subsets phase. Considering a welding rate 3 times higher than traditional semi-automatic MAG process and 3k€ of programming costs per joint geometry the total Subsets fabrication is evaluated to save 56-61% in costs and 57-62% in times.
- In a mass production (i.e. minimum 10 jackets of the same geometry) overall savings for the complete jacket (excluding transitional piece, piles and secondary structures) is evaluated between 20% and 26% in costs and between 34% and 44% in times, depending on jacket geometry.

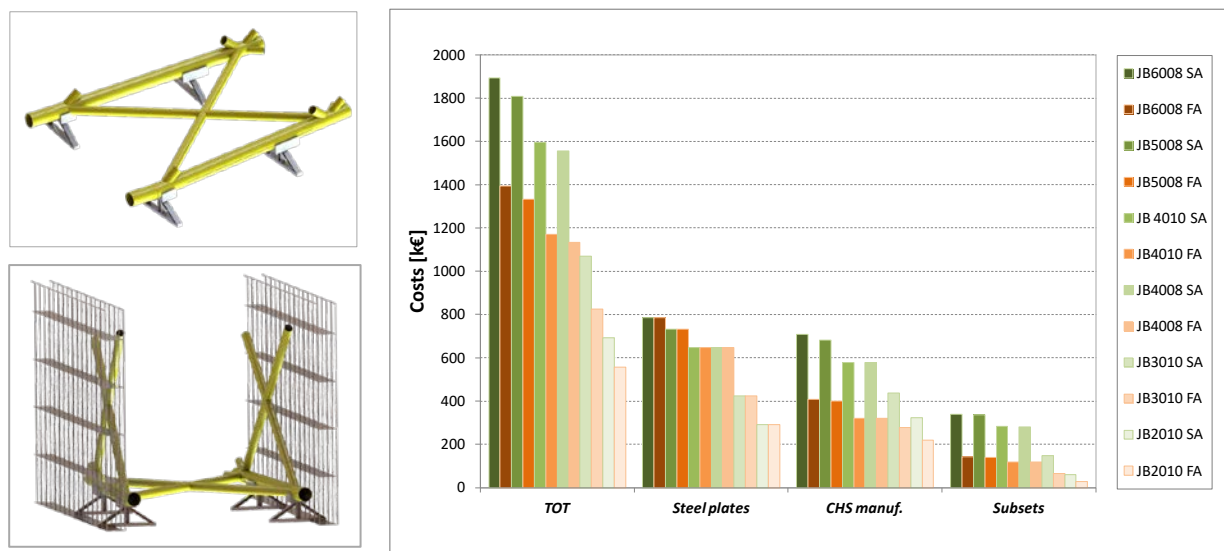


Figure 7 - Summary of costs for the different execution phases.

WP8 – DEVELOPMENT OF JABACO MANUAL AND DISSEMINATION OF RESULTS

The Jabaco tool has been realized as a free web access database (www.jabaco.it) containing main data developed during the project and potentially useful to the steel industry to develop prefabricated components for offshore wind jackets. In particular it comprises:

- Configuration of the jacket for the 6 different case studied
- Environmental load from the different locations
- In-service stress histories relevant to each of the 6 case studied
- Drawings of standard components developed
- Fine tuning of stress concentration factors
- Allowable fatigue life of standard components
- Modularity concept and fabrication costs for the different case studied

Two (2) seminars were held in different European countries, Genoa (Italy) and Edinburgh (UK). Both locations are significant with respect to offshore and marine engineering. The seminar's program included formal presentations by each Partner followed by a discussion period. At the Edinburgh seminar experienced scientists in offshore engineering were invited to give Lectures. Multiple social media channels were used where appropriate for advertising.

SCIENTIFIC AND TECHNICAL DESCRIPTION OF THE RESULTS

PROJECT OBJECTIVES

The aim of Jabaco project is to investigate the benefits of the modular jacket concept. With this aim a wide range of offshore windfarm scenarios have been considered: water depths 20-60m and turbine size 8-10MW, installed in North Sea and Mediterranean Sea.

The Modular Jacket solution is composed by qualified prefabricated components leading to cost-reduction during mass-production. With this aim incremental automated fabrication processes are considered and deeply analysed by means of fabrication trials and experimental testing.

The final outcome is the evaluation of costs and benefits of the Modular Jacket solution.

WP1 - DETERMINATION OF LOADING CONDITIONS AND PRELIMINARY ANALYSIS

OBJECTIVES AND MAIN OUTCOMES

This WP aims at establishing the design basis for the Modular Jacket solution. In particular 6 different windfarm scenarios are considered:

Table 3 - Overview of boundary conditions for the 6 considered jackets.

Wind Turbine	Water depth/Location				
	20 m	30 m	40 m	50 m	60 m Mediterranean (seismic)
	North Sea	North Sea	North Sea	North Sea	L1
8 MW		L4	L2	L3a	√
10 MW	√		√	√	√

For all combinations of considered offshore locations and turbine sizes, feasible jacket designs could be set up.

In the following a detailed description of the activities for each task of WP1 is reported.

TASK 1.1 MET-OCEAN DATA AND SOIL CONDITIONS

In this task the estimation of the design environmental conditions (wind and wave climate, extreme sea levels and univariate and bivariate design values for significant wave height H_{m_0} , wind speed U_w , and wave spectral peak period T_p) at 4 locations in the Mediterranean and the North Seas has been performed. The locations for implementation of the project activities have been selected taking into account the following criteria: i) The bottom depth should be suitable for installation of wind turbines; ii) The wind resource in the area should be exploitable; and iii) The considered time series lengths of the met-ocean parameters should be long enough in order for the extreme value analysis to be implemented. The locations selected are shown in Figure 8.

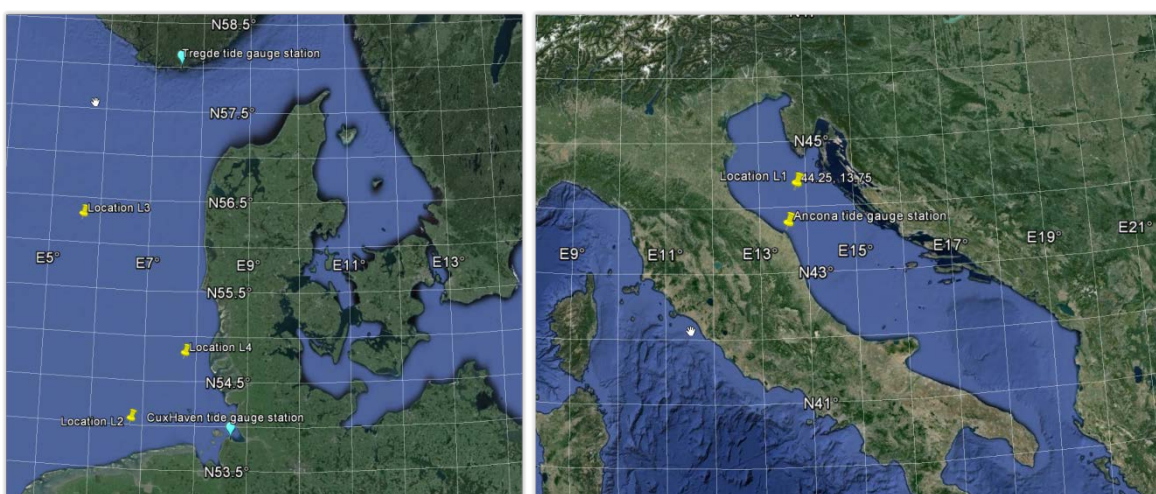


Figure 8 - Windfarm locations under investigation.

MET-OCEAN DATA SOURCE

The met-ocean data source refers to numerical model simulation results obtained by the Era-20C data set, published by the European Centre For Medium-Range Weather Forecasts (ECMWF) [1]. The original simulations extend to the period 1900-2010 with recording interval 3h. To avoid non-stationarity and inhomogeneity issues in the statistical and extreme value analysis, we considered the last 31 years of the available time series (1980-2010). Let it be noted that, since all the results presented here are obtained from numerical simulation models, they are subject to errors and uncertainties compared to the actual wind and wave conditions in the examined area. The analysed time series correspond to H_{m_0} , T_p and U_w , and the wind and wave direction θ_H and θ_U , respectively.

Regarding sea-level data, it was not feasible to have access to high-frequency data obtained by high spatial resolution model simulations. Therefore, available sea-level measurements from the closest coastal stations have been utilized. Let it be noted here that sometimes the distance between the examined location and the sea level measurement station may be large and sea level data may not be representative of the examined sites. Moreover, since sea-level data are obtained through tide gauges, the provided measurements include the effects of all relevant local phenomena, i.e., tides, storm surges, extreme wave events, potential climate changes, etc. It is also anticipated that the provided values should, in general, overestimate the corresponding sea-level values offshore, since tidal effects are more pronounced close to the shore.

The sea level data set available for location L1 are obtained from the Ancona station (43.65° N, 13.55° E, <http://www.mareografico.it>), at a distance of ~67km from the examined location and time series length 5 years (2010-2015). For locations L2 and L4 the closest available sea level station is CuxHaven (53.87° N, 8.69° E) at a distance of ~125km and ~110km respectively. Furthermore, there is a defined datum (zero reference), which is associated to fixed bench marks in shore. For location L3 the closest station with sea level data freely available is Tregde, (58.00° N, 7.55° E) at a distance of ~215km. The distance between the tide-gauge and the examined location in this case is very large, and thus the involved relevant uncertainties are increased. For CuxHaven and Tregde the sea level data are available from <http://uhslc.soest.hawaii.edu> and the time series length is 31 years (1980-2010).

STATISTICAL ANALYSIS OF MET-OCEAN AND SEA-LEVEL DATA

In Table 4 the main statistical characteristics of met-ocean parameters for the examined locations are summarised (sample size N , mean value m , standard deviation s , coefficient of variation CV , maximum max , minimum min , skewness Sk and kurtosis Ku). The values refer to the total available samples for the period 1980-2010. For location L1, the consideration of high values of spectral peak period (above 20s, corresponding to very low sea-states with $H_{m_0} \sim 0.007m$), justifies the high values of skewness and kurtosis for T_p and the high variability of H_{m_0} . These values have not been taken into consideration in the univariate extreme value analysis.

Table 4 - Statistical analysis of wind, wave and sea level time series at locations L1-L4

	Location	N	m	min	max	s	CV	Sk	Ku
H_{m_0} (m)	L1	90584	0.227	0.007	3.188	0.251	110.808	2.770	11.646
	L2	90584	1.347	0.046	8.316	0.914	67.898	1.522	3.138
	L3	90584	1.754	0.078	10.076	1.146	65.318	1.454	2.842
	L4	90584	1.399	0.0446	10.475	0.978	69.962	1.685	4.354
T_p (s)	L1	90584	3.681	2.430	23.939	1.685	45.768	8.432	96.869
	L2	90584	6.267	2.430	17.572	1.698	27.101	1.063	2.527
	L3	90584	6.946	2.430	17.360	1.737	25.013	0.760	1.083
	L4	90584	6.376	2.430	17.508	1.751	27.463	0.955	2.076
U_w (m/s)	L1	90584	3.249	2.000	15.085	1.673	51.502	1.851	3.917
	L2	90584	7.200	2.000	20.929	3.221	44.741	0.431	-0.308
	L3	90584	8.303	2.000	23.162	3.503	42.188	0.423	-0.315
	L4	90584	7.274	2.000	23.363	3.217	44.220	0.410	-0.273
Hydrometric sea level (m)	Ancona	51530	0.0353	-0.56	0.96	0.176	499.140	0.175	0.336
Sea level (m)	CuxHaven	271752	5.135	1.110	9.520	1.123	21.88	-0.101	-1.066
Sea level (m)	Tregde	256730	0.990	0.381	2.100	0.171	17.27	0.438	0.692

The same statistical parameters are also provided for sea-level (with 1-hour recording intervals). For CuxHaven station the results refer to a fixed point in land. For Tregde station the parameters refer to the absolute sea-level (obtained with reference to a fixed point in land). In the relevant Deliverable 1.1, a detailed discussion on the wind and wave roses and the 2D histograms of met-

ocean parameters is also presented.

EXTREME VALUE ANALYSIS (UNIVARIATE CASE)

For the estimation of the design values of H_{m_0} , U_w and T_p , the annual maxima method (AMM) will be applied. The underlying distribution is the Generalized Extreme Value (GEV) distribution and the estimation of its parameters is made by implementing the Maximum Likelihood Method; see Coles (2001), Soukissian, Kalantzi (2006), Soukissian, Tsalis (2015). In Table 5 the design values of H_{m_0} , U_w and T_p , for various return periods (in years) for locations L1-L4 are shown. The detailed univariate extreme value analysis is presented in the relevant Deliverable 1.1, where the analytic fit results and the 95% confidence intervals for design values are also provided. In the same deliverable the bivariate extreme value analysis and corresponding results are also included.

Table 5 - Design values for significant wave height (m), wind speed (m/s) and spectral peak period (sec) for various return periods (in years) for locations L1-L4

Return period (years)		10	20	30	40	50	60	70	80	90	100
H_{m_0}	L1	2.59	2.80	2.91	2.99	3.05	3.10	3.14	3.17	3.20	3.23
	L2	7.21	7.58	7.78	7.92	8.02	8.11	8.17	8.23	8.29	8.33
	L3	9.42	9.77	9.93	10.03	10.11	10.16	10.20	10.24	10.27	10.30
	L4	8.81	9.45	9.80	10.04	10.22	10.37	10.49	10.60	10.69	10.77
U_w	L1	13.54	14.04	14.31	14.50	14.64	14.74	14.84	14.91	14.98	15.04
	L2	19.76	20.34	20.66	20.89	21.07	21.21	21.33	21.43	21.52	21.60
	L3	22.38	22.78	22.96	23.07	23.15	23.21	23.26	23.30	23.33	23.36
	L4	21.03	21.79	22.21	22.49	22.70	22.87	23.01	23.12	23.23	23.32
T_p	L1	9.12	9.82	10.24	10.53	10.76	10.956	11.12	11.26	11.38	11.50
	L2	15.75	16.26	16.52	16.69	16.81	16.912	16.99	17.06	17.11	17.16
	L3	16.22	16.87	17.23	17.48	17.67	17.828	17.96	18.07	18.17	18.25
	L4	16.39	16.86	17.09	17.24	17.35	17.43	17.50	17.56	17.60	17.65

SOIL DATA

For the preliminary jacket design the soil has been represented by an average sand profile, as displayed in Figure 9. The preliminary jacket design has been conducted considering the most common foundation typology, i.e. piles driven into the sea bed prior to installation of the jackets; the annulus between jacket leg and pile grouted after lowering of the jacket. An investigation to evaluate the impact of different foundations typologies is in progress in WP3.

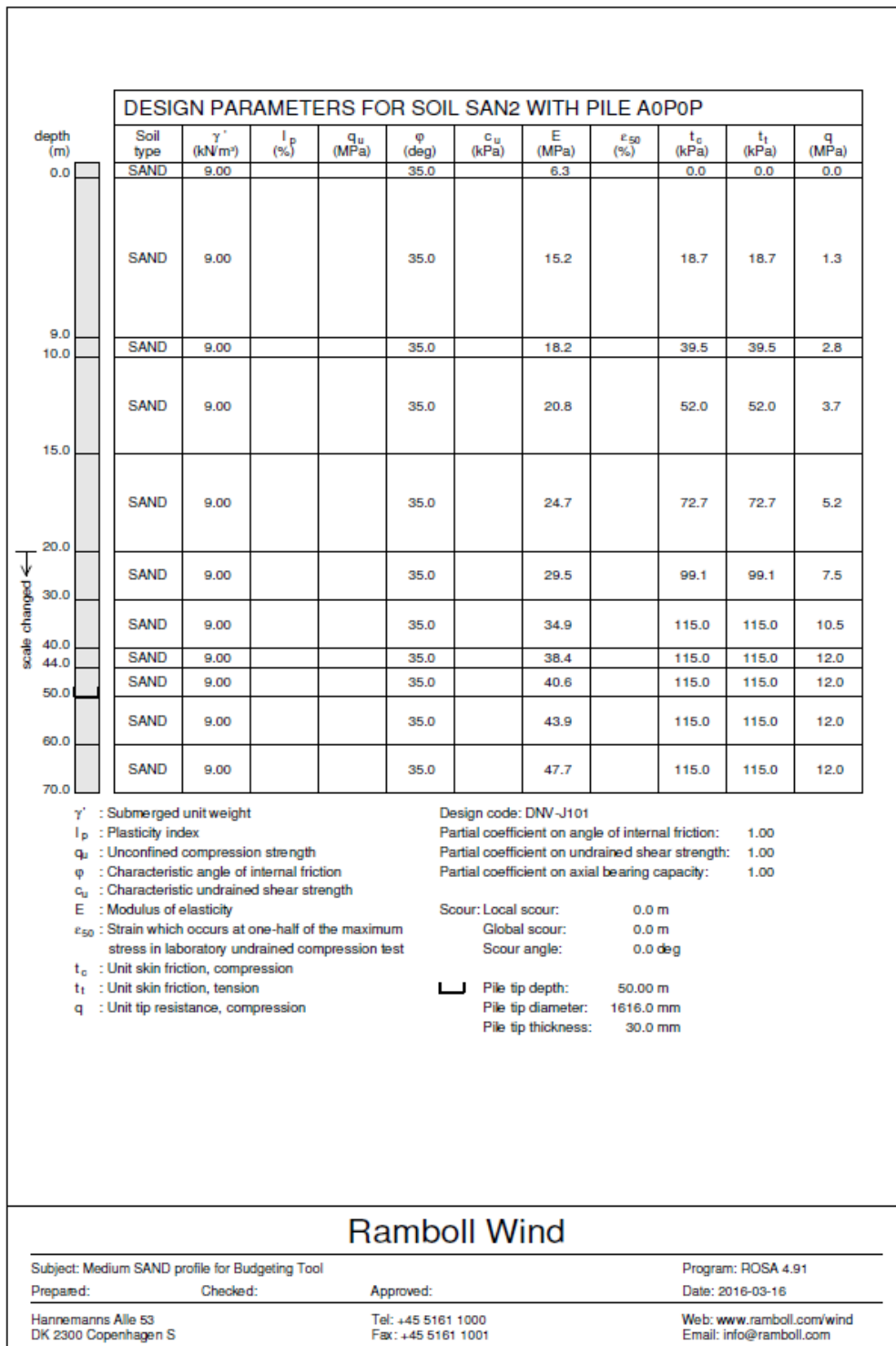


Figure 9 - Reference soil for jackets design: average sand profile.

TASK 1.2 SET-UP OF 8MW AND 10MW TURBINE MODEL

This section contains a description of the generic wind turbine model and its controller.

Figure 10 shows a sketch of the wind turbine with the coordinate system of the reaction forces in the tower bottom which constitutes the interface level.

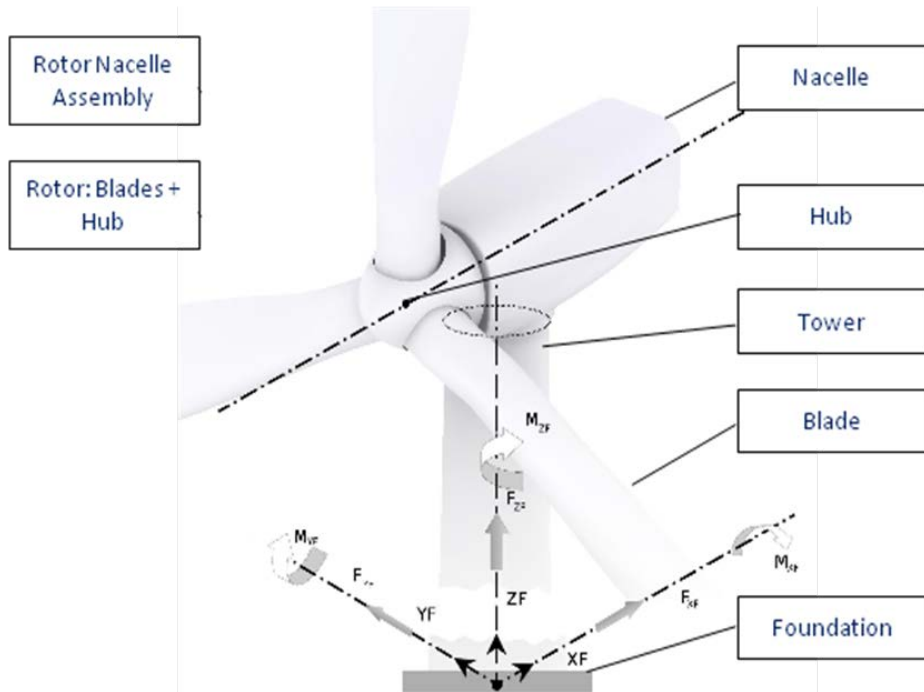


Figure 10 - General wind turbine layout and reaction forces at the tower bottom.

All state-of-the-art wind turbines follow the same principles of wind energy conversion where electricity is produced in the generator and the resulting wind thrust is transferred eventually into the foundation. Optimal design of these machines is concerned with the balance between desired maximum power output and sufficient strength to endure the lifetime loading. As a result, state-of-the-art wind turbine share some fundamental characteristics which is a three-blade, variable speed, horizontal axis, pitch controlled, wind turbine with sophisticated aerodynamic blades that transform the kinetic energy of the wind into rotational speed of the rotor and thrust. The conversion performance is dependent on the wind speed, controlled by the speed and pitch control of the turbine and expressed by the two most important dimensionless quantities, the coefficient of power (C_p) and the thrust coefficient (C_t).

Generic 8 MW and 10 MW wind turbines for IEC design load simulations of wind turbines is established using the state-of-the-art aero-elastic codes FLEX 5 and hGAST respectively. It is common to model the structural dynamics using relatively few but carefully selected degrees of freedom, using shape functions for the deflections of the tower and the blades while using stiff bodies connected by flexible hinges to model the nacelle, rotor shaft and hub. The aerodynamic loads on the blades are calculated using the Blade-Element-Momentum method including dynamic stall and wake models. The control system that takes care of the different operational regimes of the wind turbine is modelled in a separate Matlab/Simulink environment and supplied to the simulation in the format of a Bladed Style DLL, which is common in the wind industry.

The parameters for the aero-elastic model comprise geometries, mechanical properties, operational set-points and most importantly air-foil profile data. Realistic values are obtained by applying scale up laws known from literature, generic models available to the public like the NREL5MW and the DTU10MW and publicly available data e.g. on blade masses that can be represented as cubical function of the rated power.

After initial setup the controller is tuned to achieve stability in the operational region of the wind turbine. Final validation is achieved by extensive simulations of realistic operational conditions as defined in the IEC standards. Special attention is given to the power curve and the loads on the main components like tower, blades and drive train.

The present generic 8 MW and 10 MW wind turbine models are set-up to generate realistic interface loads both ultimate and fatigue, as required for the support structure design. The ultimate and fatigue loads presented are computed with time domain simulations according to IEC load cases

and presented at the interface level (tower bottom). In terms of dimensions, the 10 MW wind turbine is naturally larger than the 8 MW wind turbine. This results in 14m larger rotor diameter and 12 m higher hub heights to assure the required blade tip clearance to the outer platform which leads to both increased thrust forces and longer lever arm, resulting in larger bending moments that need to be transferred into the ground by the foundation.

Comparing the maximum loads that are transferred at the interface level from the tower bottom to the foundation at different load conditions it is apparent that for both turbines the design driver is DLC 6.2 exhibiting the highest resulting loads. As expected the 10 MW turbine induces higher loads in absolute values than the 8MW turbine. For example, in DLC6.2 where the turbines experience a 50 year wind gust in idling condition, the maximum results loads Mres(10 MW) with 221MNm exceeds the Mres(8MW) with 143MNm by a factor of 1.55.

Comparing the fatigue loads to be transferred by the foundations of each wind turbine, the fore-aft direction forces and moments are as expected significantly higher for the 10 MW turbines due to the larger rotor size and the higher turbulence intensity used during simulation.

8 MW WIND TURBINE

To demonstrate the static operational behaviour of the wind turbine, the figures below show mean values of the time behaviour of rotor speed , pitch angle and power output over the wind speed at hub height. It shows how the different normal operational conditions of the wind turbine are handled by the controller. In partial load between 5 and 12 m/s the rotational speed increases with increased wind speed, the power follows a cubical function for optimal harvesting of the wind kinetic energy. Beyond the rated rotor speed that is reached between 10 m/s and 12 m/s wind speed, the pitch is activated to keep the rotor speed at the maximal allowed speed, thus limiting the electrical power output. Beyond 25m/s the wind turbine is shut down.

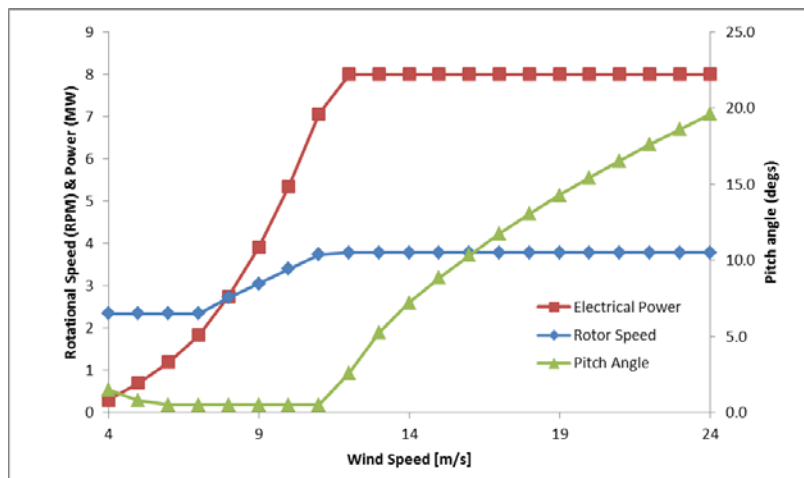


Figure 11 - Steady state operational curves showing mean (10min) electrical power, rotor speed and pitch angle over mean (10min) wind speed.

The dynamic performance of the wind turbine controller is typically demonstrated by applying virtual step response functions which constitute the most severe change in operational conditions. The controller has to prove stable operation by allowing the wind turbine to settle back at static values after such severe perturbation. The figures below show the time series of a performed step-wind load case, the time response of the power output and the resulting loads.

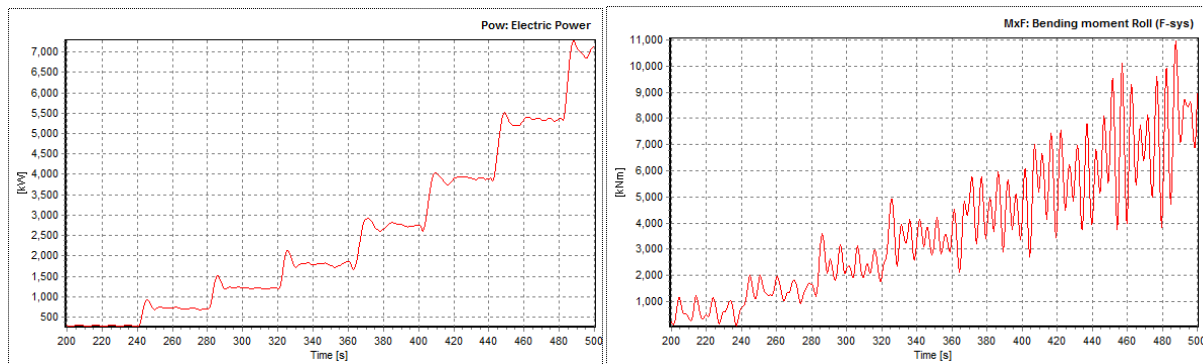


Figure 12 - 8MW turbine model: time series of the electrical power of the wind turbine (left) and the side-to-side bending moment (right).

The generic loads calculated for the described wind turbine model refer to the coordinate system displayed in Figure 10.

Table 6 - Wind turbine geometry, structural and operational parameters based on exemplary hub height of 107m LAT.

	Data	Unit
General		
Model name	Ramboll-Generic-8MW	
Rotor diameter	164.0	m
Number of blades	3	-
Nominal power	8,000	kW
Power rating	379	W/m ²
Nominal rotor speed	10.5	rpm
Minimum rotor speed	6.5	rpm
Hub height	107.0	m
Support structure		
Tower length	87.0	m
Interface height	17.0	m
Tower mass	392,000	kg
Lower frequency bound	0.20	Hz
Upper frequency bound	0.29	Hz
Rotor Nacelle Data		
Nacelle mass (excl. rotor)	295,000	kg
Rotor mass	210,000	kg
RNA mass of inertia (x)*	74.74	10 ⁶ kgm ²
RNA mass of inertia (y)*	58.07	10 ⁶ kgm ²
RNA mass of inertia (z)*	43.98	10 ⁶ kgm ²
RNA CoG (x)*	0.00	m
RNA CoG (y)*	-1.32	m
RNA CoG (z)*	3.18	m
IEC design conditions		
Structural design life time	25.0	years
Mean wind speed	11.0	m/s
Weibull shape factor	2.0	-
Wind shear exponent	0.14	-
Extreme 50-year wind (10 min)	50.0	m/s
Turbulence IEC Iref (Class B)	0.14	-

10 MW WIND TURBINE

The DTU 10MW RWT (Bak, 2013) is used to generate realistic loads both ultimate and fatigue, as required for the support structure design. This section contains a description of the wind turbine model and its controller. Table 7 gives an overview of the parameters related to geometry, structure, operation and environment in accordance with known parameters of commercial turbines of comparable classes. The tower relevant for offshore jacket applications is presented.

Figure 14 below shows mean values of the rotor speed, pitch angle and power output over the operational wind speed range between 4 and 25 m/s.

In Figure 13 and Figure 15 the increased electrical power production and the reduced tower base side-to-side bending moments are presented that justify the selection of the controller setup. The simulations have been performed using hGAST hydro-servo-aero-elastic simulation platform (Manolas, 2015).

Table 7 - General Characteristics of DTU 10MW RWT

	Data	Unit
Model name	DTU 10MW RWT	
Wind Regime IEC	Class 1A	
Rotor Orientation	Clockwise rotation - Upwind	
Control	Variable Speed - Variable Pitch (Collective)	
Cut in, out wind speeds	4.000 – 25.00	m/s
Rated wind speed	11.400	m/s
Nominal power	10.000	MW
Number of blades	3.000	-
Rotor diameter	178.300	m
Hub height	119.000	m
Drivetrain	Medium Speed, Multiple-Stage Gearbox	
Minimum Rotor Speed	5.000	rpm
Maximum Rotor Speed	9.600	rpm
Gearbox Ratio	50.000	-
Hub Overhang	7.100	m
Shaft Tilt Angle	5.000	deg
Rotor Precone Angle	-2.500	deg
Blade Prebend	3.332	m
Rotor mass (Blades + Hub)	230,667.000	kg
Nacelle mass (excl. rotor)	446,036.000	kg
Tower mass	429,181.900	kg
Structural design life time	20.000	years

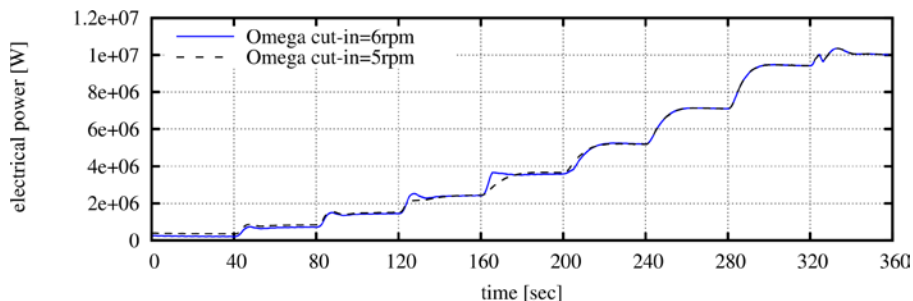


Figure 13 - Time series of the electrical power for the step-up load case for the 10MW DTU RWT mounted on a jacket at 50m water depth. The 2nd option (ω cut-in=5rpm) slightly increases the produced power in the low speed regime.

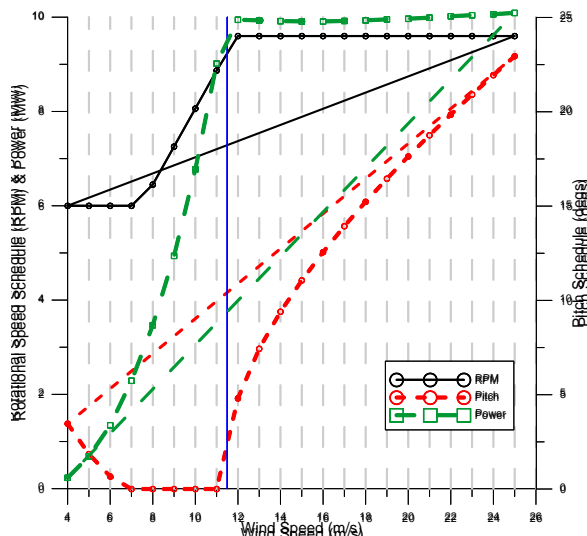


Figure 14 - Turbine rotor speed, blade pitch and electrical power over the wind speed. The blue vertical line distinguishes the variable speed part from the variable pitch part

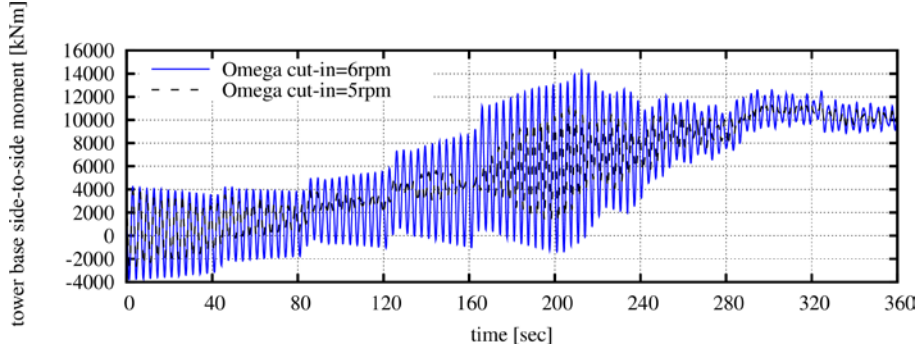


Figure 15 - Time series of the tower base side-to-side bending moment for the step-up load case for the 10MW DTU RWT mounted on a jacket at 50m water depth. The 2nd option (ω cut-in=5rpm) slightly reduces the side-to-side bending moment.

TASK 1.3 PRELIMINARY DESIGN OF MODULAR JACKET

For each of the six sets windfarm scenarios a preliminary design for a jacket structure serving as a substructure for a correspondent wind turbine generator is set up. These preliminary designs will serve as a basis for the more refined dynamic time-domain simulations to be conducted in Work Package 2.

The geometries of the preliminary jackets are based on Ramboll's experience gained from a large number of offshore wind jacket projects. Their geometries and properties follow the technical requirements set forth by DNV-OS-J101 0 and DNV GL-RP-0005 [7] with respect to e.g. minimum can and stub length, minimum brace angles or tubular steel cross-sections. The dimensions of leg, can and brace sections have been chosen in view of the prevailing loads generated by the WTG as well as the ocean environment considering both ultimate and fatigue limit state. For their assessment in regard to beneficial fatigue behaviour, resonance frequencies as well as the associated eigenmodes of each structure have been investigated as reported in the following sections.

The main output is the definition of the geometries of all six preliminary jacket designs along with diameter, wall thickness and arrangement of each pipe segment. The resulting six jacket geometries are detailed reported in the Deliverable 1.3.

JACKETS MAIN DIMENSIONS

The elevations of the jackets follow the water depth and maximum 50-years-wave crest. A summary of the main elevations is provided in Table 8 and they are set up according to Met-Ocean data analysis reported in the Deliverable 1.1. Because the maximum 50-years-wave crests for the North Sea locations are in the same region, the bottom of TP as well as the elevation of the interface to the tower is kept constant, whereas for the Mediterranean Sea the interface elevation can be lowered significantly due to the small 50-years-wave crest elevation. All elevations are denoted with regard to wrt, i.e. the seawater level of lowest astronomical tide (LAT).

Table 8 - Overview of elevations.

Location ID	mudline [m] wrt LAT	Top pf pile [m] wrt LAT	Bottom of TP [m] wrt LAT *)	Interface Elevation [m] wrt LAT	Jacket top width [m]	Jacket bottom width [m]
L4	-20	-18	19.0	23.0	14	20
L2	-30	-28	19.0	23.0	14	21
L3a	-40	-38	19.0	23.0	14	23
L3	-50	-48	19.0	23.0	14	26
L1	-60	-58	7.0	11.0	14	26

*) for simplicity the governing North Sea location (L4) is considered for all other North Sea locations (L2, L3 and L3a).

In order to reduce the vertical loading induced to the jacket legs at their upper end due to the turbine loads, an adequate width for the jacket top is chosen. However, the jacket top width is kept sufficiently slim to result in a reasonable size of the component linking the jacket to the wind turbine tower, denoted transition piece (TP). The jacket width is than widening linearly down to the mud line providing an increasing lever arm as the global bending moment resulting from turbine and wave loads increases. Thereby, the width is kept sufficiently small to avoid unfavourable resonance frequencies for the diagonal members (braces).

For an illustration of the elevations stated in Table 8, the 3D-geometry of jacket L4 located at 20m water depth is displayed in Figure 16

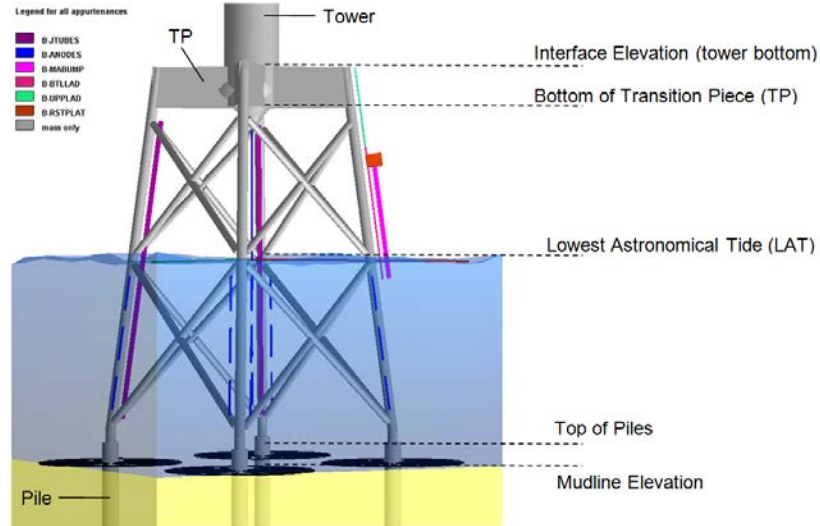


Figure 16 - Jacket 20m-10MW including typical appurtenances at location L4.

MODULAR JACKETS GEOMETRIES

For each component category (i.e. DK-joints, X-joints, DY-joints and tubular elements) a summary of different geometries (i.e. chord diameter, chord thickness, brace diameter, etc.) at the different scenarios has been done. The outcome is that the joints with the higher degree of recurrence are the X-joints for which there are some geometries that repeats in almost all the analysed windfarm scenarios (Table 9). It is not so for DK-joints and DY-joints that show poor or no repetitiveness throughout the different windfarm scenarios.

Table 9 - Offshore wind jackets X-joints geometries

Scenario	1st brace	2nd brace	3rd brace	4th brace	
	Section [mm]	Section [mm]	Section [mm]	Section [mm]	
20 m North Sea 10MW	Continuous intermittent	762x35 762x21	711x30 711x21	- -	- -
30 m North Sea 10MW	Continuous intermittent	762x35 762x21	711x30 711x21	711x30 711x21	- -
40 m North Sea 10MW	Continuous intermittent	914x35 914x21	762x35 762x21	711x35 711x21	- -
40 m North Sea 8MW	Continuous intermittent	762x35 762x21	711x35 711x21	610x30 610x21	- -
50 m North Sea 8MW	Continuous intermittent	914x35 914x21	762x35 762x21	711x35 711x21	610x35 610x21
60 m Mediterranean 8MW	Continuous intermittent	965x40 965x21	813x35 813x21	711x35 711x21	610x35 610x21

An analysis of the recurrence of the tubular elements geometries, cumulated for all the considered 6 windfarm scenarios, are reported in terms of external diameter OD and wall thickness WT (Figure 17).

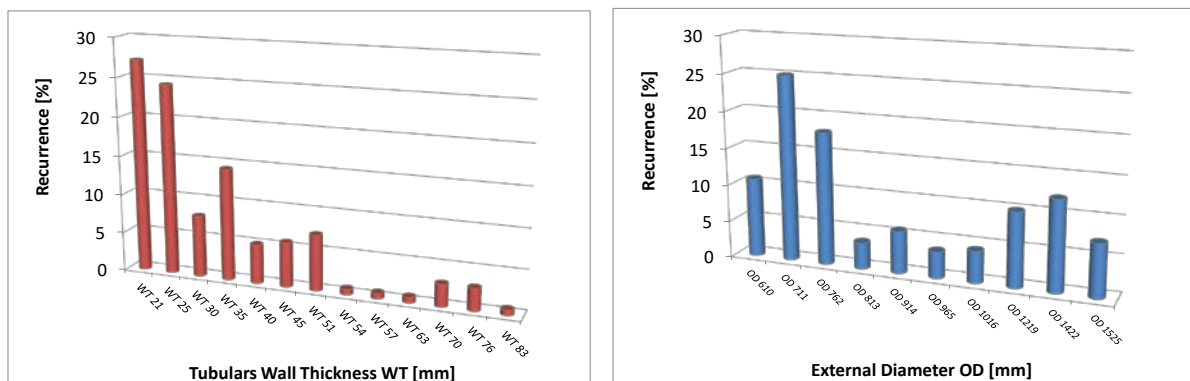


Figure 17 - Recurrence of pipe geometries cumulated for the 6 windfarm scenarios.

WP2 - MODULAR JACKET LOAD ANALYSIS

OBJECTIVES AND MAIN OUTCOMES

The aim of this WP2 is to produce the history loads relevant to the six (6) windfarm scenarios analysed via processing the load cases according to IEC 61400. In particular:

- Development of the coupled turbine/jacket model for the 8MW and 10MW OWTs
- Time domain simulations for 8MW and 10MW turbines in 6 different water depths, estimation of the internal loads at the joint-connections
- Calculation of hot spot stress histories for the X joints selected for fabrication for all the six (6) wind farm scenarios and relevant damage factor.

TASK 2.1 FULLY-INTEGRATED TURBINE-MODULAR JACKET MODEL

INTEGRATED LOAD SIMULATION TOOL FOR 8MW TURBINE-JACKET MODEL

The load simulation tool set up by Ramboll is based on a sequential integration approach comprising a dynamic wind turbine model along with a superelement approximation of the detailed jacket model under due consideration of dynamic wind and wave load excitation and structural response. The wind turbine model and the controller characteristics are described in reference. All analyses are carried out with the programs ROSA and LACFlex by Ramboll. The superelement is derived using the combined static and modal reduction method according to Craig-Bampton [19]. The overall load iteration procedure is shown in Figure 18 and consists of the following three main steps:

1. Generation of the superelement including wave loads in ROSA
2. Integrated load analysis considering wind and waves in LACFlex
3. Post-calculation to obtain local member loads in ROSA

This procedure is carried out in the time domain for each design load case combination of wind and wave input. Consistency between the applied models of the foundation and the wind turbine is achieved by alignment of masses, modal properties (natural frequencies) and the damping parameters prior to the processing of load cases.

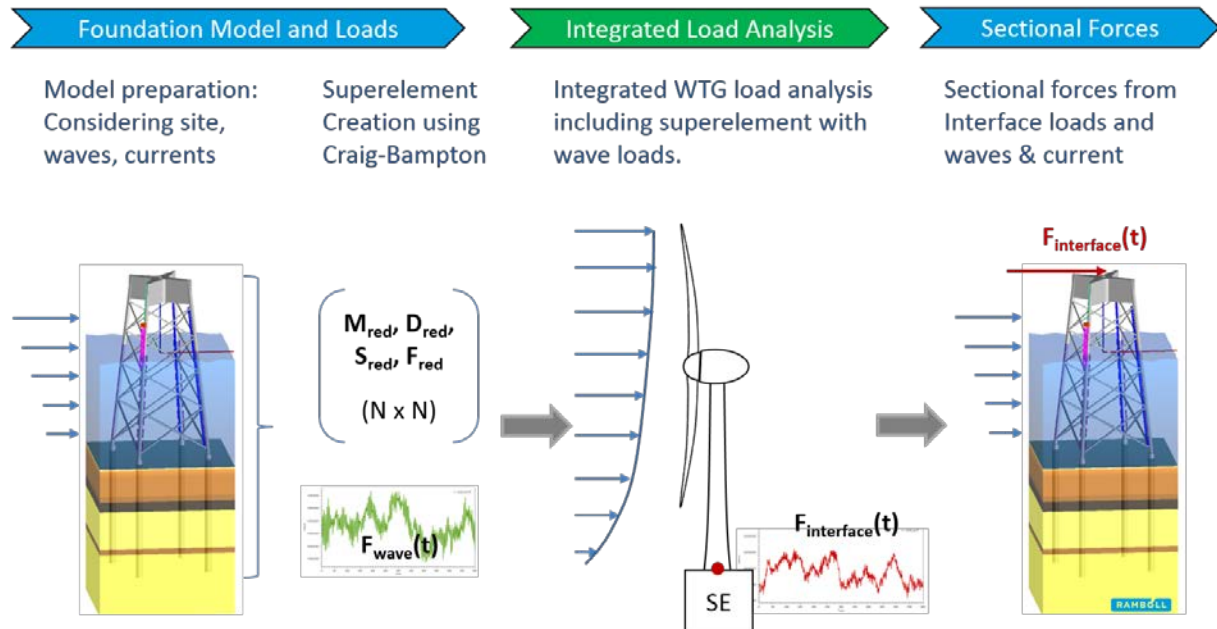


Figure 18 - Load calculation procedure.

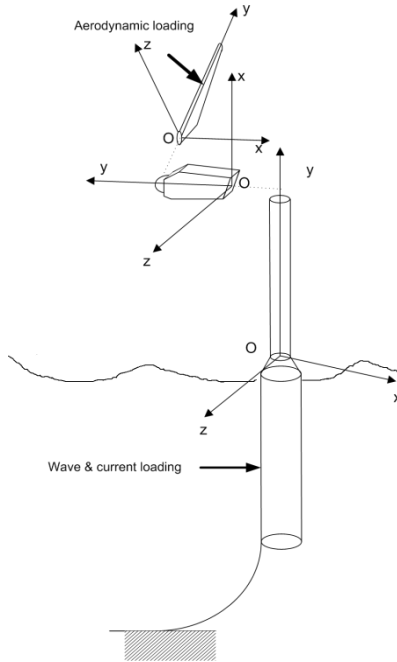
The superelement model uses a Rayleigh damping approach describing the damping of the model as a linear combination of the mass and stiffness properties, sometimes also called alpha and beta proportional damping. The required parameters depend on the natural frequencies of the first two characteristic bending modes of the entire model, i.e. wind turbine and support structure.

In contrast, the damping of the wind turbine model is based on modal damping which can be specified for each mode separately. The combination of both subsystem models (i.e. wind turbine and jacket) leads to a reduced total damping. This can be compensated by increasing the tower modal damping in order to reach the specific target damping of the full model while the damping of

the detailed jacket model remains unchanged and thus ensures consistency for the post-calculation of the jacket.

INTEGRATED LOAD SIMULATION TOOL FOR 10MW TURBINE-JACKET MODEL

NTUA is participating in JABACO project with hGAST, an in-house developed hydro-servo-aero-elastic software for the design and verification of wind turbines. It is used for performing nonlinear time domain simulations of the coupled structure, as well as eigen-value and stability analysis. hGAST is modular comprising:



- the ‘dynamic module’ that defines the dynamics of the whole system.
- the “structural module” that provides the deformed shape and the associated kinematics defined for each separate solid component of the machine.
- the “aerodynamic module” that provides the aerodynamic loads along the rotor blades.
- the “hydrodynamic module” that provides the wave¤t loading on the support structure.
- the “control module” that provides the operational conditions for the wind turbine (blades’ pitch angle and generator torque demand) regulating the power output.

Figure 19 - Physical modeling in hGAST

TASK 2.2 TIME DOMAIN DYNAMIC ANALYSIS

ANALYSIS OF 8 MW SCENARIOS

The set-up and results of the time domain dynamic analysis for the design locations of the 8MW wind turbine are described in this chapter, namely for locations

- L1, 60m water depth, Mediterranean
- L3, 50m water depth, North Sea
- L3a, 40m water depth, North Sea.

As a basis for the evaluation of the load cases to be dynamically analysed in the time domain a specific load case table is set up for each evaluated location. The jacket design is usually driven by wind fatigue loads of the turbine under operation and during idling. Therefore, the design load cases (DLC) 1.2 and 6.4 according to IEC61400-3 are considered. For each of these general load case groups a great number of different combinations of wind speed, wind direction, wave height, wave direction, wave period and yaw error may be found and assessed. Each such combination is referred to as a load case in the following. A 10-minute transient simulation is conducted for each considered load case.

An overview of the 456 load cases that have been considered in the given context is given in Table 10. 264 load cases of type DLC 1.2 representing production loads and 192 load cases of the type 6.4 representing idling loads are considered. The term idling refers to situations where no power is produced due to either extremely low or extremely high wind speeds or due to technical downtimes. A wide range of combinations of different wind speeds and wind directions is taken into

account. A yaw error of 8 degree, i.e. the turbine pointing not directly to the direction of the incoming wind but slightly deviating from that direction by a certain amount, was considered for the DLC 1.2 load case group which has a higher contribution to the overall damage. However, the effect of the yaw error is known to be rather minor in the context of jacket loads.

The direction of the wave state is assumed to be aligned to the wind direction for all load cases. For each combination of wind speed and wind direction one specific sea state is chosen based on the met-ocean data provided in Deliverable 1.1, each sea state being described by a significant wave height as well as the peak period of the wave period in the applied Jonswap wave spectrum.

Table 10 - Overview of the considered load cases

Load case group	Wind speed v_w	Direction	Wind-wave direction	Yaw error	Sig. wave height	Wave period	Number of time series
1.2	4 – 24 m/s	0-330°	Aligned	0° / 8°	f(v_w)	f(H_s)	264
6.4	2 – 30 m/s	0-330°	Aligned	0°	f(v_w)	f(H_s)	192

For the allocation of significant wave heights, H_s , to specific combinations of wind speed, v_w , and wind direction the results from an evaluation of the met-ocean data for location L1, L3 and L3a is documented in Deliverable 2.2. The allocation is based on combinations with maximum probability of occurrence.

For the allocation of peak periods, T_p , to specific combinations of significant wave height, H_s , and wind directions corresponding results for location L1, L3 and L3a are analysed. Again, the allocation is based on combinations with maximum probability of occurrence. By use of the data so allocated all load cases generally described in Table 10 can be clearly defined. An exemplary listing of the considered load cases for locations L3 is documented in Appendix B of Deliverable 2.2.

For the interpretation of each load case the definition of the wind and wave direction is of great interest. All wind and wave met-ocean data is given in the compass coordinate system. Wind and wave directions are given with respect to geographic North. The global x-axis is pointing towards North, the global y-axis is pointing towards West.

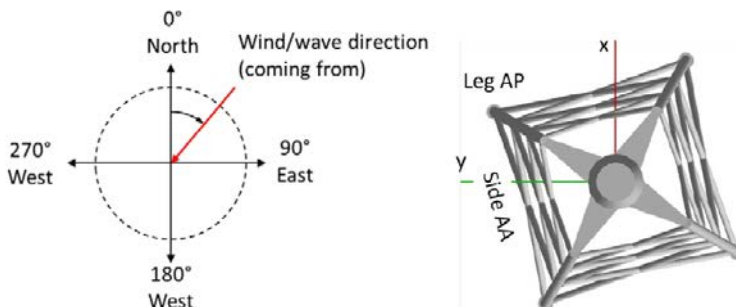


Figure 20 - Definition of wind and wave directions

The result of each performed simulation consists of time series of sectional forces (F_u , F_v , F_w , M_u , M_v , M_w) for all jacked members. These are reported for all attached beams at all K-, Y- and X-joints. As an illustration of the obtained results the first 20 seconds of the time series of all six sectional forces (three sectional forces and three sectional moments) for load case 117 are plotted in Figure 21 and Figure 22, respectively. As can be extracted from Appendix B of Deliverable 2.2, by this load case a load situation comprising a medium wind speed of 12 m/s, a wind/wave direction of 300° and no yaw error is simulated. The modelled coexisting sea state is characterised by a significant wave height of 1.5 m/s as well as a peak period of 6s. This is also reflected in Appendix B of Deliverable 2.2.

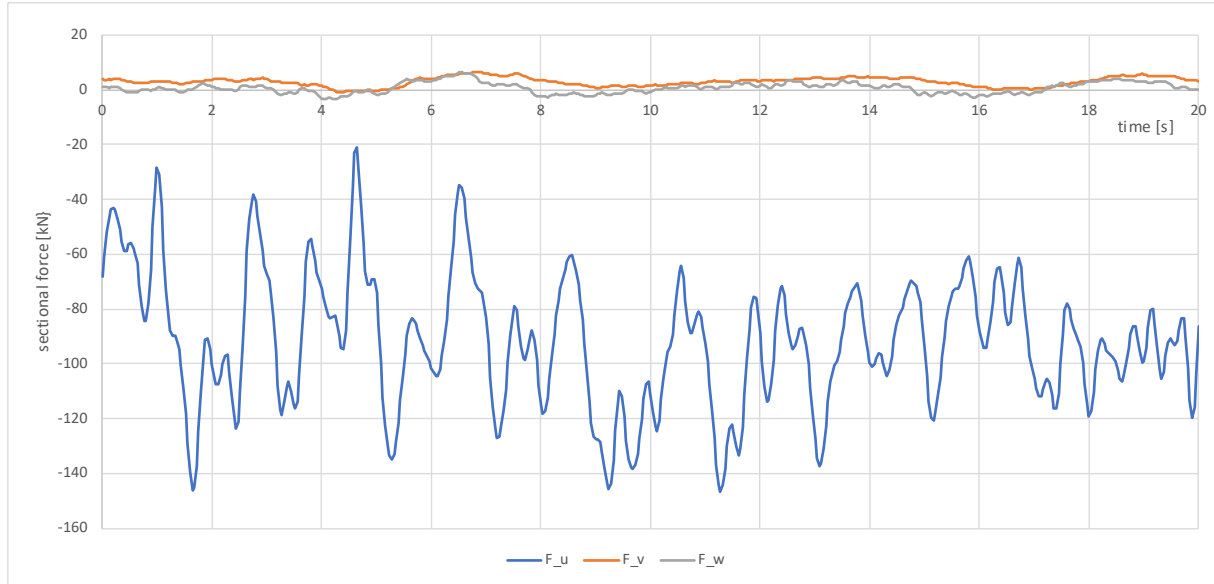


Figure 21 - Beginning of the resulting time series of sectional forces at the connection of beam 5 to the K-joint node 30 of the jacket at location L3 (50 m water depth, North Sea) for load case 117

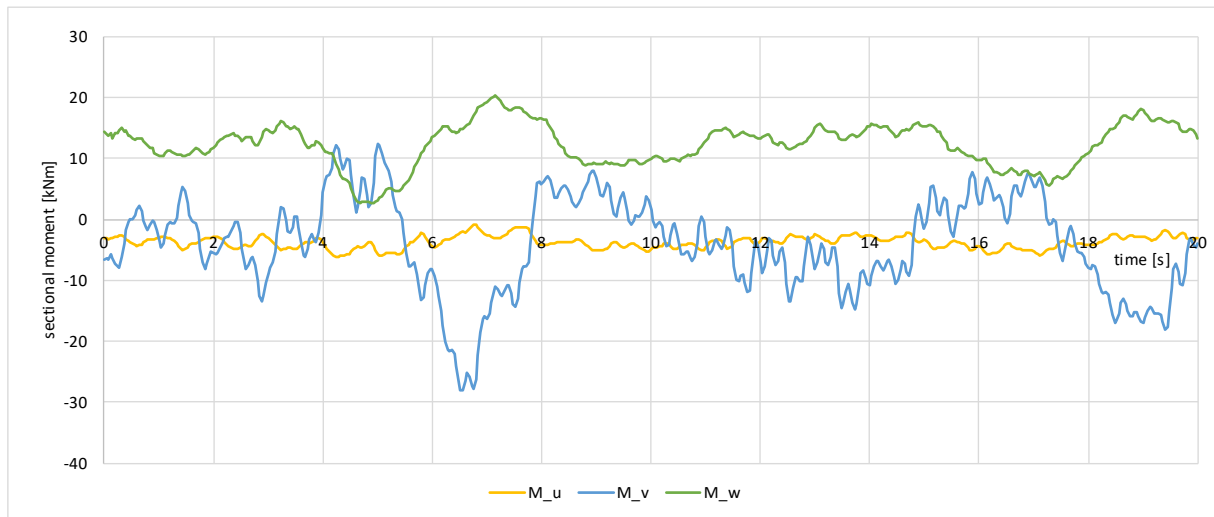


Figure 22 - Beginning of the resulting time series of sectional moments at the connection of beam 5 to the K-joint node 30 of the jacket at location L3 (50 m water depth, North Sea) for load case 117

For the evaluation of the provided results of the time domain dynamic analysis in addition to the time series of sectional forces the probabilities of occurrence for each load case also need to be known. These numbers have been extracted from the met-ocean data along with the derivation of the load cases and are provided in Deliverable 2.2..

It should be noted that power production takes place at mean wind speeds between 4 and 24 m/s, only [6]. For these wind conditions a probability of power production of 95% is assumed. For cases where no power is produced due to adverse wind conditions or downtimes the turbine is assumed idling. The probability of occurrence for each load case is also added to the load case table as presented for location L3 and L3a in Appendix B of Deliverable 2.2. Please note that the probabilities for the production load cases (DLC 1.2) are equally distributed to the two load cases comprising yaw errors of 0° or 8°.

ANALYSIS OF 10 MW SCENARIOS

Time domain hydro-servo-aero-elastic simulations of the coupled structure (including the DTU 10MW turbine and the modular jacket for the 3 considered water depths) have been performed using hGAST in-house tool, in order to estimate the internal loads at the joint-connections.

Table 11 presents the met-ocean data for the 3 considered sites, by processing the data provided in Task1.1. The most probable set of wave peak period T_p and significant wave height H_s is given for each wind speed at hub height (the wind speed initially is provided at $z=10m$ and transformed to $z=120m$ using the log-law with a shear constant=0.14). Also in this table the probability of each wind speed is given, needed for the estimation of the lifetime fatigue equivalent loads.

In order to come up with a unique set of T_p and H_s per wind speed applicable to all 3 sites, which are very close all in the North Sea, the mean value is calculated as shown in Table 11. In the same table the turbulence intensity TI of the wind is also provided, defined based on IEC standards for a WT of class IIB. For a IIB-class site the reference wind speed is 43m/s and the TI is 0.14.

Table 11 - Met-ocean data for the 3 sites in North Sea for the 10MW WT and average values used in the first analysis

L4, d=20m				L2, d=30m				L3a, d=40m				time-domain simulations		
Uhub [m/s]	Tp [s]	Hs [m]	Prob [%]	Tp [s]	Hs [m]	Prob [%]	Tp [s]	Hs [m]	Prob [%]	Tp [s]	Hs [m]	TI: class IIB		
3.00	4.62	0.41	8.11	4.47	0.34	8.46	4.45	0.33	3.68	-	-	-		
5.00	5.22	0.51	11.13	4.78	0.50	11.45	4.74	0.53	9.15	4.91	0.51	26%		
7.00	4.77	0.62	14.72	4.32	0.58	15.41	5.19	0.73	12.86	4.76	0.64	22%		
9.00	4.32	0.72	16.38	4.32	0.75	16.40	5.04	0.93	14.38	4.56	0.80	19%		
11.00	4.77	1.04	15.82	4.78	1.00	15.06	5.34	1.13	14.92	4.96	1.05	18%		
13.00	5.22	1.35	12.59	5.23	1.33	12.60	6.24	1.63	13.75	5.56	1.43	17%		
15.00	6.28	1.97	9.45	6.29	1.99	9.06	6.09	1.83	10.99	6.22	1.93	16%		
17.00	6.28	2.18	6.08	6.29	2.24	5.79	6.83	2.43	8.31	6.47	2.28	15%		
19.00	6.88	2.70	3.37	6.90	2.82	3.41	7.73	3.23	5.79	7.17	2.92	15%		
21.00	8.24	4.06	1.55	7.65	3.73	1.66	7.73	3.53	3.38	7.87	3.77	14%		
23.00	9.29	5.31	0.55	8.56	5.05	0.48	8.48	4.43	1.83	8.78	4.93	14%		
25.00	9.29	6.04	0.18	8.71	5.30	0.18	9.22	5.43	0.66	9.08	5.59	14%		
27.00	9.29	6.25	0.05	9.17	6.12	0.03	9.67	6.43	0.21	-	-	-		
29.00	8.08	4.48	0.01	8.56	5.46	0.00	10.27	7.63	0.06	-	-	-		

A reduced matrix of design load cases (dlc) based on IEC standard has been defined as shown in Table 12. Dlc1.2 corresponds to the normal operation of the WT in normal turbulence conditions and normal sea state (Table 11) and is used for estimating the fatigue limit state. For normal operation simulations have been performed for wind speeds [5-25m/s] with a step of 2m/s and wind direction (yaw angle) equal to zero. DLCs 6.1 and 6.2 correspond to storm conditions at which the WT idles at the wind speed of 43m/s, with 90deg blade pitch and considering a severe sea state ($H_s=10m$, $T_p=13.5$). In DLC 6.1 yaw controller of the nacelle operates and thus wind is normal to the rotor plane. 3 wave directions have been considered (0, 22.5 and 45deg) and 2 yaw errors (0, 8deg). On the other hand in DLC 6.2 yaw controller is not available and so 9 wind directions have been considered [-60-60deg] with a step of 15deg, while the wave is codirectional with the wind. DLCs 6.1 and 6.2 are used for estimating the ultimate limit state. For each case one 10min realization has been performed.

The output of the simulations is time-series of internal generalized loads (3 forces and 3 moments) at the joint connections of the jacket support structure and the wind turbine members (tower, drive-train and blades). This data has been shared to the project in ascii-format and will be used in Task 2.3 for the stress estimation at the joint connections of the modular jacket.

In Table 13 the maximum absolute value of the internal loads, from the DLCs of Table 12, is presented, after transforming them into stresses by dividing the loads by the cross section area. For each different joint-connection, i.e. DY-joint, DK-joint and X-joint, the maximum stress is presented from the 4 same joints per vertical station. The number referring to the brace is linked to the vertical z level and has been defined in Task 1.3 in which the definition of the jackets was provided. It is noted that the safety factors that are associated to every DLC have been applied, while no correction for 3D stress concentration is applied. The presented signals are the local stresses at every cross section originating from the axial and the normal forces and moments. The maximum stress at every joint is estimated by comparing the stresses of all the members associated to each joint connection (4 members for the X-joints and Y-joints and 6 members for the K-joints).

Table 12 - DLCs definition

DLC	Conditions	runs/depth	Safety Factor
1.2	11bins [5:25,2m/s], 1yawerr [0deg]	11	1.35
6.1	1bin [43m/s], 3wave dirs [0,22.5,45deg] x 2yawerr [0,8deg]	6	1.35
6.2	1bin [43m/s], 9wind dirs [-60:60,15deg]	9	1.1

Table 13 - Maximum absolute values of the stresses for each joint-type of the jacket for the 3 water depths

JB2010 20 m North Sea - 10MW						
Joint	Brace level	z [m]	sFa [kPa]	sFn [kPa]	sMa [kPa]	sMn [kPa]
DY	1	-16.304	196359	12762	7114	22388
X	1	-6.370	50763	4419	3008	20248
DK	1	2.175	232039	6905	3385	25574
X	2	10.713	42638	3713	2638	12707
DY	2	17.800	205243	11534	5015	15723

JB3010 30 m North Sea - 10MW						
Joint	Brace level	z [m]	sFa [kPa]	sFn [kPa]	sMa [kPa]	sMn [kPa]
DY	1	-26.104	144522	8438	4067	11768
X	1	-17.355	51840	2021	1619	10043
DK	1	-9.573	299601	3610	2328	13692
X	2	-1.830	41438	3177	1682	11138
DK	2	4.987	198923	5025	3011	16118
X	3	11.841	41293	4125	2001	12491
DY	3	17.800	169567	10016	3584	23601

JB4010 40 m North Sea - 10MW						
Joint	Brace level	z [m]	sFa [kPa]	sFn [kPa]	sMa [kPa]	sMn [kPa]
DY	1	-35.904	102072	6059	3011	9393
X	1	-24.668	49881	1900	1644	9447
DK	1	-15.080	112224	2994	1598	11549
X	2	-5.533	43293	2554	1460	8380
DK	2	2.620	150230	4125	2919	13348
X	3	10.811	44513	3593	1630	11509
DY	2	17.800	142544	8533	4035	27326

TASK 2.3 DETERMINATION OF LONG-TERM HOT SPOT STRESS RANGE ANALYSIS

The load resultants of each Jacket were delivered by elaborating 600 seconds of time-history of axial forces, transverse forces and bending moments of all elements. These data have been provided for the different wind speed considered at design stage, ranging from 5m/s to 25m/s. The loadings coming from the different wind conditions are combined using long-term wind speed probability distributions obtained by met-ocean data analysis of the different locations.

The Rainflow cycle counting method has been applied to obtain the stress histograms useful to determine the fatigue life at each node. The Rainflow method according to ASTM E1049-85, and presented in Nieslony (2009), was adopted.

In the following figures the obtained hot spot stress histograms are reported for each windfarm scenario analysed. The delegate X-joint and hot spot location have been selected on the basis of most critical among the many different considered.

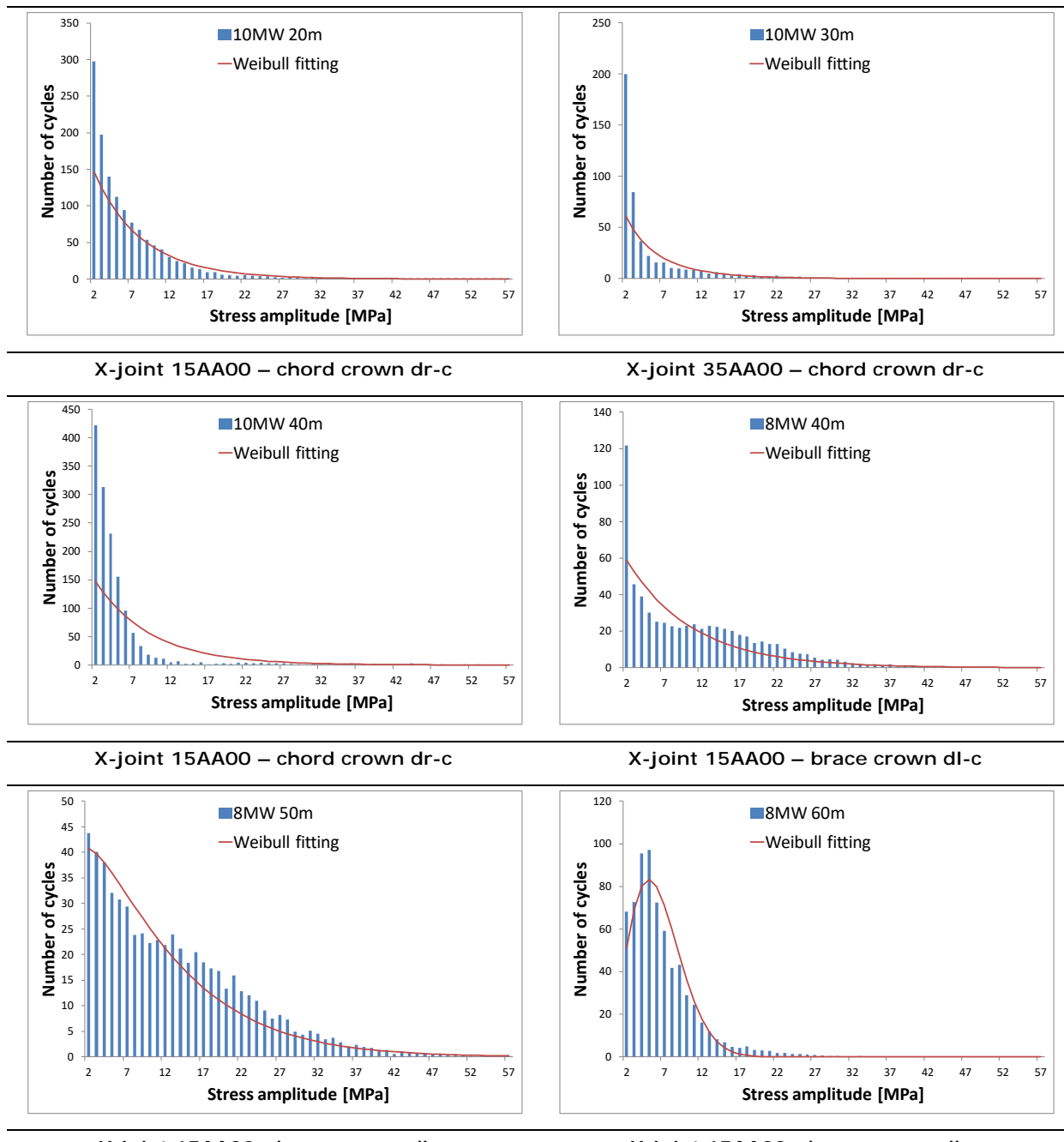


Figure 23 – Hot spot stress histograms relevant to most critical X-joint location per windfarm scenario.

The damage factor was calculated for 1 year time period and then was linearly extrapolated for 20 and 30 years.

Fatigue strength curves have been used for the analysis of the six different Jackets. In the framework of this research effort the fatigue strength curves proposed by ISO 19902, DNV-RP-C203 and API-RP-2A have been used and compared.

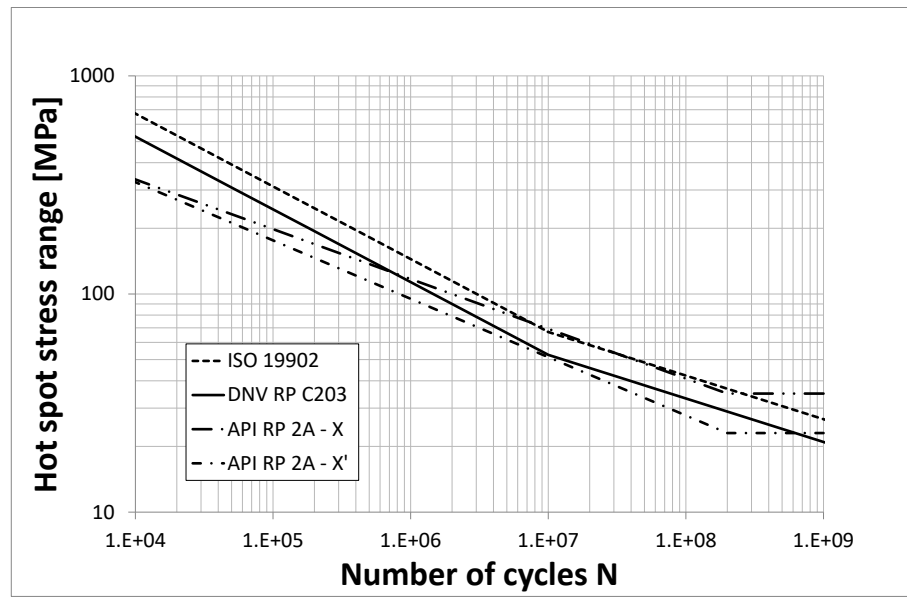


Figure 24 – Comparison among different fatigue designS-N curves for offshore tubular connections.

In Figure 25 the damage factors of the critical X-joint of each jacket are presented, considering the SCFs calculated with analytical expressions.

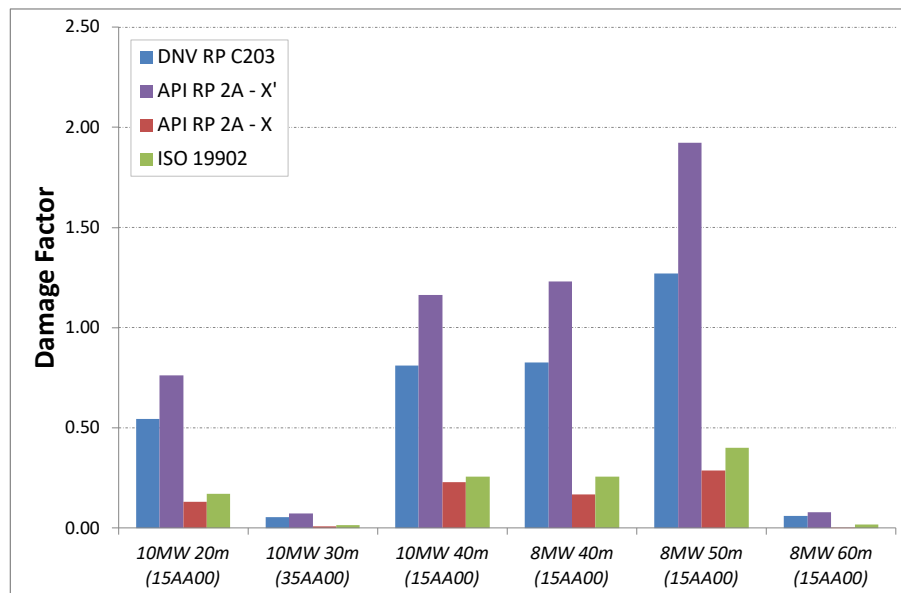


Figure 25 – Damage Factors of selected critical locations.

WP3 - DESIGN OF THE FOUNDATION OF THE MODULAR JACKET

OBJECTIVES

The WP3 aims to:

- (i) propose and validate a numerical methodology to analyse foundation response; investigate piled foundation performance under normal and extreme loading scenarios (Task 3.1)
- (ii) finite element analysis response of alternative suction caisson foundation typology (Task 3.2)
- (iii) investigate the effect of foundation type (piles or suction caissons) on the jacket performance with special consideration to seismic robustness (Task 3.3).
- (iv) develop handy design charts to be used for the preliminary design of jacket foundations for the wind farm scenarios of the JABACO project (Task 3.4)

TASK 3.1 IDENTIFICATION OF THE MOST APPROPRIATE FOUNDATION SYSTEM

Foundation design was performed at Ultimate Limit State (ULS) conditions considering Consequence Class 2 (API RP 2A-WSD (2000), DNV-OS-E301 (2010)). A uniform profile of medium-loose sand of $\varphi=35^\circ$ ($\delta=25^\circ$), $G_0 = 10000(\sigma_v)^{0.5}$ and $\gamma_{\text{sat}} = 20 \text{ kN/m}^3$ has been considered.

The proposed numerical methodology was validated able to rigorously capture the prevailing load-carrying foundation mechanisms. The Numerical simulations involved 3-dimensional F.E. configurations analyzed in the ABAQUS code. The geometry and mesh configuration (for a typical pile foundation) is presented in Figure 26. The soil body is modeled using 8-node hexahedral continuum elements (C3D8), while linear elastic surface elements (S4) are used for the tubular pile. Sliding and detachment of the pile from the surrounding and encased soil is captured through special interface elements placed at the internal and the external pile periphery. Sensitivity analysis was performed to decide upon the optimized configuration that reduces analysis effort without compromising accuracy.

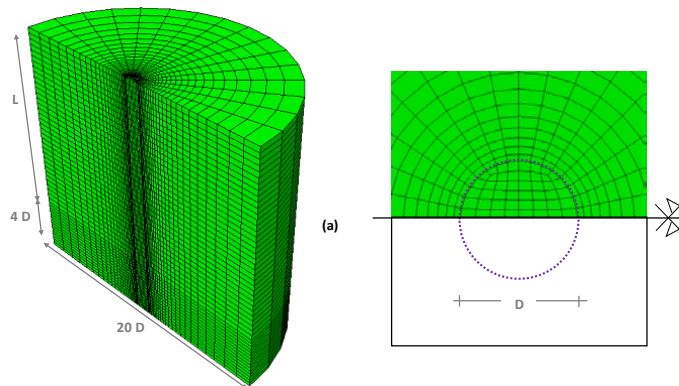


Figure 26 - Numerical Methodology FE Mesh.

To simulate the non-linear behaviour of sandy materials, a pressure dependant Von Mises plasticity model with nonlinear kinematic hardening is implemented. The yield stress at saturation is defined as a function of the confining pressure (octahedral stress) and the friction angle φ . Three possible yield criterions are examined: Model C, where the yield circle circumscribes the Mohr-Coulomb shaped hexagonal pyramid (compressive meridian matching) in the π -plane; Model T, where the hexagonal pyramid is inscribed by the circle (tensile meridian matching), and Model CT, where the circle lies between the aforementioned two circles (Figure 27). A user subroutine is incorporated in Abaqus which relates the model parameters to the vertical stress and the principal stresses.

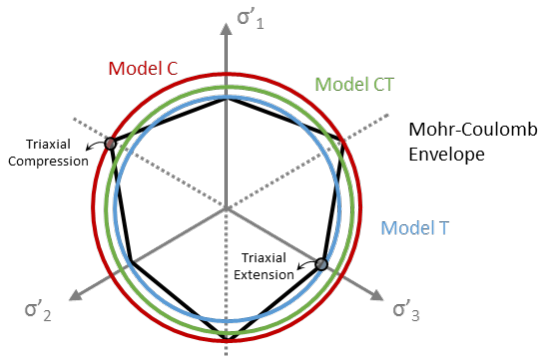


Figure 27 - Representation on the n -plane of the Mohr-Coulomb yield criterion and the three assumed yield criteria of the kinematic hardening model

The numerical methodology is validated against API calculations and centrifuge experiments (Rosquoët et al, 2004) as reported in Figure 28.

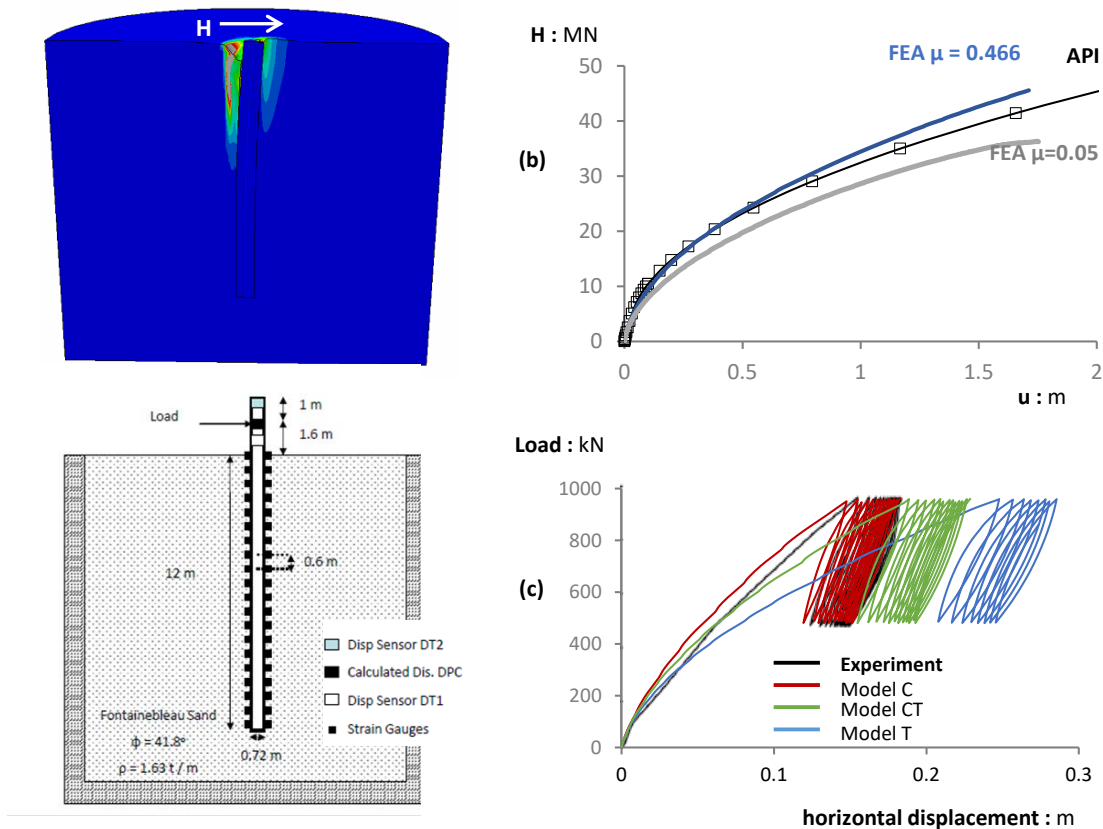


Figure 28 - Numerical Methodology validation against (b) API and (c) centrifuge experiments Rosquoët et al (2004).

Validation of our FE models against the Centrifuge Experiment shows that Model C outperforms the other two, accumulating less displacement throughout the cyclic loading phase and capturing closely the system's stiffness at relatively large strains. However, at smaller strains (at pile displacements $\delta \approx 0.05$ m, i.e. the range where the turbine is expected to work), Model CT displays marginally superior behavior.

FE analyses are also compared to simplified beam-on springs calculations where soil reactions are replaced by evenly distributed non-linear springs along the pile length ('p-y' springs). For $z/D > 2.5$, the maximum per length soil lateral resistance calculated by FEA is higher than the code specification, while the FEA systematically presents a far more flexible response.

The validated model was implemented to analyse the response of the entire soil-foundation-Jacket-OWT System under the combined action of environmental loads. Results were compared with those obtained from simplified beam-on springs calculations (Figure 29) where soil reactions are replaced by evenly distributed non-linear springs along the pile length ('t-z', 'p-y' springs). The seismic performance of jackets was analysed performing fully coupled 3D time-history analyses. Both piled foundations and suction caissons had been considered and structural performance was judged on

the basis of maximum and/or residual foundation deformations and how the latter compare to specified design limits.

The coupled FEA were found to compare satisfactorily well to simplified design procedures. Comparison is better under NC, while for extreme environmental loading, the simplified approach tends to overestimate deformations (Figure 29).

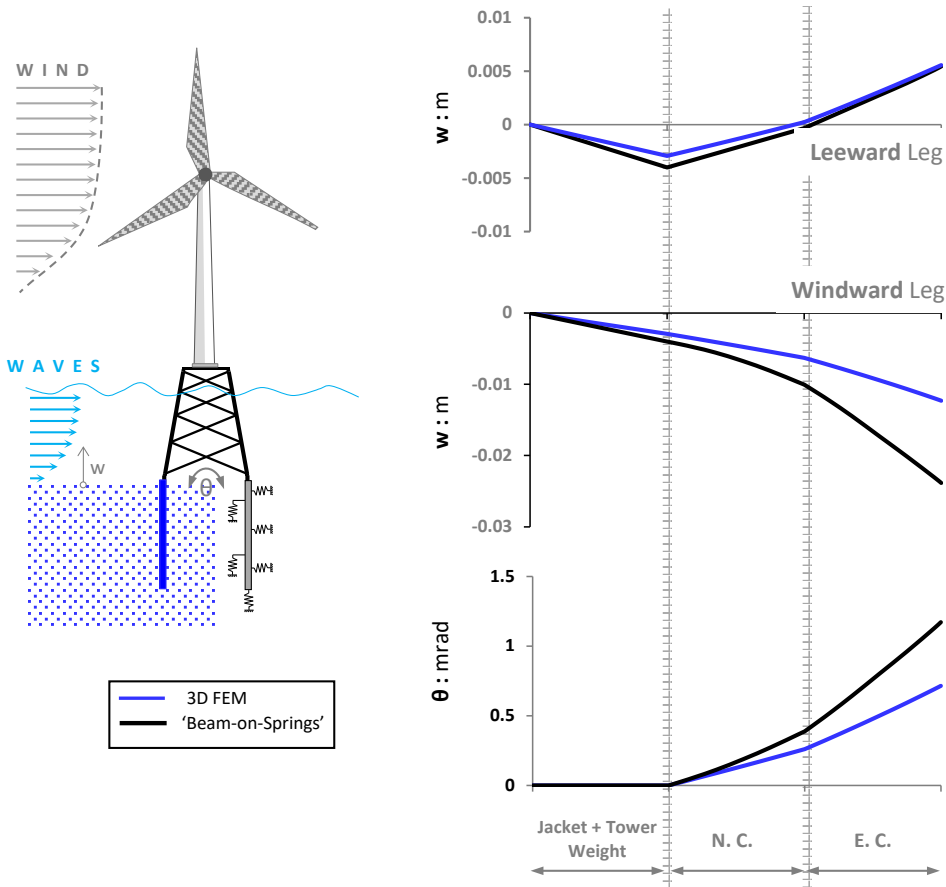


Figure 29 - Performance of OWT on Jacket Platform for monotonically increasing values of wind and wave loading. Comparison between 'Beam-on-Springs' and coupled 3D FEM: vertical displacements at the leeward and windward legs and jacket rotation.

TASK 3.2 COMPREHENSIVE FE ANALYSIS OF SELECTED FOUNDATION SYSTEMS

An alternative foundation solution is discussed herein, that of a suction caisson. It comprises a shallow circular footing of diameter (D) whose capacity is enhanced by means of peripheral embedded skirts that confine the internal soil thereby creating a soil plug. Ease of installation is the main advantage of this foundation type. The process consists of floating the caisson to its location where it is driven into the seabed under the action of its self-weight and pumping of water trapped within the skirts. The differential pressure due to pumping creates suction, which attracts the caisson lid downwards until it attains full contact with the soil. In applications where the vertical capacity of the foundation is the decisive design parameter, the length of the skirts is of the order of $L=3D - 4D$.

A key benefit of skirted foundations over conventional embedded foundations lies in their ability to resist uplift owing to negative excess pore water pressure (i.e. suction) developed within the confined soil plug. If passive suctions can be maintained, reverse end bearing will govern uplift resistance.

Controversy exists among the scientific community on whether these passive suctions may indeed be reliably considered throughout the life-time of the foundation. Code provisions are advising to ignore the positive role of suction in foundation design, so accordingly, the results presented herein are assuming zero-suction conditions between the soil plug and the peripheral skirts.

A view of the FE model is depicted in Figure 30. The foundation is a deep suction caisson with diameter $D = 7$ m, and embedment ratio $L/D = 3$. The soil is modeled with eight-node hexahedral

non-linear continuum elements (C3D8) that follow the C constitutive model. The caisson is modeled with linear elastic shell elements. External boundaries were set sufficiently remotely from the foundation to ensure no boundary effects on the foundation response. No cavitation between the caisson and the internal soil is assumed. For the simulation of contact between the caisson and the encased/surrounding soil, special-purpose contact elements are implemented that allow sliding as well as detachment.

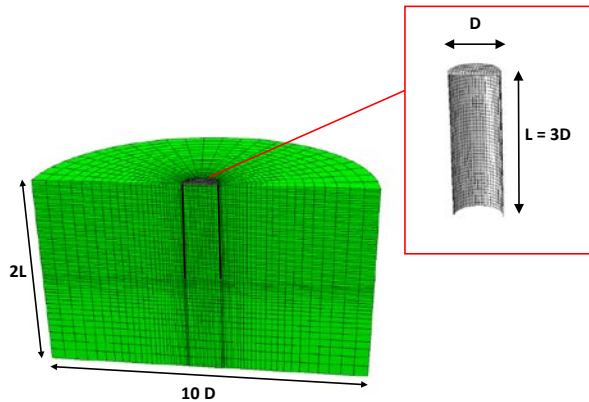


Figure 30. Suction Caisson with $L/D=3$: finite element mesh configuration.

The bearing mechanism of suction caissons was found to be controlled by the properties at the soil-caisson interface. Under perfectly "sealed" conditions (i.e., when suction may be granted), a "reverse end bearing" mechanism is mobilized accompanied by significantly higher resistance values. If the "sealing" is inefficient (i.e., in case of improper installation or when the soil permeability is very high to sustain suction), resistance values reduce as failure occurs only in the form of sliding along the caisson sidewall. For typical soil profiles and caisson dimensions, this decrease may be as high as 40% of the nominal value (assuming full suction) – Figure 31.

The jacket performance is only marginally affected by the assumed suction conditions. At Normal Sea State, the jacket response under 'suction' or 'no-suction' assumption is completely identical, while even for extreme environmental loads, the differences in the response are not that important. The beneficial effect of suction was found to be marginal also for seismic loading combinations.

Overall, in terms of foundation performance the jacket platform is a very redundant system. Even when the axial capacity at its supports is fully exhausted (i.e., in case the assumed wind and waves loads are excessively higher than the design loads), the jacket will not immediately fail. Instead it will continue sustaining loading through bending, mobilizing resistance along the shaft periphery of the foundation piles or the caissons.

No specific advantage was revealed by using piled foundations instead of suction caissons.

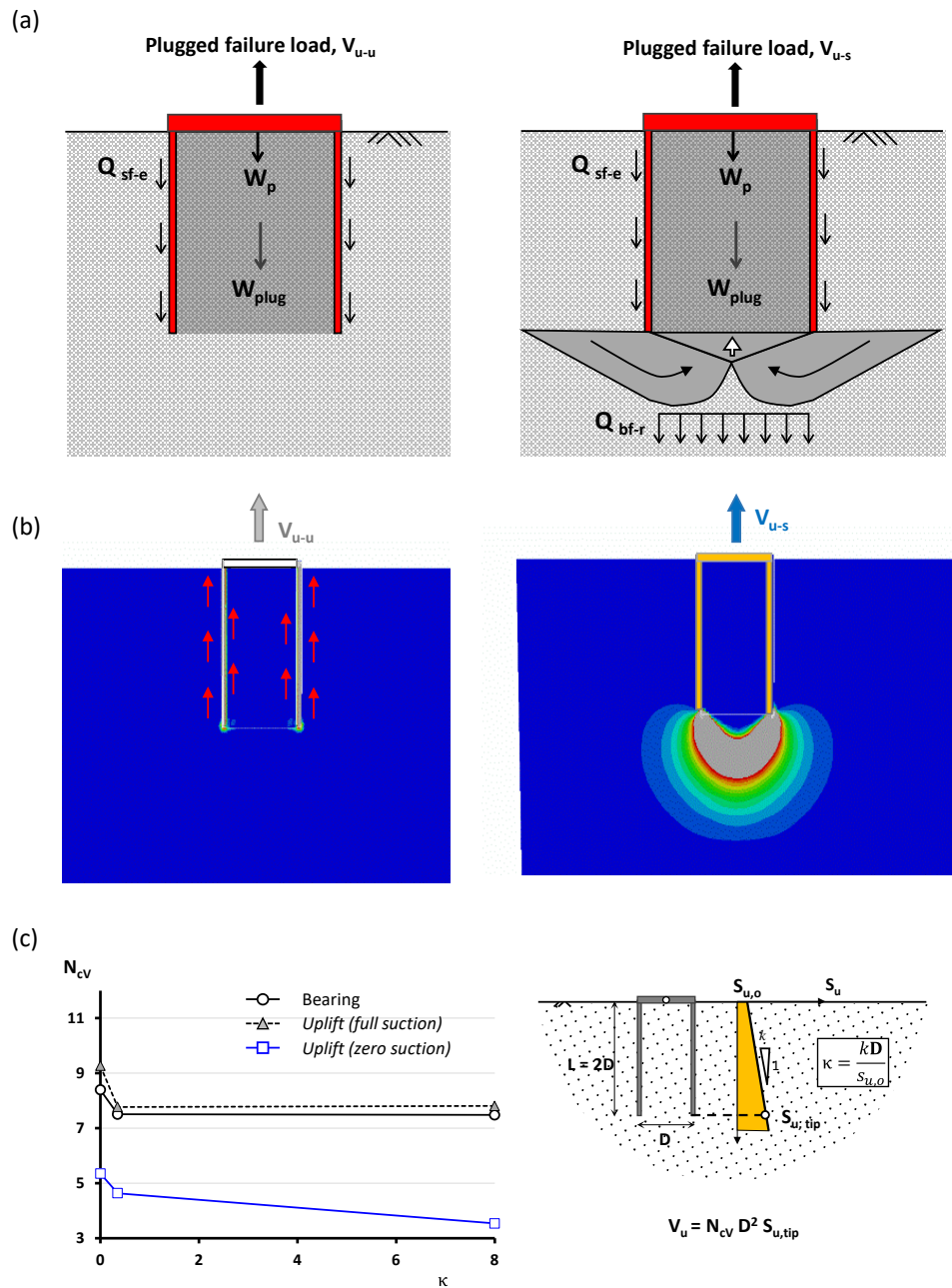


Figure 31 - Uplifting resistance of suction Caisson in clays: (a) theoretical bearing mechanisms assuming no-suction and full-suction conditions; (b) numerical modeling: snapshots of plastic deformations; (c) effect of suction conditions on the axial bearing capacity of caissons with $L/D=2$ for different levels of soil inhomogeneity

Task 3.3 FOUNDATION RESPONSE IN ACCOUNT OF DYNAMIC SOIL-STRUCTURE INTERACTION

An intriguing comparison of 10^{MW} OWT in the seismic Mediterranean Sea location, supported by 4-legged jacket either on piles or suction caisson has been performed.

OWTs (being extremely flexible) are generally insensitive to ground shaking when subjected to pure earthquake loading (Figure 32).

Alarming conditions for the operability of the turbine may arise when seismic shaking is combined with a non-zero wind force acting at the top of the tower. This wind-induced asymmetry, coupled with the kinematically-generated stressing on the foundation, tends to trigger increasingly high rates of accumulated rotation throughout the duration of the strong seismic shaking (Figure 32b).

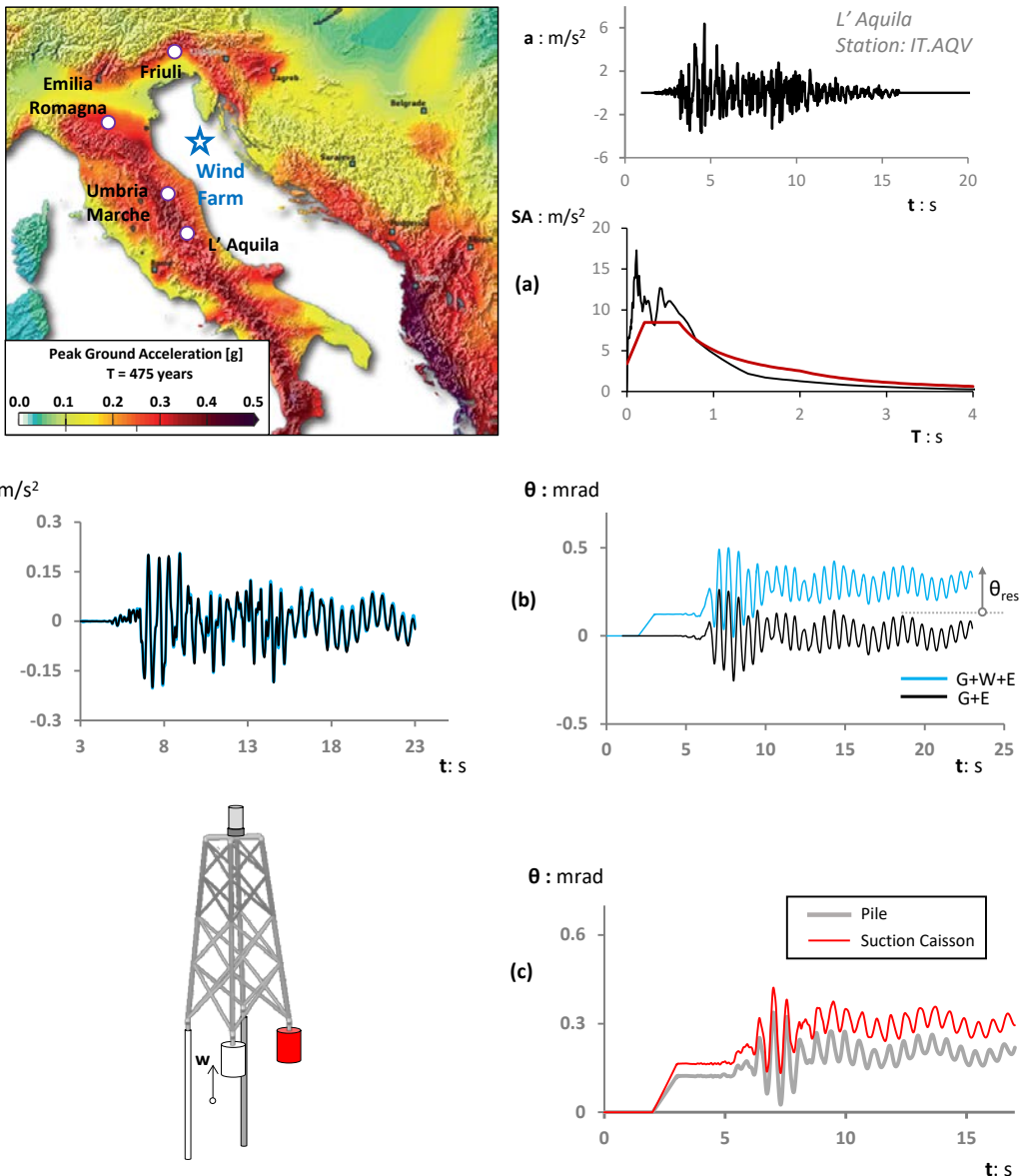


Figure 32 - Seismic Performance of OWT supported on Jackets : (a) Regional Seismicity in the area of the Wind farm; the L'Aquila input motion and its elastic response spectrum; (b) seismic response of a wind-turbine in operation (loading combination LC: G+W+E) and a wind turbine at rest (LC: G+E); time-history of seismic jacket rotation when the foundation is implemented with piles or suction caissons (LC: G+W+E)

Task 3.4 DEVELOPMENT OF DESIGN CHARTS

In the final Task of WP3 foundation design charts were proposed that: (i) facilitate quick dimensioning of foundation elements (i.e. Diameter and Embedment Length L) in order to achieve specific levels of safety (for a range of soil sites and sea depths) and (ii) correlate amplitude at Jacket supports to maximum foundation deformations (displacement and rotations) for a range of plausible foundation dimensions. The scenarios involved windfarms in the North Sea or the Mediterranean Sea, considering turbines of 8MW and 10MW. For the cohesionless North Sea sites, design charts for piled were provided foundation, while for the North mediterranean sites (where the seabed consists mainly of clayey soils), design charts for suction caissons were delivered.

Design charts for sand and clay sites are provided.

In sandy sites, charts are in the form of $\text{Deformation} = f[\text{Environmental load}]$, allowing for the user to decide upon the pile's dimensions, depending on the amplitude of environmental loading and the system's deformation requirements (Figure 33).

In clays (Figure 34) : Normalized $\text{Deformation} = f[\text{Factor of Safety}]$

Design charts, the methodology behind them and specifically developed design examples are available through the database www.jabaco.it.

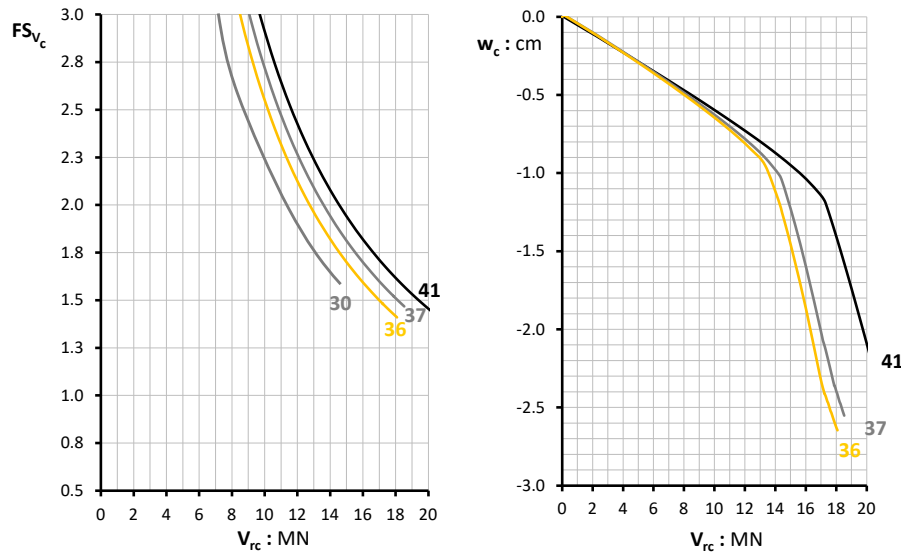


Figure 33 - Example design charts. Reference case: 10 MW turbine, pile foundation ($D=2.5\text{m}$), sandy site with $\phi=30^\circ$

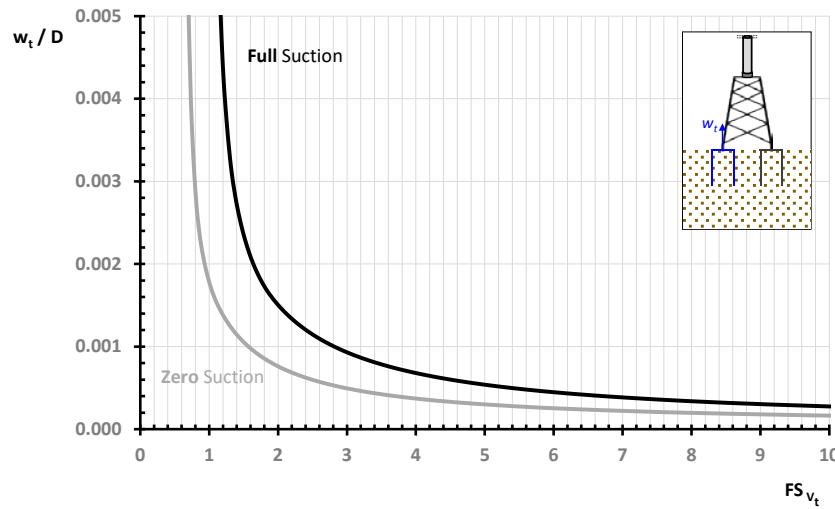


Figure 34 - Dimensionless design charts for suction caissons in clays: Dimensionless vertical deformation with respect to the vertical factor of safety at the leeward leg.

WP4 - MANUFACTURING OF STANDARD COMPONENTS FOR TESTING

OBJECTIVES AND MAIN OUTCOMES

This WP4 focuses on fabrication aspects. The aim is twofold:

1. Evaluate the Quality/Cost benefits of switching from traditional jacket fabrication techniques to increasingly automatized ones.
2. Fabricate prototypes for evaluate the final product quality level when switching from traditional production to prefabrication.

In the following a description of the activities for each task of WP4 is reported.

TASK 4.1 DESIGN OF STANDARD COMPONENTS FOR TESTING

Three different mock-up X-joints have been designed to be tested in the three different laboratories and comparing different fatigue testing methods, i.e the traditional hydraulic controlled testing method and the resonance testing method.

Resonance testing has the advantages to be quicker and the machine is quite lighter with respect to a traditional hydraulic one so it is possible to test larger joints in a reduced time window.

With the hydraulic testing rigs involved in the project both constant amplitude qualification of joints and compare with variable amplitude one considering the actual in service load scenarios

The stiffness of the joints and the dimensions has been selected to be as close as possible the one of the reference X-joint geometry (711x21; 711x35; mm) found to be the most recurrent one in the 6 windfarm scenarios analysed (Task 1.3).

Table 14 - Geometrical properties and Ephthymiou coefficients for the X-joints under consideration.

Joints		yield stress [MPa]	OD [mm]	wt [mm]	OD/wt	A [mm ²]	J [mm ⁴]	β	γ	τ	Θ
Reference X-joint	chord	350	711	35	20	7.4E+04	4.26E+09	1.00	10.16	0.60	90 deg
	brace		711	21	34	4.6E+04	2.71E+09				
X-joint for resonance testing	chord	350	806	35	23	8.5E+04	6.31E+09	0.88	11.51	0.60	90 deg
	brace		711	21	34	4.6E+04	2.71E+09				
X-joint for hydraulic testing	chord	350	210	10	21	6.28E+03	3.15E+07	1.00	10.50	0.60	90 deg
	brace		210	6	35	3.85E+03	2.00E+07				

$$\beta = \frac{d}{D} \quad \gamma = \frac{D}{2T} \quad \tau = \frac{t}{T} \quad \text{where:}$$

D chord external diameter

d brace external diameter

T chord wall thickness

t brace wall thickness

As can be seen in the table above the samples have been scaled to keep almost constant the coefficients relevant for the calculation of fatigue hot spot stresses and Stress Concentration Factors.

For the specimen to be tested in resonance machine a slight increase of the chord OD dimension has been recommended and adopted to make the response of the specimen more symmetric between out-of-plane bending mode and in the in-plane bending mode and make the machine work properly.

Finite element computations were performed to evaluate the stresses around the weld. The applied FE models are described in Task 6.1. A preliminary evaluation of Stress Concentration Factors have been performed comparing with the analytical formulation available in the design guidances (DNVGL-RP-C203 [7], CIDECT No. 8 [5]).

Detailed drawings of joints are provided in the relevant Deliverable 4.1.

TASK 4.2 BASE MATERIAL PROCUREMENT

Material selected for the particular application is the steel grade most widely used in offshore construction, i.e. S355J2 grade.

The base materials and consumables have been procured with the nominal grade of S355J2 as state-of-the-art material widely used in offshore constructions. Table 15 shows the mechanical properties of grade S355J2. The S355J2 tubes for the final manufacture of the prototypes were first subjected to cutting and bevelling procedures and then the Welding Procedure Specifications were applied in order to manufacture the final specimens.

Table 15 – Base material mechanical properties.

Steel grade	Minimum yield strength Reh MPa						Tensile strength Rm MPa		Minimum elongation - A Lo = 5,65 * So (%)				Notch impact test		
	Nominal thickness mm						Nominal thickness mm		Nominal thickness mm				Temperature °C	Min. absorbed energy J	
	≤16 ≤40	>16 ≤63	>40 ≤80	>63 ≤100	>80 ≤125	>100	>3 ≤100	>100 ≤125	>3 ≤40	>40 ≤63	>63 ≤100	>100 ≤125			
S355J2	355	345	335	325	315	295	470-630	450-600	22	21	20	18	-20	27	

Two different types of consumable material have been used:

- Semi-automatic process → CARBOFIL 1 1.2x0016xBS300
- Fully automated process (robot) → CARBOFIL 1 ELITE 1.20x0300xDRUM.

The material quality controls are provided in Deliverable 4.4.

Pipes relevant to provided specimens drawings have been fabricated by three roll bending operations.

Bending Operation - The plate is placed between the cylinders. It is centred using one of the heads. The cylinders are tightened to prevent the plate from coming loose. The head by which it was centred is initiated, with the aid of a template and acting independently on the bottom cylinders.

The other head is initiated in the same way and finally, without changing the cylinders position, the centre is bent.

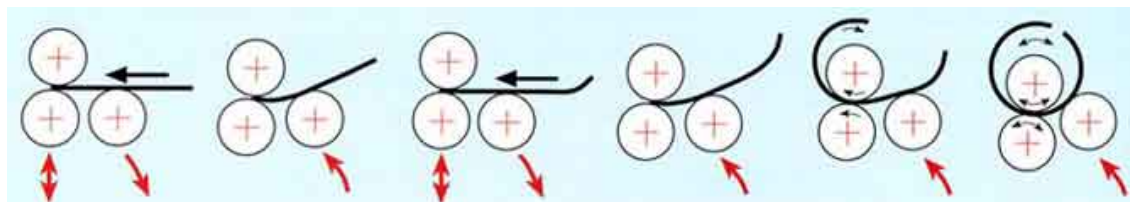


Figure 35 - Diagram showing how a plate is formed into a tube

Three roll benders work by pinching the metal between two rolls and curving it as it comes in contact with a back forming roll. This curves the metal workpiece into a cylindrical form, where it is welded together to produce a cylinder. The upper roll is in a fixed position, the lower roll has adjustable movement to perform the gripping function. These are the "pinch" rolls. The third roll (the forming roll) is also adjustable. With a manually opened or hydraulically moved drop hinge, the end of the top shaft is opened to allow removal of the finished work piece, especially a completed tube shape.

The one described is the main plate bending operation. There are other conical sections, which are done through the use of folding machines, and complex forming techniques.

TASK 4.3 WELDING PROCEDURE SPECIFICATION AND QUALIFICATION OF JOINTS

This Task 4.3 the following fabrication methods have been selected to be studied. Those are selected with increasingly upgraded level of automation, in particular:

- a. Semi-automatic Arc welding (MAG welding)
- b. Fully Automated Arc Welding (MAG welding)
- c. Robotized Welding (both TIG+MAG and Laser+MAG)

Written Welding Procedure Specifications (WPS) have been developed and summarized in Table 16 below. The written WPS are reported in Deliverable 4.3.1.

Table 16 - Summary of Welding Procedure Specifications.

Level of automation	Welding process	Joint geometry	WPS nr.
Semiautomatic (state-of-the-art)	MAG	X-joint: chord 806x35mm; brace 711x21mm; steel grade S355J2	M1/G062/1
		X-joint: chord 210x10mm; brace 210x6mm; steel grade S355J2	M1/G062/2
Fully Automated (Prefabrication welding process)	MAG	X-joint: chord 806x35mm; brace 711x21mm; steel grade S355J2	MR1/G062/1
		X-joint: chord 210x10mm; brace 210x6mm ; steel grade S355J2	MR1/G062/2
Robotized	TIG+MAG	Girth welded joint (220x10mm) ; steel grade S355J2	CSM_7-17
	Laser+MAG	Girth welded joint (220x10mm); steel grade S355J2	CSM_1-17

In the following a brief description of the above welding techniques and pros and cons is provided.

SIMULATION OF WPS

The welding book corresponding to M1/G062 parts 1 and 2 was modelled by the finite element method (FEM). As can be seen in Figure 36, the WPS are introduced in the developed numerical models, considering all the essential variables of the welding process, the actual cord and joint geometries, as well as all the properties of the materials of the weld, variable as a function of temperature. An adaptive mesh of the welded joint was made, ensuring that the Jacobian error of the elements was zero. Adaptive hexahedral elements were used, using the birth and death of elements technique. In this way, the number of elements increases automatically during resolution, ensuring numerical convergence with an error of less than 2%.

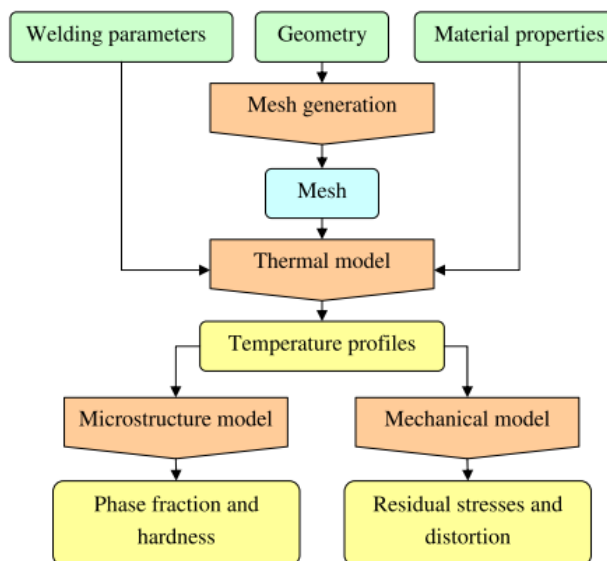


Figure 36 - FEM simulation process

A detailed analysis of the section of the joint was carried out with different possible configurations of both penetration and finishing with different geometries of welding beads. Three possible welding types have been modelled. They are shown in Figure 37:

- 1) Penetration Type 1, with a blunt root (aggressive geometric shape).

2) Penetration Type 2, with asymmetry in the inner root on the tube support wall to be penetrated.

3) Penetration Type 3, uniform with smoothed outline.

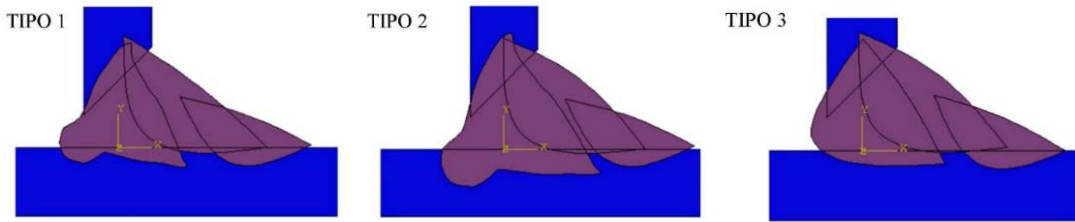


Figure 37 - Simulation of possible welding configurations

The microstructural phases predicted by the metallurgical numerical modelling are ferrite, bainite and perlite located at the surface. Only occurrence of martensite is anticipated for sudden cooling during the execution of the weld. Therefore, by controlling the essential variables during the welding process, no martensite should appear in the penetration zone or in the outer surface areas of the welded tubes.

In the case of the present study, the range of values of $t_{8/5}$ is between 0 and 132 seconds, which implies that we will have the whole range of mechanical properties and microstructural phases in the mockup of the welded node.

On the other hand, the geometry and dimension of the throat is critical for conditioning the triaxiality, and it is very influenced by the type of procedure (single or multi pass). Figure 38 shows the result of calculating the actual triaxial state associated with the welding process. The present study has calculated the triaxiality of the joint by using numerical simulation.

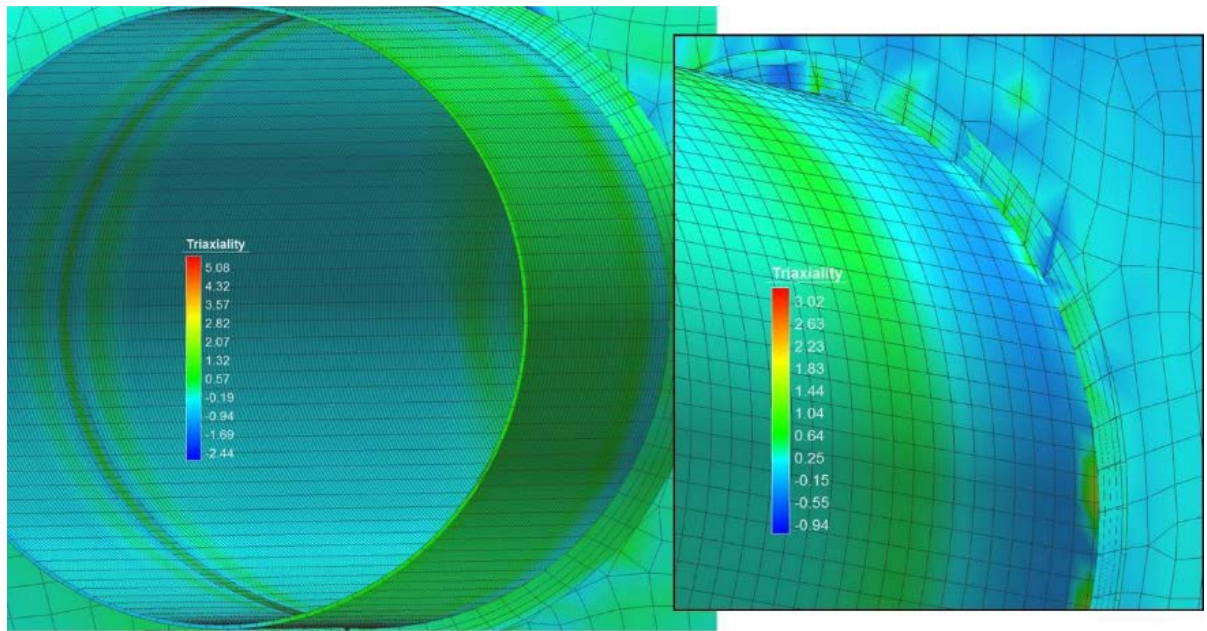


Figure 38 - Triaxial state associated to the welding process with penetration Type 3

The following conclusions can be extracted from the fatigue study of the original welded structure, which has been based on the welding book (Deliverale 4.3.1):

- 1) The welding of the joint with highly optimized throat geometries is recommended. In the area of penetration, a smooth penetration with blunt zones is required, similar to the Type 3 analyzed. In the upper part, the cords must have a very smooth transition to the tube walls, with blunted surfaces.
- 2) It is recommended to fix and control the thermal input applied in each pass of the welding process, in order to generate the metallurgy and the mechanical properties required.
- 3) The stress triaxiality is a critical parameter that is conditioned by the WPS and the definition of the joint. This parameter is a key to ensure in service life against static overloads and dynamic conditions. The multipass welding process has a great influence on the triaxiality as well as on the stresses that the different zones of the joint will be able to support, under different strain rates.
- 4) The welding process described in the welding book [1] is considered appropriate, applying the welding sequence attached in Figure 39.

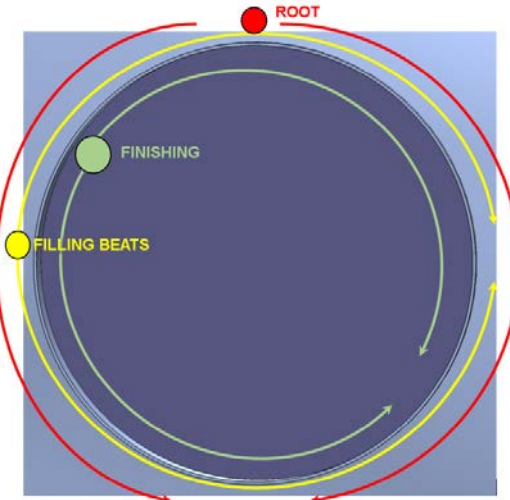


Figure 39 - Sequence of welds for making mockup starting at points

NONDESTRUCTIVE TESTS

Welded mock-ups have been characterized according to EN ISO 15614-1.

The ultrasonic (UT) and Magnetic-particle (MT) inspection have been performed on the joints showing absence of unacceptable defects according to EN ISO 5817 Quality Level B. These tests were done by Recoord, an external company.

Then Visual inspection (VT) has been performed on the joints showing absence of unacceptable defects according to EN ISO 5817 Quality Level C.

In summary, the different non-destructive tests are:

- Visual inspection: all specimens
- Magnetic-particle inspection: all specimens
- Ultrasonic: specimens 101 (devoted to resonant testing)

Detailed NDT results are reported in Deliverable 4.4.

TASK 4.4 FABRICATION IMPROVEMENTS

Nr. 37 welded mock-ups have been fabricated and characterized according to EN ISO 15614-1. In Table 17 the joint geometry, Welding Procedure Specification and number of manufactured mock-ups are detailed.

Table 17 – Jabaco project X-joint mock-ups.

Level of automation	Welding process	Joint geometry	WPS nr.	Nr of fabricated joints
Semiautomatic (state-of-the-art)	MAG	X-joint: chord 806x35mm; brace 711x21mm; steel grade S355J2	M1/G062/1	4
		X-joint: chord 210x10mm; brace 210x6mm; steel grade S355J2	M1/G062/2	13
Fully Automated (Prefabrication welding process)	MAG	X-joint: chord 806x35mm; brace 711x21mm; steel grade S355J2	MR1/G062/1	2
		X-joint: chord 210x10mm; brace 210x6mm ; steel grade S355J2	MR1/G062/2	10
Post weld treated HFMI Semiautomatic	MAG	X-joint: chord 806x35mm; brace 711x21mm; steel grade S355J2	M1/G062/1	2
		X-joint: chord 210x10mm; brace 210x6mm; steel grade S355J2	M1/G062/2	2
Robotized	TIG+MAG	Girth welded joint (220x10mm) ; steel grade S355J2	CSM_7-17	2
	Laser+MAG	Girth welded joint (220x10mm); steel grade S355J2	CSM_1-17	2

In Figure 40 some pictures of fabrication trials are reported.



Figure 40 – Robot Welding (TIG+MAG) of jacket X-joint.

The welding parameters recorded during welding trials are reported in Table 18 and Table 19 are reported for X-joints and Girth joints respectively.

Table 18 – X joints welding parameters.

	WPS	pass	Amperage [A]	Voltage [V]	Travel speed [mm/s]	Number of passes	Notes
MANUAL WELDING	M1-1	root	120	18	1.5÷2.4	1	*
		filling + capping	250	25÷26.5	6÷8	11	flat position (pipe rotating) with MAG (135) semiautomatic welding. "Classic" process, no STT
	M1-2	root	120	18	1.5÷2.4	1	*
		filling + capping	235	24	6÷8	4 (1 filling + 3 capping)	MAG (135) semiautomatic welding. "Classic" process, no STT
ROBOT WELDING	MR1-1	root	120	18	1.5÷2.4	1	*
		filling + capping	280	24	8	11	MAG (135) robotic welding
	MR1-2	root	120	18	1.5÷2.4	1	*
		filling + capping	250	24	8	4 (1 filling + 3 capping)	MAG (135) robotic welding

* Root pass performed in vertical (downhill progression) with GMAW (135) semiautomatic welding, using a specific process for root pass on pipe applications (Lincoln Electric STT: <http://www.lincolnelectric.com/resources/support/process-and-theory/Pages/stt-pipe-welding-detail.aspx>), to achieve a correct weld profile on the root in order to improve fatigue resistance.

Table 19 – Girth joint welding parameters.

	WPS	pass	Amperage [A]	Voltage [V]	Travel speed [mm/s]	Number of passes	Notes
ROBOT WELDING	CSM_7-17	root	220	13	2.5	1	TIG Welding
		filling + capping	290	27	8	3	MAG Welding
	CSM_1-17	root	320	27	20	1	Hybrid Welding (MAG+LASER)
		filling + capping	290	27	8	1	MAG Welding

HAMMER PEENING - HFMI

Figure 1 shows one jacket manufactured by IDESA. This jacket was semi-automatically welded, according to the IDESA's Welding Book (WPS M1/G062/1 y 2) [1].



Figure 41 - (left) Different regions for the preparation of specimens (right) Application of HFMI on laboratory specimens

As it is marked in Figure 20, two different type of regions were selected for analysis and images of the application of the HFMI on the specimens employed to measure the residual stresses.

Regarding optimization and validation of HFMI treatment as post-welding treatment of the IDESA's jackets, the following strategy was set:

- a. Optimization and operator training by using Region 1 and Region 2 specimens.
- b. Execution of optimum treatment on Region 1 and Region 2 specimens.
- c. Residual stress measurements before and after optimum treatment on Region 1 and Region 2 specimens. (Task 5.1)
- d. Determination of stress raiser on Region 2 specimens (most aggressive condition) before and after optimum treatment. (Task 5.1)
- e. Fatigue testing on slides obtained from Region 2 specimens (most aggressive stress raiser) before and after optimum treatment. (Task 5.1)

Finally, optimum treatment was applied at IDESA workshop.



Figure 42 - (a) Operator performing the HFMI treatment (b) specimens treated at IDEFAB

WP5 – EXPERIMENTAL INVESTIGATION ON SELECTED SCALED COMPONENTS

OBJECTIVES

The objective of this WP is to experimentally validate the structural behaviour of the prefabricated components.

The testing program comprises material testing for the characterization of base material and weld properties as well as large scale tests on whole component.

Since offshore structures are mainly subjected to cyclic loading most part of the experimental activities have been dedicated to fatigue strength evaluation.

Experimental data from this WP will be useful for:

- Fine tuning of finite element models developed in WP6;
- Evaluate actual fatigue behaviour of prefabricated components and potential fatigue life enhancement.

TASK 5.1 MATERIAL CHARACTERIZATION AND RESIDUAL STRESS MEASUREMENTS

In this task the fabricated joints have been sectioned and deeply analysed to characterize the quality of joints. In particular the following experimental activities have been performed:

Tensile tests and Charpy V notch impact tests to characterize the base material.

X joints fabricated with the different processes have been sectioned and the following characterization performed:

- Hardness measurements
- Residual stress measurements
- Small scale fatigue tests on HFMI treated joints
- Metallographic analysis

BASE MATERIAL CHARACTERIZATION

Base material used for this project is S355J2. This steel grade is the most commonly used one for offshore constructions since the focus of the project was on innovative fabrication with higher productivity techniques and processes. Tensile specimens have been extracted from both brace (BT specimens) and chord (CT specimens) elements along tubular axis direction. The specimens were proportional cylindrical ones according to ISO 6892 standard. Tensile properties and stress-strain curves are reported in the followings.

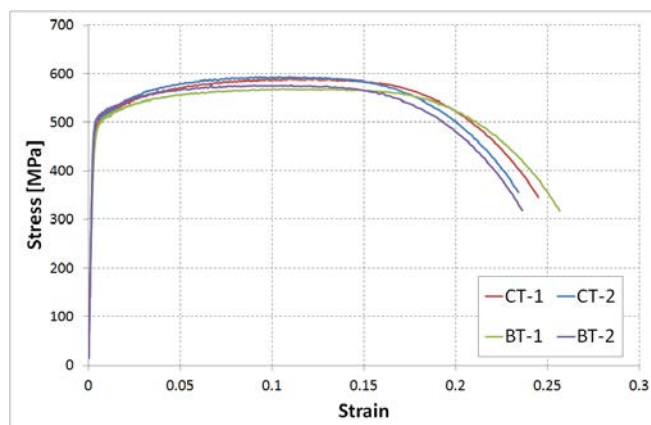


Figure 43 - Engineering stress-strain curves.

Impact tests at 3 different low temperatures have been performed on Charpy V notched specimens extracted from both brace and chord tubular in longitudinal direction with notch through thickness. Relevant results are reported in the following table:

Table 20 - Charpy V notch tests

Brace								
T [°C]	0			-20			-40	
KV ₂ [J]	184	180	174	156	160	168	144	142
avg KV ₂ [J]		179			161			152
Chord								
T [°C]	0			-20			-40	
KV ₂ [J]	160	128	164	154	144	76	136	100
avg KV ₂ [J]		151			125			112
								116

RESIDUAL STRESSES

Residual stresses can affect the fatigue performances of a welded joint especially if tensile residual stresses are of concern: crack propagation at weld defects is promoted by the presence of tensile residual stresses that locally adds on the structural load acting on the structure, resulting in higher stress level than expected.

In this experimental evaluations X-joints in three (3) different delivery conditions are compared:

- Semi automatic welded X-joint, as welded condition
- Semi automatic welded X-joint, HFMI (hammer peening post weld treatment)
- Fully-automatic welded X-joints, as welded condition

Residual stresses have been measured applying two (2) different techniques: X-ray diffraction and Hole Drilling techniques as reported in the following sections.

Table 21 summarizes the increase on compressive residual stresses after HFMI post welding treatment. As it can be shown, compressive stress from 62 MPa to 570 MPa was introduced. The great scatter can be due to the variability in the HAZ mechanical properties along the joint, but also to the manual operating technique. Small deviations on the point of measurement, between the original and HFMI situations, could also explain this scatter.

Table 21 - Compressive stresses and local work hardening (FWHM) induced by HFMI on the HAZ

Specimen	Point	Δσ _{max} [MPa]	Δσ _{min} [MPa]	ΔFWHM [°]
Region 1	3	-570	-62	0.42
	4	-103	-336	0.79
	5	-251	-181	0.68
Region 2 Zone 1	2A	1	-246	0.63
	2B	-488	-414	0.30
	2C	-166	-379	0.87
Region 2 Zone 2	2A	-554	-331	0.18
	2B	-246	-187	0.90
	2C	-130	-229	0.21

In Figure 44 residual stress measurements performed with different techniques are compared. Values obtained with X-ray diffraction and Hole drilling on the semi-automatic joints (SA) are consistent varying between + 200 MPa and – 400 MPa (actual base material yield strength is almost 500 MPa).

Values obtained for the fully-automatic joints (FA) shows a tendency to higher residual stresses close to the welded joint (HAZ), particularly when compressive residual stresses are considered.

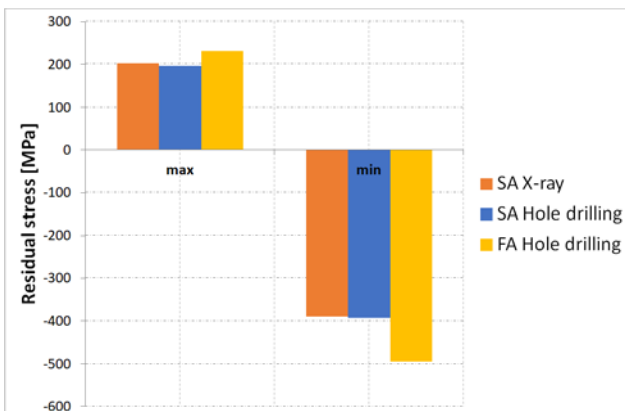


Figure 44 - Hole drilling (h-d) and X-ray diffraction (x-r) measurements comparison.

HARDNESS MEASUREMENTS

Hardness measurements have been performed according to ISO 9015-1 (HV10). In Figure 45 the results are reported for semi-automatic and fully-automatic weld process respectively.

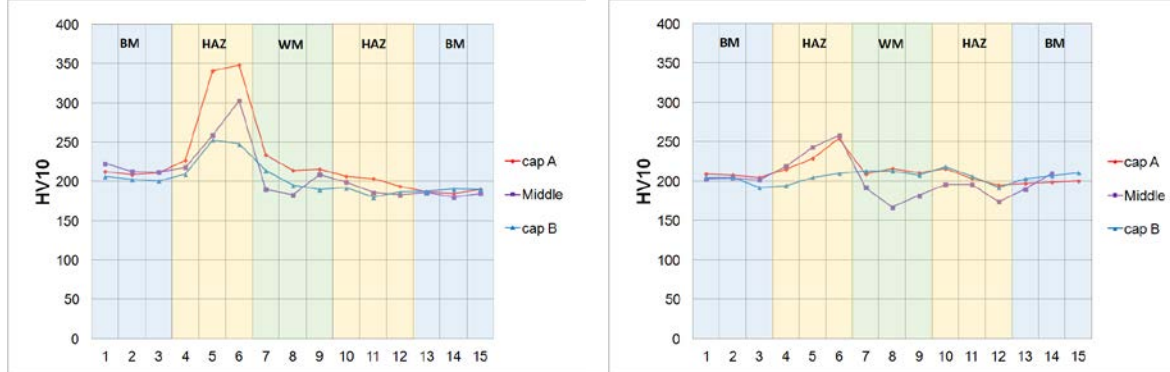


Figure 45 - Hardness measurements on (left) semi-automatic traditional weld and (right) fully-automatic weld.

STRESS RAISERS

Geometrical inspections of received X-joints have been performed comparing the semi-automatic welded joints (SA) than for the fully-automatic ones (FA). Summary of data are reported in the followings. In Appendix A the complete measurements are available.

In Figure 46 the weld metal height profiles at the saddle and crown locations are reported. Fatigue crack initiation is at the weld toe on the chord side (axis origin in Figure 46 left). As can be seen the weld bead angle with respect to the chord is generally higher for the SA weld than for the FA weld. At the crown location (Figure 46 right) crack initiated is in the weld metal, in the convex area. This kind of shape is common to both SA and FA welding processes.

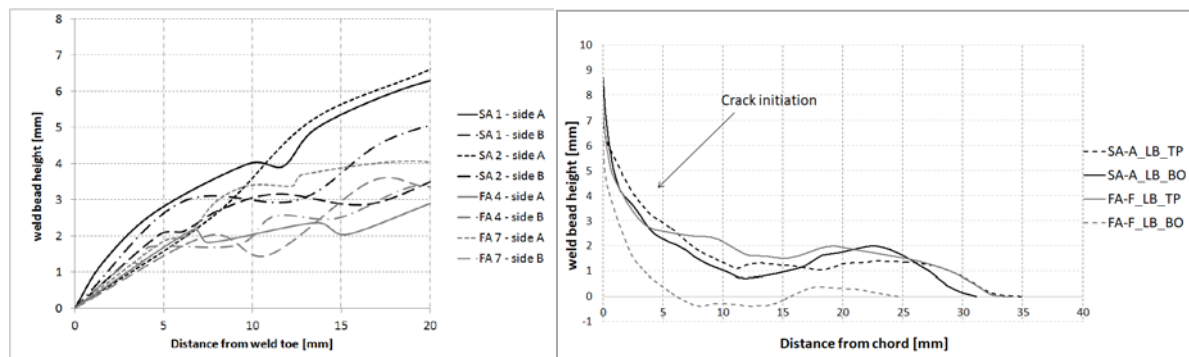


Figure 46 - Weld bead profiles at saddle (left) and crown (right) location.

Stress raiser of pos weld HFMI treated joints was measured by using ARAMIS Technology. ARAMIS is a non-contact and material-independent measuring system based on digital image correlation (DIC). Figure 47 shows an example of the maps of strain obtained by the ARAMIS technology for a load level close to the 80% of the yield strength of the S355J2, in the as welded condition. Table 3 shows the numerical values obtained for each specimen, as well as the mean value \pm standard deviation.

Table 22 - Results obtained after the measurements of stress raisers

Specimen	As welded		HFMI PWHT	
	Internal	External	Internal	External
1	1.45	1.85	1.45	1.25
2	1.48	2.05	1.48	1.35
Mean \pm dev	1.47 ± 0.02	1.95 ± 0.14	1.47 ± 0.02	1.30 ± 0.07

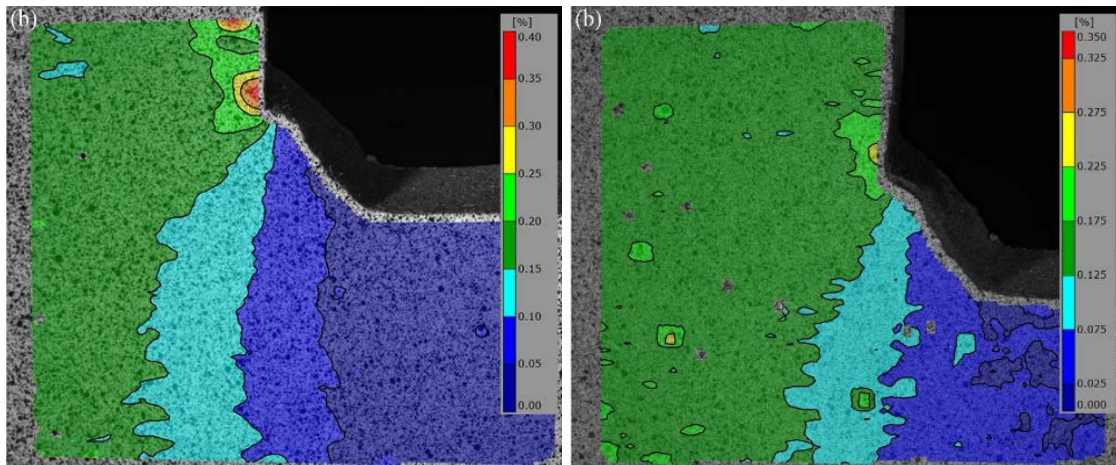


Figure 47 - Strain map for the external stress raiser: (a) as welded condition (b) after HFMI treatment

SMALL SCALE FATIGUE TESTS ON HFMI TREATED JOINTS

Fatigue tests were performed on T specimens extracted from full scale joint. A MTS universal dynamic testing machine, with a load cell of 250 kN, was employed to perform the fatigue tests. Maximum stress of 80 % of the yield strength of the S355J2 was employed, with a fatigue ratio $R=0.1$. A frequency of 10 Hz was used.

Three specimens without treatment and four specimens with HFMI were tested. After the fracture of the specimens, an analysis of the fracture surface was made by using a scanning electron microscope (SEM), equipped with EDX micro chemical analysis. It was also reported if fracture took place on the internal or the external stress raiser.

Fatigue tests were performed with the following nominal load parameters: $\sigma_{\max} = 284$ MPa; $\sigma_{\min} = 28$ MPa. Table 4 shows the results obtained, before and after the HFMI treatment.

Table 23 - Results obtained in the fatigue tests

Condition	Specimen	Fatigue life [Cycles]
As welded	1	86.890
	2	56.434
	3	79.540
	Mean \pm dev	74.540 ± 15.893
HFMI	1	116.742
	2	170.648
	3	363.454
	4	258.728
	Mean \pm dev	227.393 ± 107.948

That means that fatigue life was increase by a factor of 3.05, regarding average values. Nevertheless, it should be pointed out the great scatter obtained in the HFMI condition. However, taking the most conservative values (86.890 cycles in the as welded condition and 116.742 cycles in the HFMI condition), an improvement by a factor of 1.34 was obtained. That means that HFMI would be able to increase the fatigue life of the component at least a 34 %.

The as welded specimens fracture took place on the external stress raiser. Figure 48 shows the HFMI specimens. In the case of specimen 2, fracture took place on the internal stress raiser.

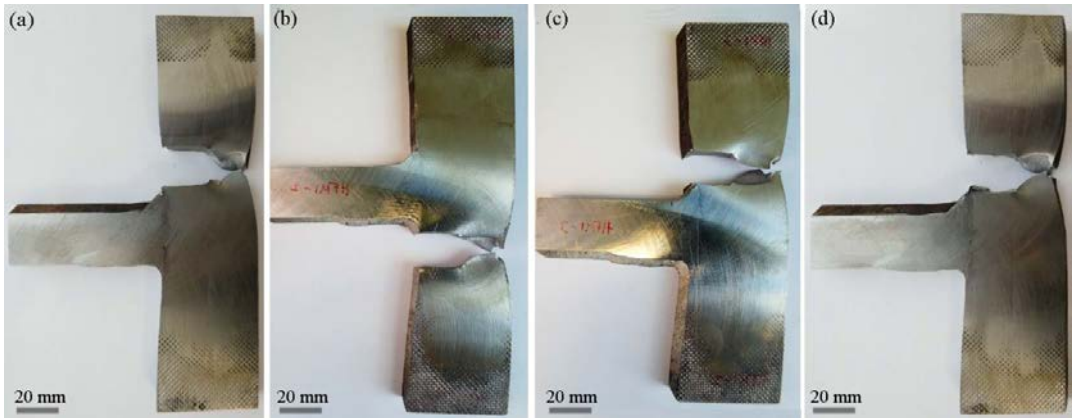


Figure 48 - Fatigue specimens after testing (HFMI condition)

TASK 5.2 AND 5.3 FULL-SCALE TESTING

A total number of 24 joints have been tested in full scale (Table 24). The testing program aimed at comparing fatigue performances of traditional semi automatic (SA) and improved fully automatic (FA) processes. In addition, a limited number of joints have been tested after HFMI post weld treatment (i.e. 2 X-joints). Since the testing program has been rearranged to accommodate a larger number of fatigue tests the monotonic ones have been performed only with the aim of evaluate residual stiffness after fatigue crack detection.

Base materials and consumables have been procured with the nominal grade of S355J2 as state-of-the-art material widely used in offshore constructions (Deliverable 5.1 for material characterization. Welding Procedure Specifications are reported in Deliverable 4.3.1)

Table 24 - Actual full-scale testing program (Task 5.2 and 5.3)

Fabrication process	In-Plane Bending fatigue	Out-of-Plane Bending fatigue		Resonant fatigue
	Constant amplitude fatigue	Constant amplitude fatigue	Variable amplitude fatigue	Constant amplitude fatigue
Semi automatic (SA)	4	4	2	2
Fully automatic (FA)	4	4	-	2
Post weld treated HFMI	2	-	-	-

Different experimental testing campaign are reported:

- Traditional hydraulic testing Out-of-plane bending (OPB)
- Traditional hydraulic testing In-plane bending (IPB)
- Resonant testing (mixed OPB and IPB)

With respect to resonant testing method the main advantage is the simple and straightforward association of loading conditions to stress location. On the other side the traditional testing method does not allow for very high frequencies and requires longer time to complete the test. Moreover, the hydraulic jack and testing rig shall be very large to conduct a 1:1 scale test and normally a reduced scale need to be applied.

With the hydraulic testing rigs involved in the project both constant amplitude and variable amplitude tests have been performed.

Strain gauges measurements have been performed with the aim of evaluate the actual Hot Spot Stress. Moreover, residual strength and stiffness after fatigue crack detection have been evaluated by meand of monotonic loading and displacement measurements.

For the aim of this project the joints have been scaled according to geometrical parameters relevant to fatigue behaviour (Table 25). Details of specimen's design are reported in Deliverable 4.1.

Table 25 - Geometrical properties of the X-joints under consideration.

Joints		Yield stress [MPa]	OD [mm]	wt [mm]
Reference X- joint	chord	350	711	35
	brace		711	21
X-joint for resonance testing	chord	350	806	35
	brace		711	21
X-joint for hydraulic testing	chord	350	210	10
	brace		210	6

REFERENCE S-N CURVES

The fatigue resistance of the material in or around a weld to variable stresses is given in the form of empirical S-N curves, where S is a constant amplitude stress range and N the number of cycles to failure. Many S-N curves have been determined and can be found in the literature. Each curve is strictly associated with a particular definition of S and N, as well as a particular structural detail; they shall not be used with variables that are defined in a different manner or for different structural details.

In the framework of this research effort the fatigue strength curves proposed by ISO 19902, DNV-RP-C203 and API-RP-2A have been considered for comparison (Figure 49).

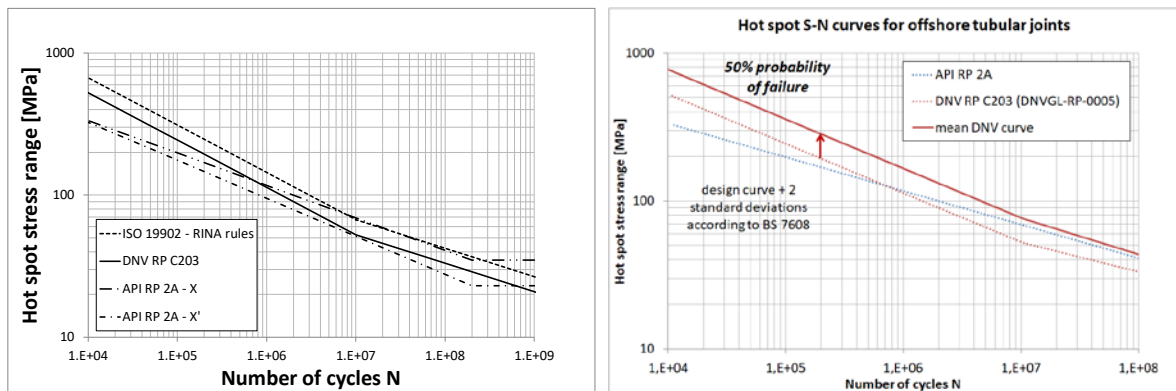


Figure 49 – Left: Comparison among different fatigue design S-N curves for offshore tubular connections. **Right:** Standard deviation applied to S-N curves.

The stress to be used for design purpose is the range of idealised hot spot stress defined by: the greatest value of the extrapolation of the maximum principal stress distribution immediately outside the region effected by the geometry of the weld. The hot spot stress to be used in combination with those design curves (Figure 49left) is calculated as

$$HSS = SCF \cdot \sigma_{nominal}$$

where SCF = stress concentration factor.

The SCF shall include all stress raising effects associated with the geometry and force pattern of the joint, except the local (microscopic) weld notch effect, which is included in the S-N curve.

SCFs may be derived from FEA, experimental tests or empirical equations (Efthymiou equations) based on such methods. In general, the SCFs depend on the type of variable forces exerted by the brace on the joint, the type of joint, and details of the joint geometry. Brace axial forces, brace in-plane bending (IPB) and brace out-of-plane bending (OPB) moments cause different patterns of variable stresses around the joint.

When comparing experimental data with Standards the safety factors applied to S-N design curves have to be neglected. Standard S-N curves represent a 97.5% probability of survival curve while fitted experimental data ideally represents a 50% probability of survival. Design S-N curves are obtained by subtracting two standard deviations from the 50% probability curve. For the purpose of this study the standard deviation from BS 7608 are applied. In Figure 49right the 50% probability of survival curves are reported.

OUT-OF-PLANE BENDING

Ten (10) joints have been tested in OPB loading conditions, in particular:

- 4 semi automatic MAG process constant stress range fatigue;
- 4 fully automatic MAG process constant stress range fatigue;
- 2 semi automatic MAG process variable stress range fatigue.

In Figure 50 a picture of the samples as delivered to the testing lab is reported. The machine is a servo-hydraulic controlled one with 100 tons load capacity (80 tons in variable amplitude). Maximum displacement $\pm 120\text{mm}$. Wave shape can be sinusoidal, triangular or variable.



Figure 50 - X-joint as delivered to laboratory.

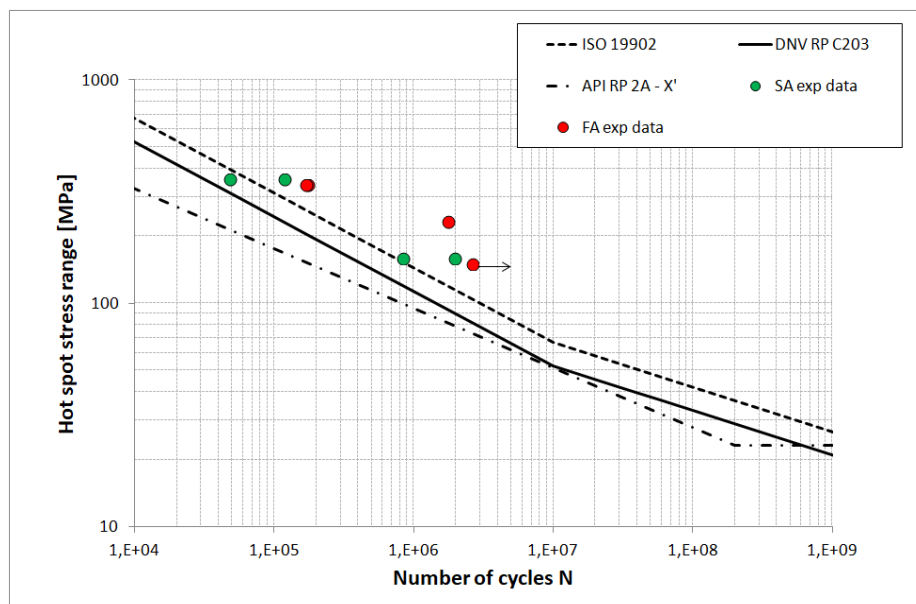


Figure 51 – Experimental results comparison with standard S-N curve.

Table 26 – Tabulated experimental results.

Test ID	Process	Max load [kN]	Min load [kN]	cycles	notes
1	SA	101	10	4.70×10^4	Failed
6		101	10	1.16×10^5	Failed
2		50	5	8.19×10^5	Failed
3		50	5	1.94×10^6	Failed
4	FA	50	5	2.60×10^6	Run-out
5		76	8	1.73×10^6	Failed
7		101	10	1.73×10^5	Failed
8		101	10	1.66×10^5	Failed

Fatigue crack initiated at the weld toe from the chord side, in saddle position and propagated along the weld toe and through the chord thickness (Figure 52).

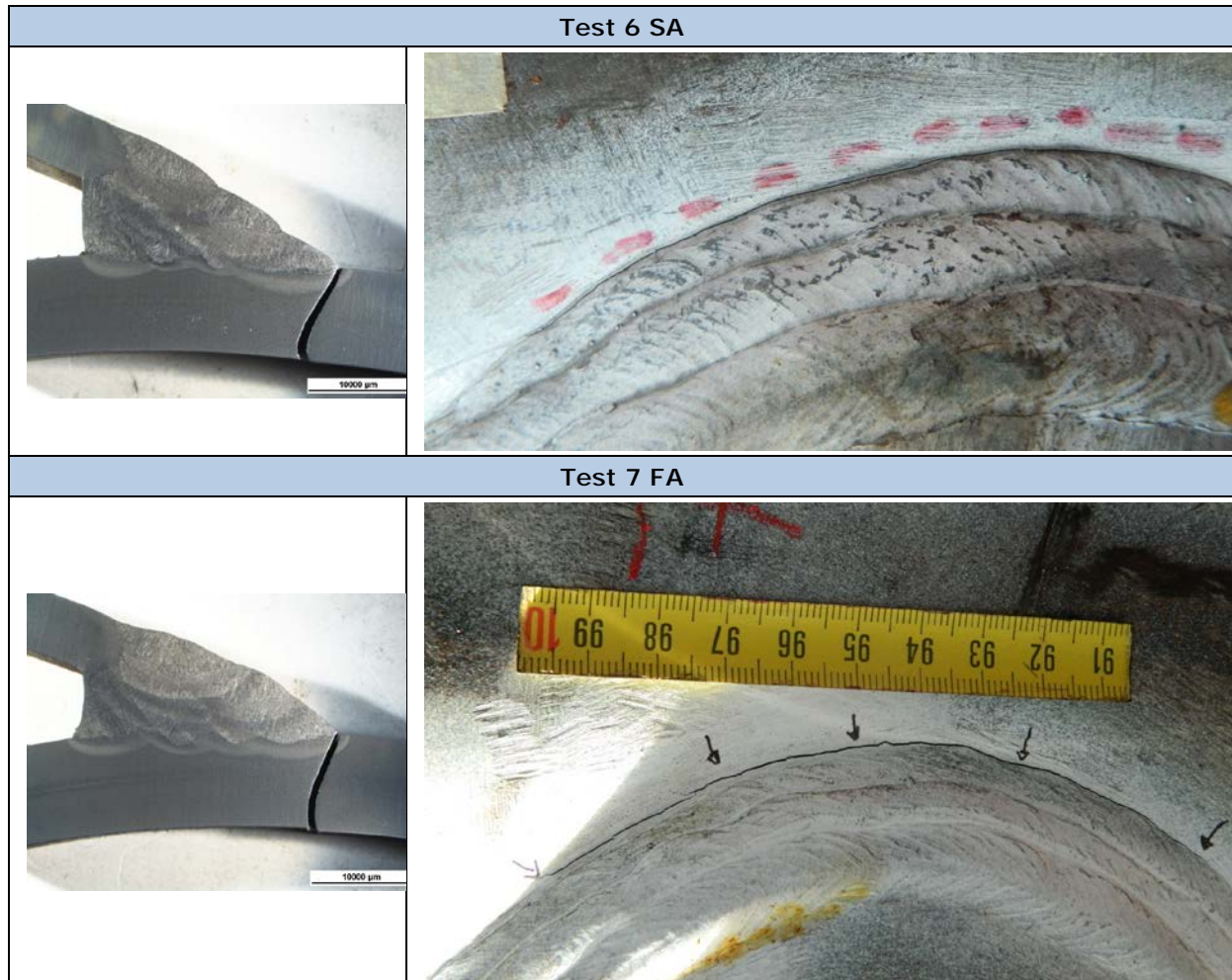


Figure 52 – Fatigue crack of test ID 6 and ID 7.

In limited cases (Test 5 and Test 10) the fatigue crack propagated through the heat affected zone (HAZ) and the base material (BM). In Deliverable 5.2-5.3 the pictures of fatigue crack are reported.

OUT-OF-PLANE BENDING VARIABLE AMPLITUDE FATIGUE

With the aim of evaluate effectiveness of linear damage fatigue accumulation rules two (2) full scale variable amplitude fatigue tests have been performed in the out-of-plane bending configuration.

The variable load has been applied by blocks of given magnitude, as reported in Table 27, at R=0.1 and 0.5Hz.

Table 27 – Variable amplitude loading blocks

Load block ID	Max Load [kN]	Min Load [kN]	HSS Range [MPa]
A	101	10	360
B	76	8	248
C	50	5	160

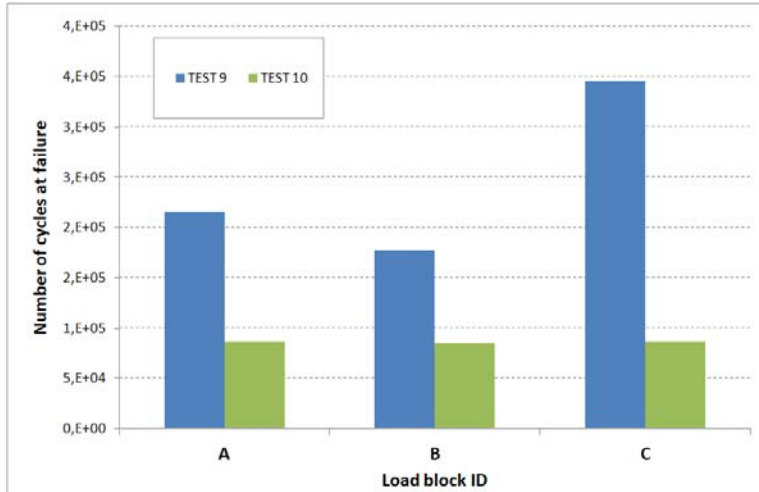


Figure 53 – Number of cycles at failure for each loading block.

Equivalent constant amplitude stress ranges have been evaluated by applying standard API X' fatigue curve for offshore joints and linear damage accumulation formula (Miner's rule):

$$D = \sum_i^n \frac{n_i}{N_{Ri}}$$

Where:

D is the damage during the design life

n_i is the number of cycles associated with the stress range $\Delta\sigma_i$ for the load block i

N_{Ri} is the endurance (in cycles) obtained from the S-N curve for a stress range $\Delta\sigma_i$

The experimental results expressed in terms of equivalent stress range on the basis of API X' curve and linear damage accumulation Miner criterion are reported in Figure 54.

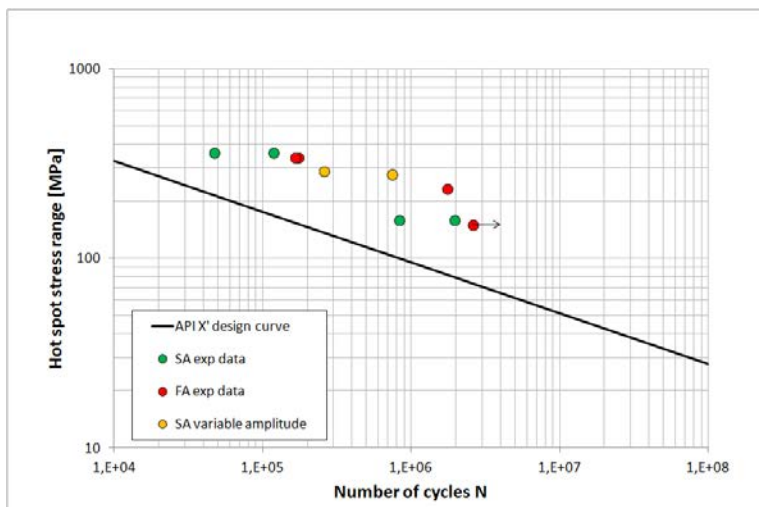


Figure 54 – Variable amplitude fatigue data: comparison with constant amplitude ones and API X' design curve.

OUT-OF-PLANE BENDING STRAIN GAUGES MEASUREMENTS

Due to relatively complex geometry of tubular joints the determination of simple nominal stress can be difficult consequently the design of such tubular joints is based on the determination of hot spot stress (HSS), Figure 55. The hot-spot stress (HSS) includes the macroscopic stress concentrating effects of the weld detail but not the local peak stress caused by the notch at the weld toe (i.e. weld toe radius, undercut, etc.).

The joints have been instrumented with strain gauges to get strain concentration due to global weld geometry (Figure 55).

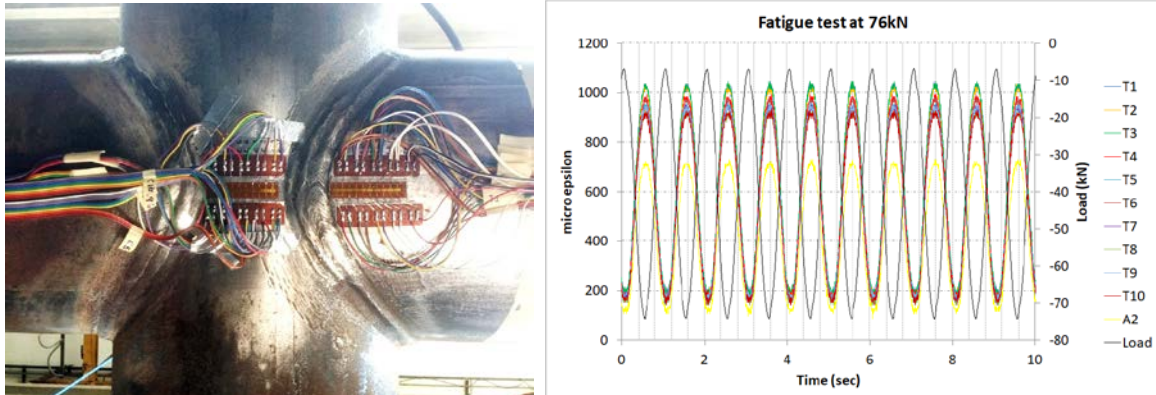


Figure 55 – Strain gauge instrumentation and measurements (10 cycles at 76kN maximum load on test ID 5 (FA)).

The complete set of measurements is reported in Deliverable 5.2-5.3.

HSS extrapolated (Table 28) at the weld toe from the chord side, where failure occurred.

Table 28 – SCFs evaluated by strain gauges measurements (chord saddle position).

Test ID	Nominal stress [MPa]	HSS [MPa]	SCF experimental	SCF analytical
5 (FA)	131	222	1.69	
5 (FA)	85	156	1.84	
10 (SA)	120	209	1.74	1.57
10 (SA)	69	133	1.93	

OUT-OF-PLANE BENDING MONOTONIC LOADING

A series of monotonic loading tests have been done with the aim of evaluate the evolution of the joint stiffness while experiencing fatigue loading and degradation.

In Figure 56 the load vs displacement curves before fatigue testing and after failure (crack length >10 cm) for Test 5 and Test 10 tested at 76 kN maximum load (37 kNm maximum bending moment applied) are reported. Despite the stiffness is sensitively reduced the global bending behaviour is still in the linear part and no plastic hinge formation is advised.

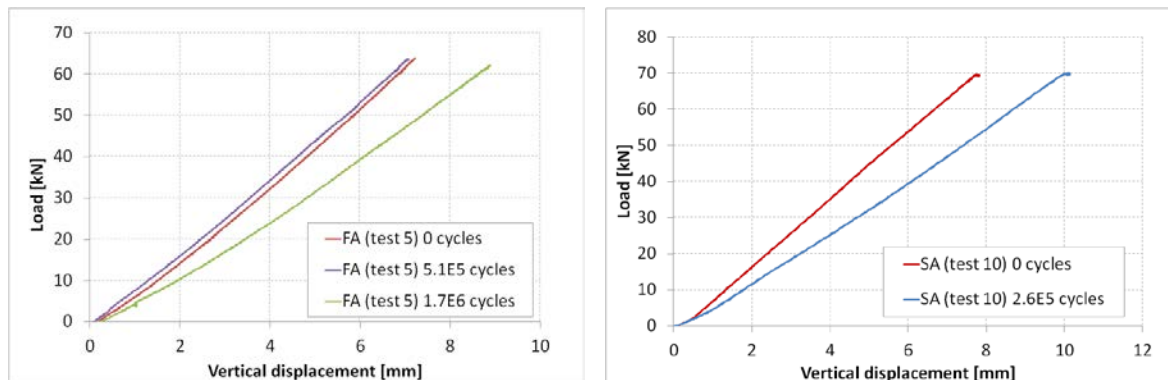


Figure 56 – Joint stiffness evolution during the test.

IN-PLANE BENDING FATIGUE TESTING

The experimental investigation consists of ten (10) cyclic tests on X-joint tubular welded specimens under high-cycle fatigue. Three different branch-to-chord weld processes were examined: manual (semi-automatic, denoted as SA), robot (fully-automatic, denoted as FA) and hammer peening (denoted as HP). The branch pipe had a nominal cross-section 219.3×6 mm and the chord (main pipe) 219.1×10 mm. The pipes were made of S355J2 steel with a nominal yield stress of 355 MPa.

The experimental set-up configuration is presented in Figure 57. The load was applied to the chord in the chord-branch plane (in-plane bending) through a 250-kN-force-capacity hydraulic actuator. The chord of the specimen was bolted to the actuator while both ends of the branch were

supported to appropriate hinges. Internal air pressure of about 1.0 bar was used to detect at which cycle the through-thickness crack occurred.

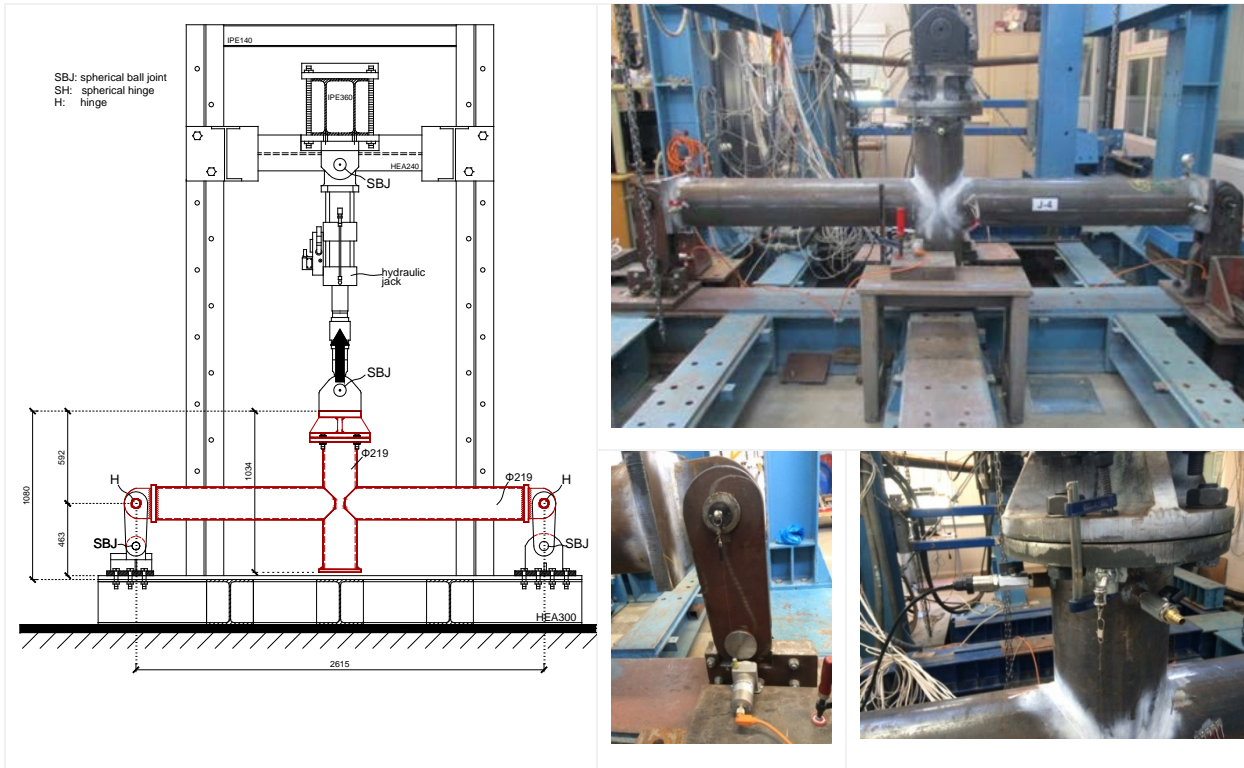


Figure 57 – Experimental set-up for in-plane bending fatigue tests.

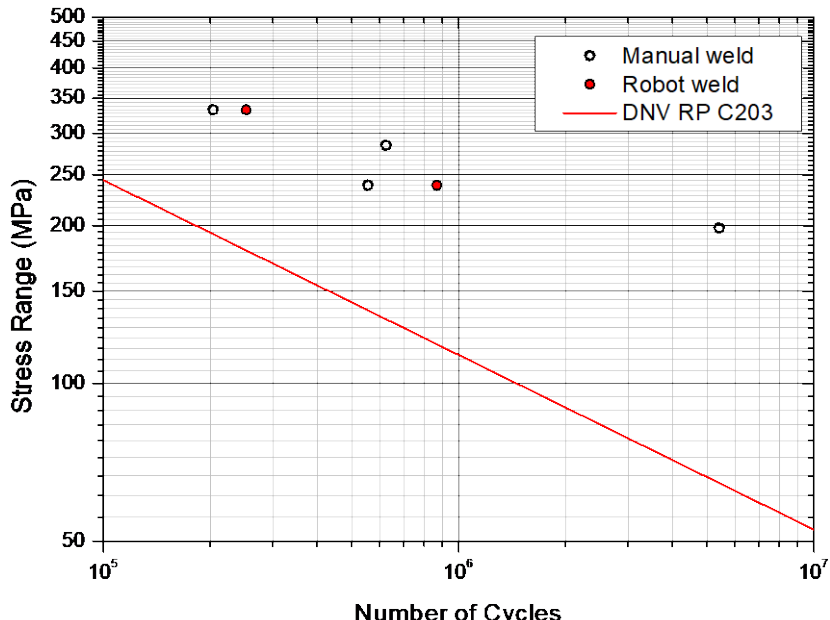


Figure 58 – Experimental results; comparison with DNV RP C203 standard S-N curve.

Test results are summarized in Table 29. All the specimens were subjected to high-cycle fatigue loading at a frequency $0.7 \div 1.5\text{Hz}$ with a load ratio of P_{\min}/P_{\max} equal to 0.15. In all cases, the through-thickness crack occurred at the chord side of the welded connection. Cracking initiated at the crown location or/and between the crown and the saddle of the joint. Finally, a major crack developed along the weld circumference which opened progressively through the thickness of the chord (Figure 52). In Deliverable 5.2-5.3, pictures of fatigue crack (through-thickness) for all specimens are reported.

Table 29 – In-Plane bending experimental results.

specimen	process	max load, P_{\max} (kN)	min load, P_{\min} (kN)	n_{\exp} (cycles)	notes
J-2	SA	48.3	7.1	5.55E+05	failure
J-3		67.4	10.1	2.04E+05	failure
J-4		40.1	6	2.42E+06	failure
J-8		57.6	8.6	6.24E+05	failure
J-5	FA	67.4	10.1	2.52E+05	failure
J-6		48.3	7.1	8.68E+05	failure
J-9		57.6	8.6	6.61E+05	failure
J-11		40.1	6	9.71E+05	failure
J-7	HP	67.4	10.1	1.00E+06	run-out
J-10		83.5	12.5	2.15E+05	failure

SA = semi-automatic (manual)

FA = fully-automatic (robot)

HP = hammer peening (post weld treated)

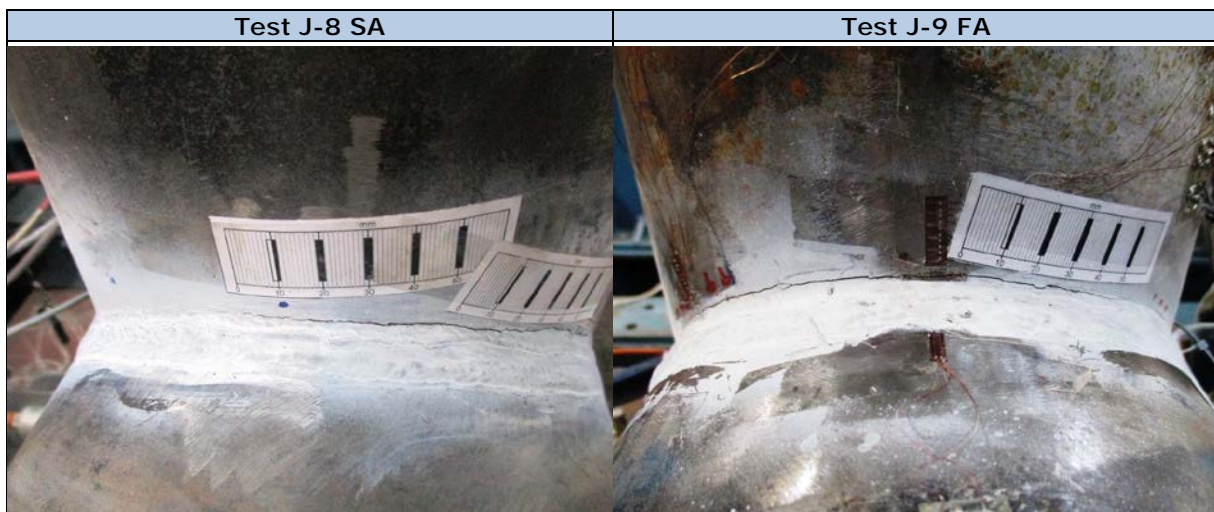


Figure 59 – Through-thickness crack at specimens J-8 and J-9.

STRAIN GAUGES MEASUREMENTS

Based on numerical analysis, a number of strain gauges placed at critical locations (Figure 52). Uniaxial and axial 5-element-strip strain gauges were attached to the specimens in the region of the weld toe at the chord side for determining the strain distribution in the X-joint connection. The distance between adjacent strain gages is equal to 3 mm, with the first one being placed 5 mm away from the weld toe of the connection. The measured strain values ranged from approximately 0.6 to 1.35% at the proximity of the chord weld toe. The complete set of strain measurements are reported in Deliverable 5.2-5.3.

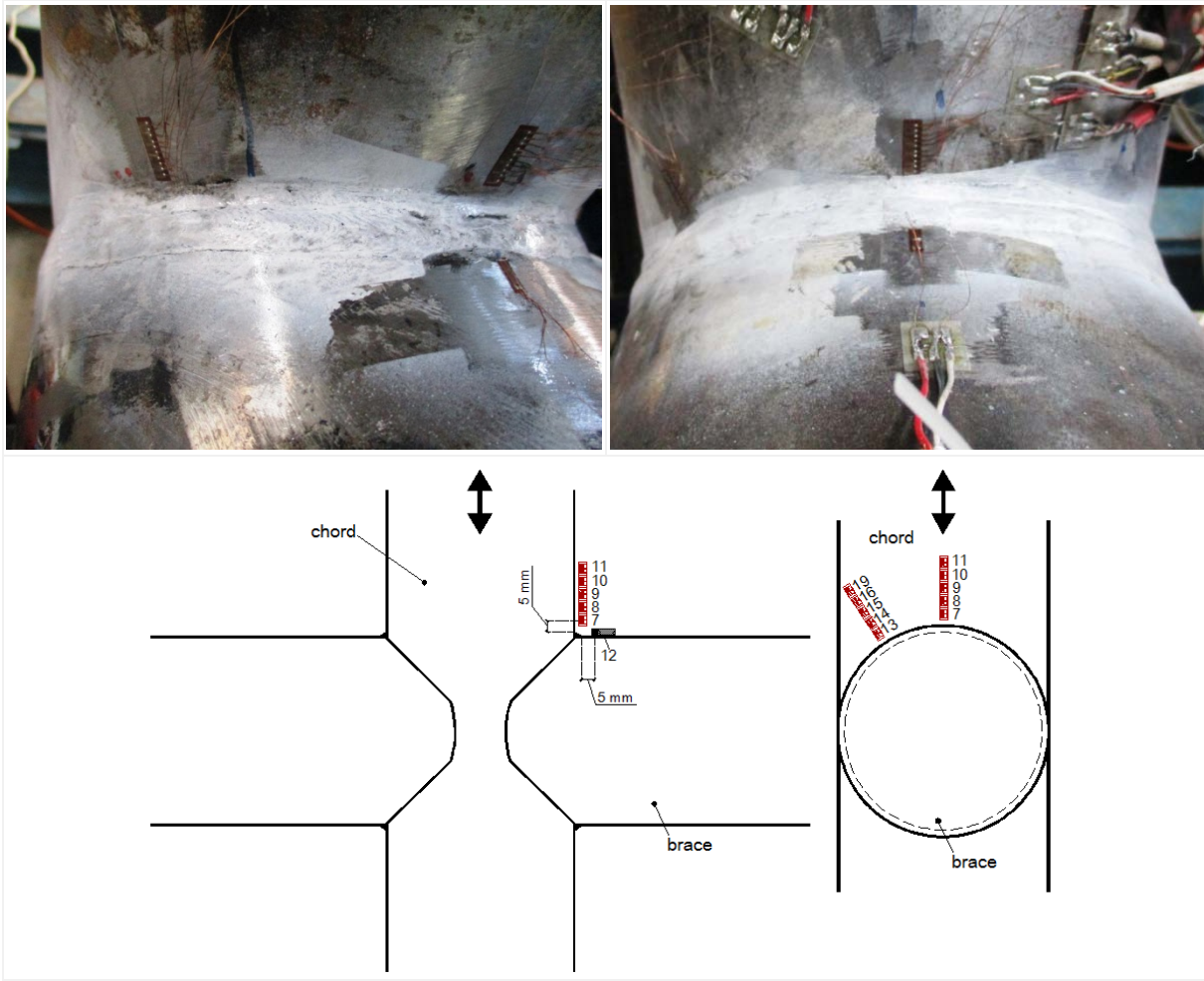


Figure 60 – Strain gauge instrumentation.

The experimental stress concentration factor (SCF experimental) and the hot-spot stress (HSS) were determined by using extrapolation method according to Appendix C of CIDECT no. 8.

Table 30 – SCFs evaluated by strain gauges measurements (chord crown position).

Test ID	Nominal stress [MPa]	HSS [MPa]	SCF experimental	SCF analytical
J-7 (HP)	195.1	378.7	1.94 ^(a)	2.02 ^(b)
J-8 (SA)	166.7	291.1	1.75 ^(a)	
J-9 (FA)	166.7	260.8	1.56 ^(a)	
J-10 (HP)	241.7	357.8	1.48 ^(a)	
J-11 (FA)	116.1	172.8	1.49 ^(a)	

(a) CALCULATED BY USING CIDECT NO. 8 (APPENDIX C)
 (b) CALCULATED BY USING CIDECT NO. 8 AND EFTHYMIOU (1988) EQUATIONS

LOAD-DISPLACEMENT DIAGRAMS AT SPECIFIC NUMBER OF CYCLES

A number of static loading cycles have been performed during the tests to identify the evolution of joint stiffness due to fatigue loading and its degradation.

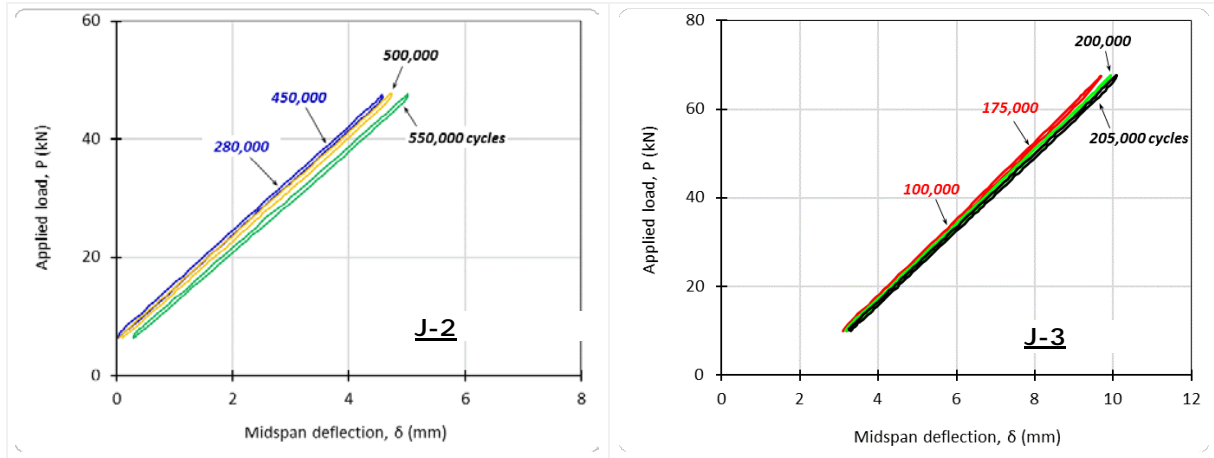


Figure 61 – Joint stiffness evolution during the test.

RESONANT FATIGUE TESTING

Four full scale specimens of tubular joints were tested in fatigue on a resonance test bench. The fatigue tests were performed at a frequency larger than 23Hz, more than twenty times faster than classical methods. The test method proved able to detect small crack by a change of resonance frequency of the specimen. The system is also foreseen to apply an elliptic loading on the specimen, in order to obtain hot spot stresses and strains as homogeneous as possible along the weld. In the tests, when a crack is detected, either by change in the response of strain gauge or by a change in the dynamic behaviour, an inspection by die-penetrant is carried out. The initial cracks are recorded. In the next stage of the test, the excitation is tuned such that the loading comes in only one plane, in order to obtain a simple crack propagation.



Figure 62 – Resonant fatigue testing rig.

Of the four specimens, two were produced by semi-automatic welding and two by a robot. Generally, their behaviour was similar. The lowest resonance resonance was obtained out-of-plane, while the in-plane resonance frequency was slightly higher, by typically 0.2Hz. During the initiation phase, the largest hot spot strain range was recorded at the brace saddle position. The second largest hot spot strain range was found at the chord crown. After the first inspection, the cracks were generally found close to the crown position, on the chord. It was then decided to continue the tests with in-plane loading for the crack propagation phase. Crack propagation proved to be significantly longer than crack initiation, close to three times longer. The breakthrough crack occurred three times through the brace and once through the chord.

Generally, there was no significant difference between the behaviour of the welds produced by a robot or a semi-automatic method. All of them fit on the same S-N curve, with a slope slightly larger than 3.

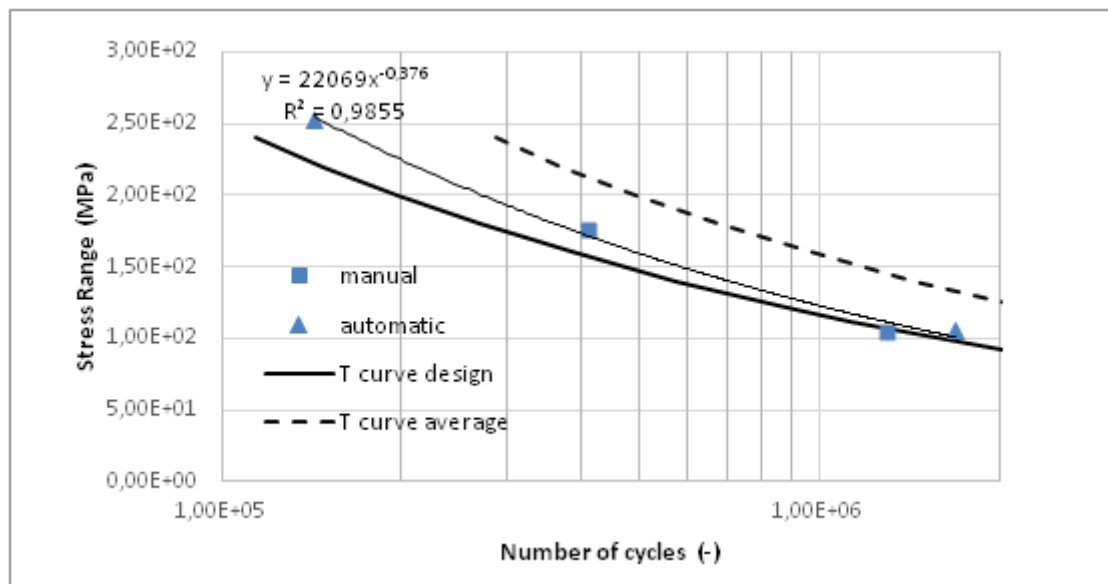


Figure 63 - Comparison between the S-N curve for tubular joints and the experimental results

It can sound as a contradiction that the cracks are initiated at the chord but propagate through the brace at a location with a lower hot spot stress. However, looking at the weld geometry, it is obvious that the most significant geometrical discontinuity is close to the chord, and not at the weld toe on the brace. The strain range measured by the strain gauges is too far from the geometrical discontinuity, and the crack initiation point. Consequently, the measured strain range on the brace is an underestimation of the actual one.

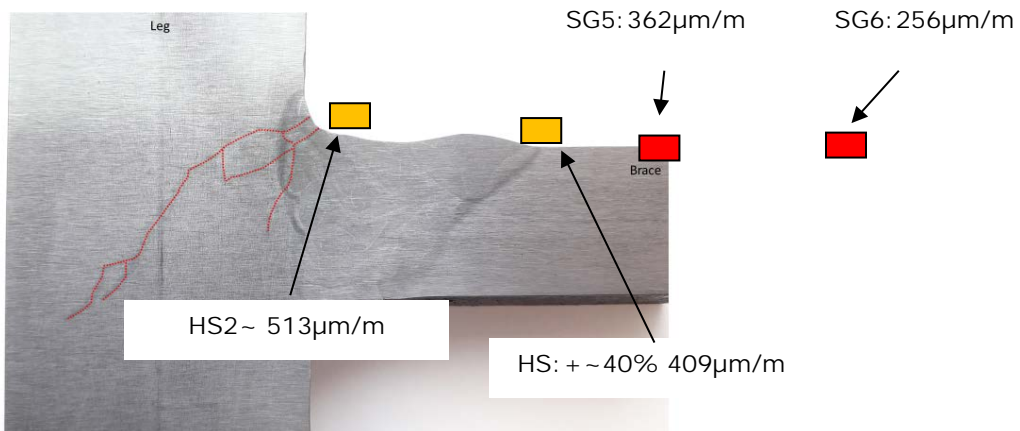


Figure 64 - Illustration of the shape of the weld and the crack location (sample G)

WP6 - FINITE ELEMENT SIMULATIONS ON THE STANDARD COMPONENTS

OBJECTIVES

The objective of this WP is to develop accurate finite element models, capable of predicting the mechanical behavior of welded tubular connections. The numerical models once tuned against experimental data are useful instruments to extend analysis to other geometries than those tested. In particular the following activities are planned:

- Development of Finite Element Models for the 3 different large scale tests to be performed in WP5
- Fine tuning of FEMs behind the experimental data
- Parametric analysis with developed models to extend experimental results to other Modular Jacket geometries selected for prefabrication

In the following details of the activities are reported.

TASK 6.1 DEVELOPMENT OF FINITE ELEMENT MODELS OF THE STANDARD COMPONENTS

OUT-OF-PLANE BENDING

A finite element model have been developed using the commercial code MSC Marc/Mentat software. The developed FE model is able to evaluate the strain-stress fields involved during the experimental fatigue tests. The model has been adopted for a sensitivity analysis reported in Deliverable 6.2.

The main features of the developed model are reported in the following and in Figure 65:

- steel bodies (chord and brace) have been modeled using four nodes thick-shell elements
- wood made internal reinforcements have been modeled with eight-nodes isoparametric brick elements
- linear materials model with steel elastic modulus = 190000 MPa and wood elastic modulus= 15000 MPa

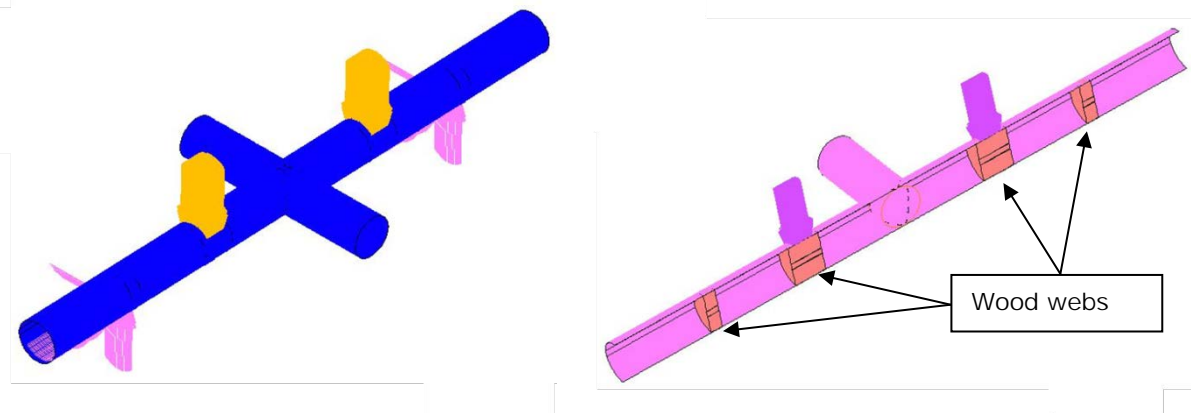


Figure 65 - Finite element model and boundary conditions.

In order to obtain the experimental results useful to calibrate the numerical model, a displacement/load controlled application procedure has been applied up to the defined target load of the specimen and relevant parameters extracted. In particular the longitudinal strain values on the tensile side of the specimen are extracted mostly near the welding zone and as far as to have a strain value not influenced by joint geometry.

In order to obtain the experimental results useful to calibrate the numerical model, a displacement/load controlled application procedure has been applied up to the defined target load of the specimen and relevant parameters extracted. In particular the longitudinal strain values on the tensile side of the specimen are extracted mostly near the welding zone and as far as to have a strain value not influenced by joint geometry.

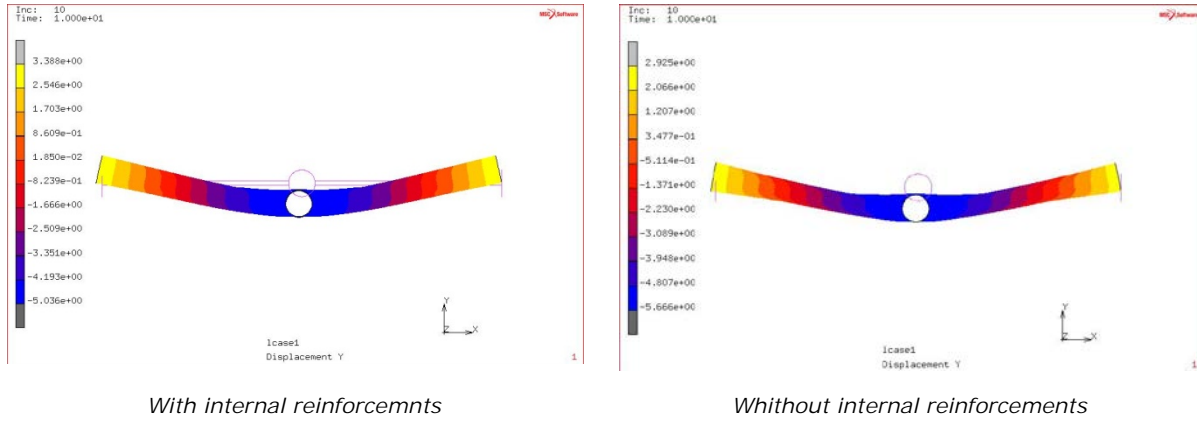


Figure 66 - Out-of-plane bending vertical displacements.

IN-PLANE BENDING

A numerical model was developed in general purpose finite element software in order to support the experimental program and to investigate the structural response of the joints under consideration. Based on the preliminary numerical analysis of the tests, the identification of the critical locations for the specimen instrumentation was achieved. In Figure 67, a schematic representation of the developed model is presented. The specimen and the experimental set-up used for the validation of the numerical model are presented in Task 5.2-5.3. In order to reduce the computational effort only the half joint was simulated and appropriate boundary conditions were used in order to restore the symmetry. A reference point, coupled to the end cross section of the brace was employed in order to apply the boundary conditions of a pin. Another reference point, coupled to the upper-end cross section of the chord, was used for the application of the force as shown in Figure 67. The model employs 4-node linear tetrahedron elements for the area close to the weld, while 3D brick elements were used at the areas away from the weld.

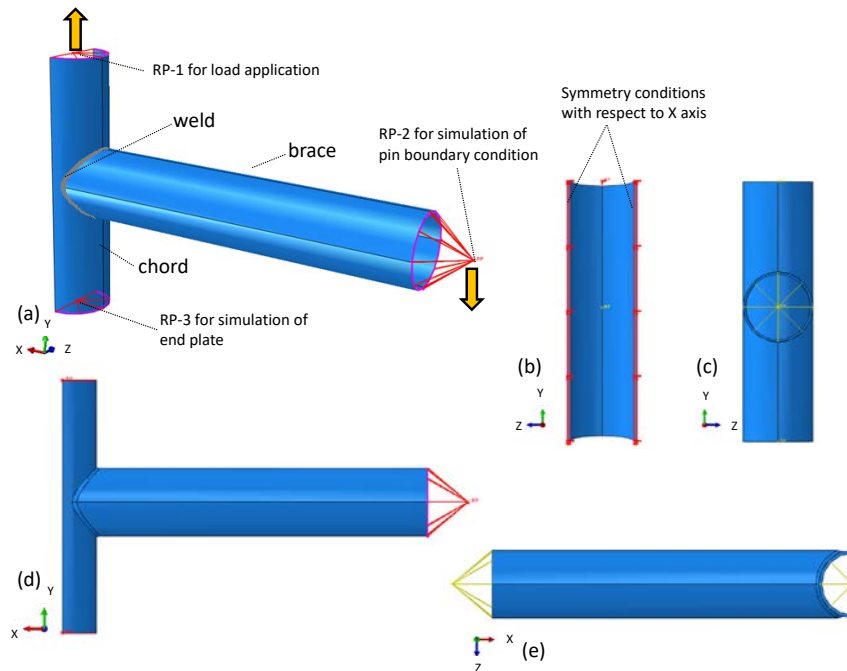


Figure 67 – General view of the numerical model.

Special attention has been paid in the accurate simulation of geometry of the weld. The weld profile was simulated accurately along all the circumferential of the joint and it is presented in Figure 68 together with the experimental material curve, was used in the numerical analysis. The material test was performed in the framework of WP5 and corresponds to axial direction of the chord.

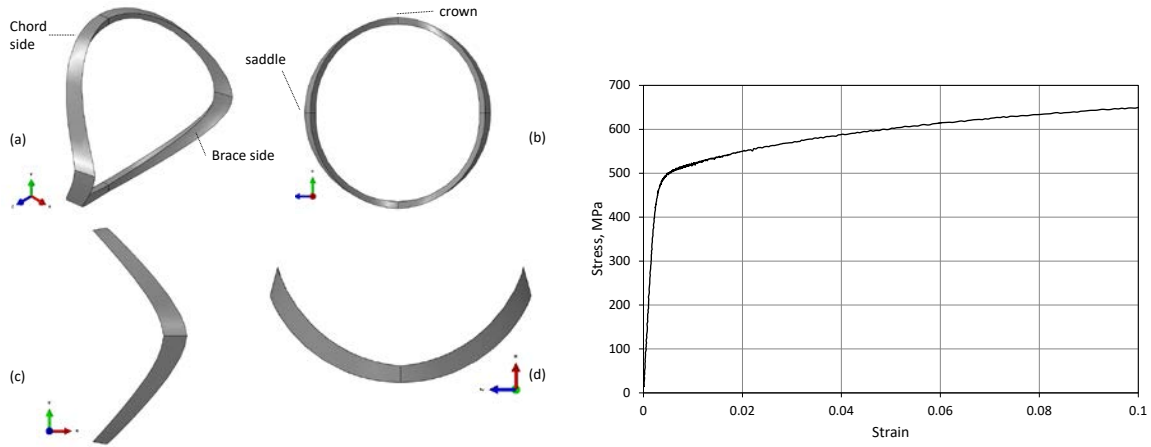


Figure 68 – Different views of weld part and experimental material curve used in numerical analysis.

FE MODEL FOR RESONANCE TESTING

PRINCIPLE OF SPECIMEN DESIGN FOR RESONANCE TESTING

The principle of the resonant test is to evaluate the fatigue performance of the component at full scale. Down-sizing the testing scale has the inconvenience that either the welding process is changed, or the size of the weld pool compared to the thickness member is significantly different. Also, instrumentation of small pipes for the determination of the stress concentrations is often less accurate, as the thickness of the component can be similar to the length of a typical strain gauge. Investigations have demonstrated that it is possible to excite non-axisymmetric tubular joints close to their resonance frequencies, provided that an adequate design of the specimen is achieved. As the specimen is non-axisymmetric, its stiffness is different in the out-of-plane bending (OPB) and in-plane bending (IPB) loading mode, and consequently, the eigen frequencies of these two resonance modes can differ. In practice, a test is normally performed at a frequency smaller than the lowest resonance frequency, and therefore the resonance mode with the lowest frequency will be typically more excited than the other mode. It is therefore an advantage to obtain eigenfrequencies as close as possible to each other.

COMPUTATION OF RESONANCE FREQUENCY

The first estimation of the resonance frequencies was performed by the finite element method using Abaqus 6.14.2. The specimen is modelled with shell elements. The brace end-masses and leg endplates are modelled with solid elements or attached masses and inertia moments. The shell mesh size is typically 10mm in the zones around the welds and up to 40mm at the brace ends which gives in total around 100.000 elements. For the eigenfrequency extraction, the Lanczos eigensolver is used.

A preliminary analysis was performed with brace lengths of 3.5m and a leg length of 2.4m. The eigen frequencies were 23.0Hz in IPB mode and 27.8Hz in the OPB mode. Different geometries were then investigated, but keeping the diameters of the brace and the leg so close did not allow to decrease sufficiently the difference of eigen frequencies. This is because the stiffness in the OPB mode is significantly higher than in the IPB. As the inner diameters of the tubes are equal, the stress in the brace, which is dominantly membrane, becomes almost completely membrane stress in the central component. It was then decided to increase slightly the outer diameter of the leg, in order to promote bending of the leg component in the IPB mode and therefore decrease its stiffness. After different runs of computations (in total, 50 iterations were performed), the dimensions of the leg were proposed as an outer diameter of 806mm and a length of 1480mm. With this geometry, the resonance frequencies of IPB and OPB are identical at 21.3Hz.

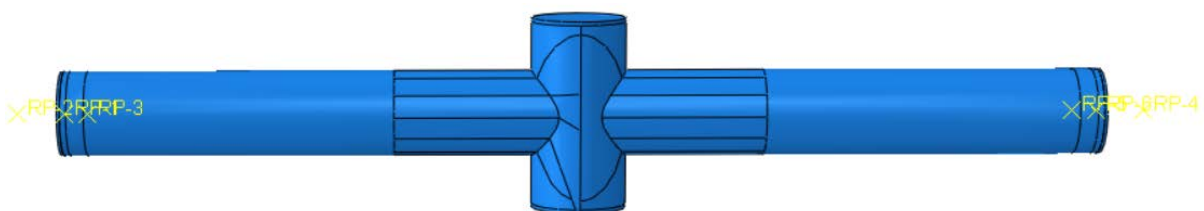


Figure 69 - Finite element model of the specimen (showing different paths for stress gradient extraction)

Drawings were then supplied by Idesa in order to purchase the components. Looking at providers of materials, the dimensions were slightly changed to a thickness of 20mm for the braces and 38.1mm for the leg. The diameter of the leg is increased from 806 to 813mm. New simulations were then performed on the basis of the workshop drawings. The resonance frequencies are estimated at 24.0Hz.

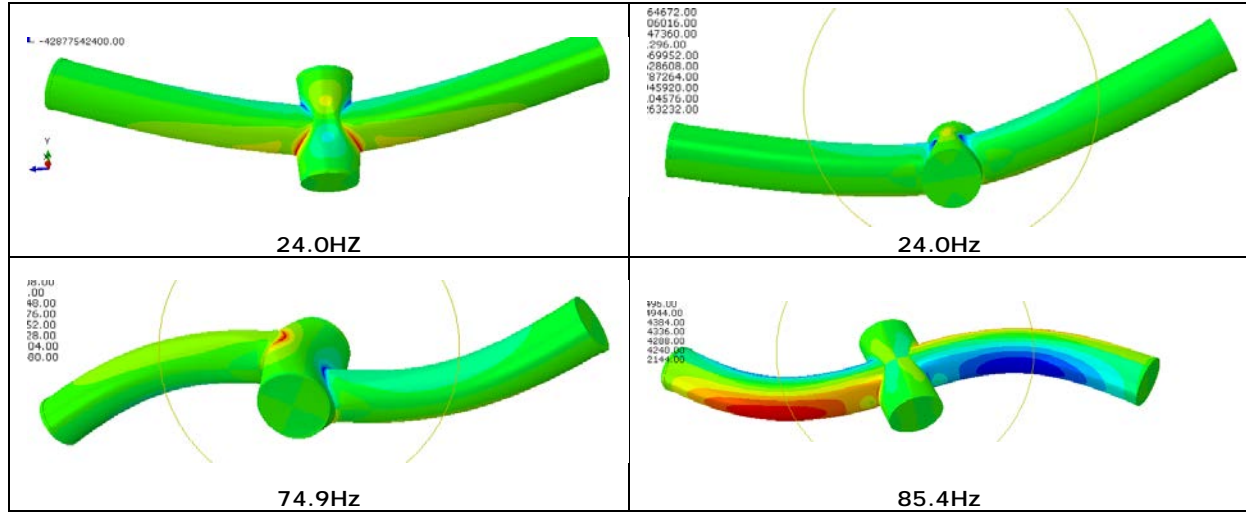


Figure 70 - Representation of the different mode shapes.

PREDICTION OF LOCAL STRESS / STRAIN

To predict the local stress and strains, models with solid elements C3D20R were used. These models were found to be more reliable than models with shell elements. Furthermore, they give the possibility to include the geometry of the weld. We investigated the frequency response with steady state dynamics analysis. The response to forced vibration provides real and imaginary stresses and deformations. The real component corresponds to an excitation in the out-of-plane direction, while the imaginary part corresponds to an excitation in the in-plane condition. When approaching resonance frequency, the response is out-of-phase compared to the excitation. For this reason, most of the results are reported according to the magnitude of the complex numbers. The excitation force is proportional to the square of the frequency, as it is a function of the rotating eccentric mass m , the frequency ω and the arm length of the rotating mass.

$$F = m \cdot r \cdot \omega^2$$

It was chosen to estimate the hot spot stresses from the magnitude of the first principal stress with the highest absolute value. To obtain the hot spot value, the selected quantity (first principal stress) was extracted at different locations along the length of the weld at different angular position along the brace and at a given distance from the intersection between the chord and the brace. In (DNVGL, 2016), the hot spot is computed from stress values measured at two locations. As the principal stress between the saddle and the crown positions is also of interest, it is necessary to extract the values along a path. The first path, reported as HS1 in the figures, is at 16.9 mm from the intersection. A second contour on the brace is located on the brace at 54.8mm. On the leg, the conventions are different at the saddle and crown positions, but practically rather close and leading to minor differences. Therefore, it was decided to use the distance of 16.9 and 41mm to compute the hot spot stresses. From the stresses at two positions, the value at the weld toe is extrapolated to obtain the hot spot value.

The first computation is performed assuming that the excitation of the sample follows a circle, corresponding to a single eccentric mass exciting the sample. In the next figures, 0 / 180° correspond to the saddle positions of the joint and 90 / 270° to the crown position. The nominal dimensions of the specimens are considered. One observes that the maximum is at the saddle positions on the brace and on the leg. The maximum values are quite similar between the brace and the leg, meaning that the failure could be almost equally present on the brace and on the leg if the thickness effect is neglected. Taking into account the thickness effect, failure is then to be expected on the leg. The stress distribution is quite similar on the brace and on the leg, with maxima of 120 MPa and minima of 60MPa. The evolution between maxima and minima is however slightly different at the intermediate positions. The prediction on the chord is not always very smooth; it is considered to be due to the selection of a point for an extraction in an element at a different distance from the weld toe.

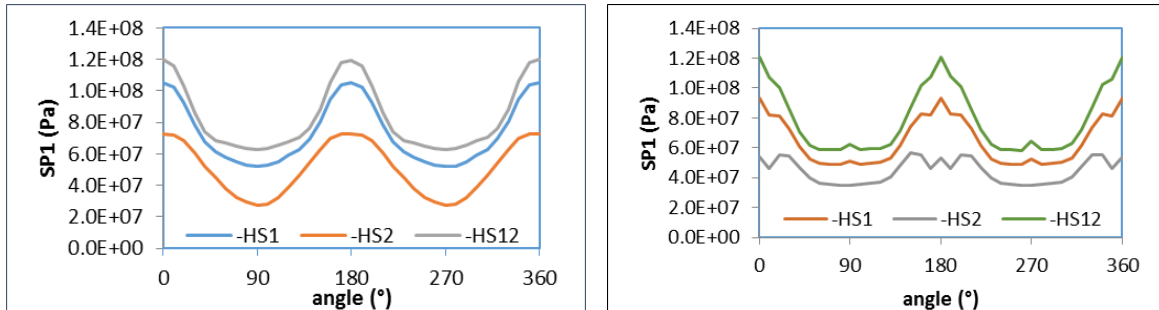


Figure 71 - Expected magnitude of the first principal stress in absolute distribution along the brace at a frequency of 23.08Hz, at two distance from the weld toe (HS1 and HS2) and the resulting hot spot stress value (HS12)

Knowing the distribution of the hot spot along the weld, it is possible to tune the compensation of the drive system such that the difference of hot spot stresses at 0/180° and 90/270° are reduced. The compensation was tuned at 32%. The resulting hot spot distribution along the weld are represented in Figure 72. The hotspot stresses on the brace are generally higher than on the leg/chord, except at the saddle positions.

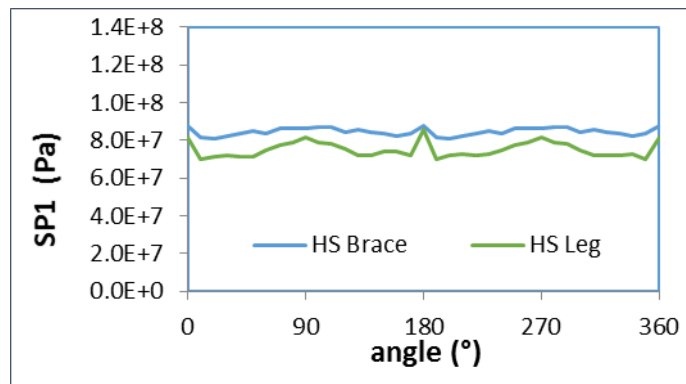


Figure 72 - Expected magnitudes of the hot spot stress on the chord and the brace sides for an elliptic loading

TASK 6.2 NUMERICAL SIMULATION OF EXPERIMENTAL RESULTS OF THE STANDARD COMPONENTS

OUT-OF-PLANE BENDING

The developed finite element model has been tuned with respect to strain gauge measurements of experimental tests (Task 5.2 Figure 55, details in Deliverable 5.2-5.3).

In order to accurately reproduce the SNCF and SCF at the saddle location (the most critical one in the out-of-plane bending condition) a fine mesh is necessary near the weld and effort has been made in capturing the actual bead geometry (Figure 73, details in Deliverable 5.1).



Figure 73 - Actual joint geometry.

Further improvement was made by changing the geometry of the brace in the intersection zone with the chord. In particular the mesh geometry is reported in Figure 74 where FEA 0 is the model with nominal geometry and FEA 16 is the tuning case with the weld thickness variations.

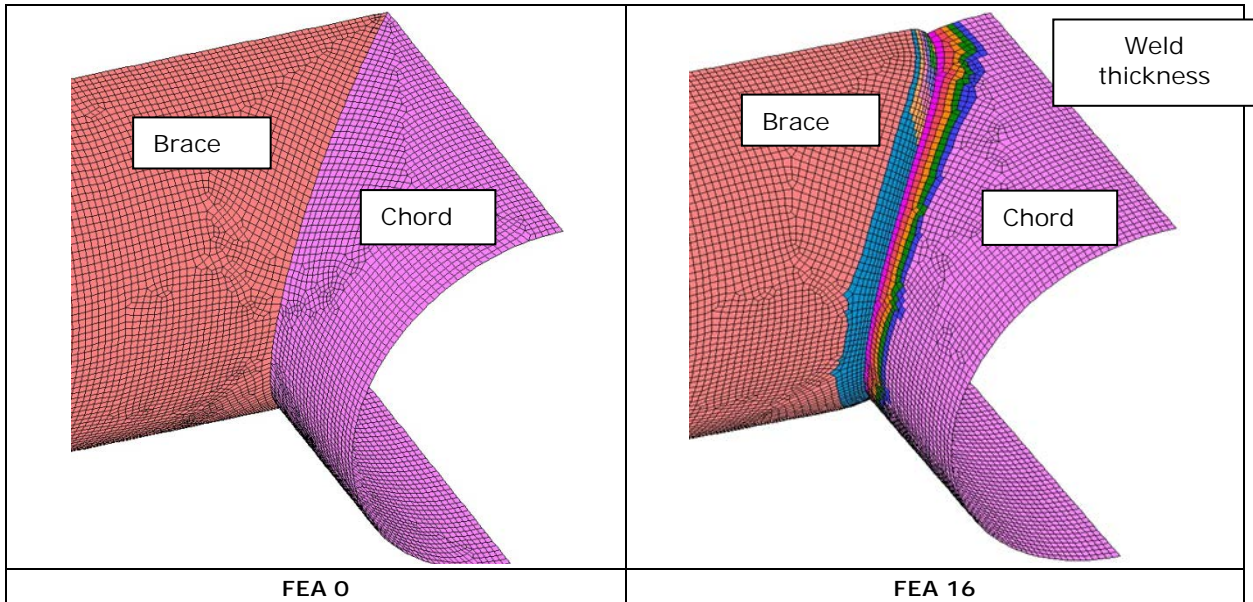


Figure 74 - Finite element model: without weld geometry (FEA 0) and with weld geometry modelled (FEA 16)

The comparison with strain gauges experimental measurements in terms of axial strain (Figure 75) and axial stresses (Figure 76) are reported showing the improvement achieved in the model matching experimental data.

As can be seen from Figure 76 the stress pattern on the chord side (where fatigue crack occurred) in well defined and by interpolation of values at a certain distance from the weld toe it is possible to extract the Hot Spot Stress value.

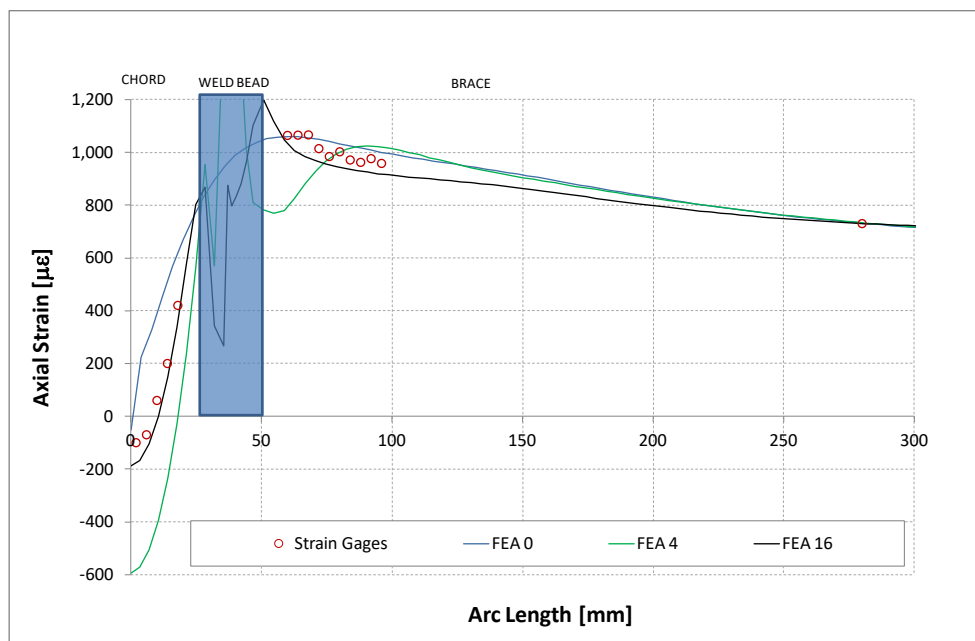


Figure 75 - Axial strains (brace direction): model vs. experimental.

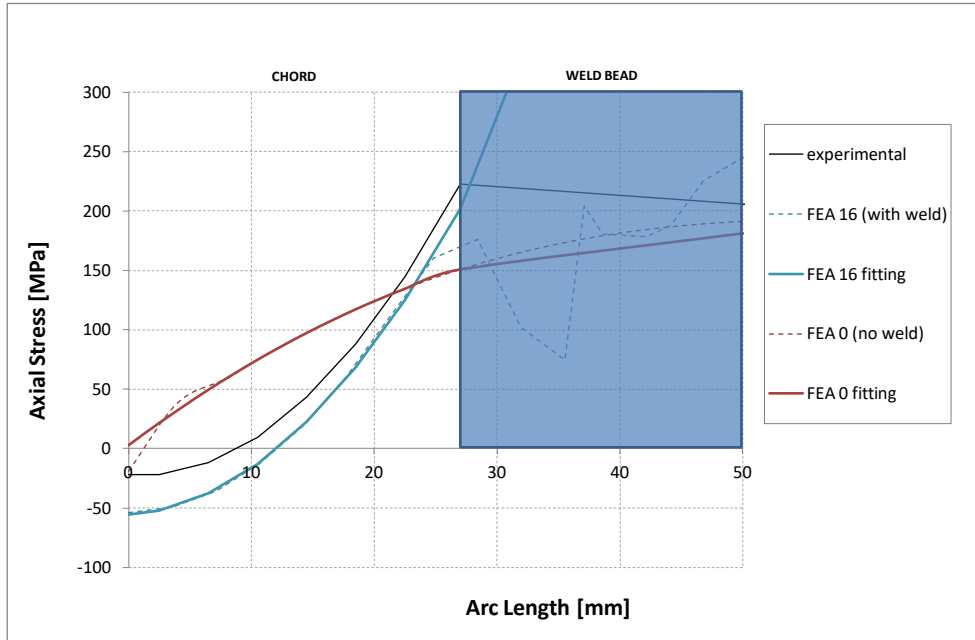


Figure 76 - Maximum principal stresses in axial brace direction.

IN-PLANE BENDING

The numerical model of in-plane-bending experiment (Task 5.2, Figure 57) was validated against the pilot test J1. In this test a monotonic loading was performed prior to fatigue loading in order to examine the structural response of the joint under monotonic loading. The comparison between experimental and numerical results in terms of force-displacement diagram is presented in Figure 77. Moreover the numerical simulation helped for the identification of the critical locations for the specimen instrumentation. Two areas were identified as critical locations as shown in Figure 78a and b. The first critical location, with the larger induced strains, was identified at the area between the saddle and the crown of the joint as shown in Figure 78a. The distance of the two yellow arrows (Figure 78a) was equal to 69 mm at the z-direction and 27 mm at the y-direction. The second one is located at the crown of the X-joint and presented in Figure 78b. The distance among the two yellow arrows (Figure 78b) at the x-direction is equal to 45 mm. Those two locations were instrumented in order to measure the maximum applied strains during fatigue loading.

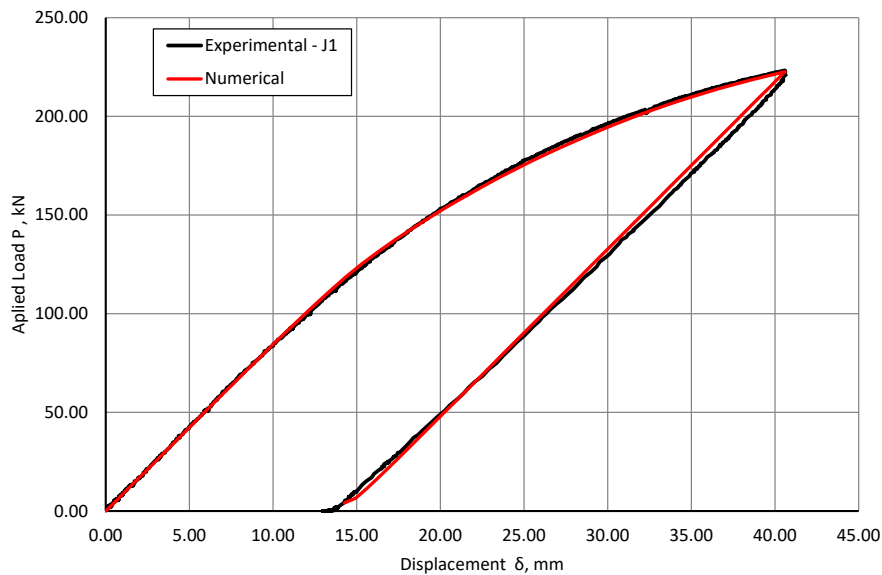


Figure 77 – Comparison of experimental and numerical results in terms of load - displacement diagram.

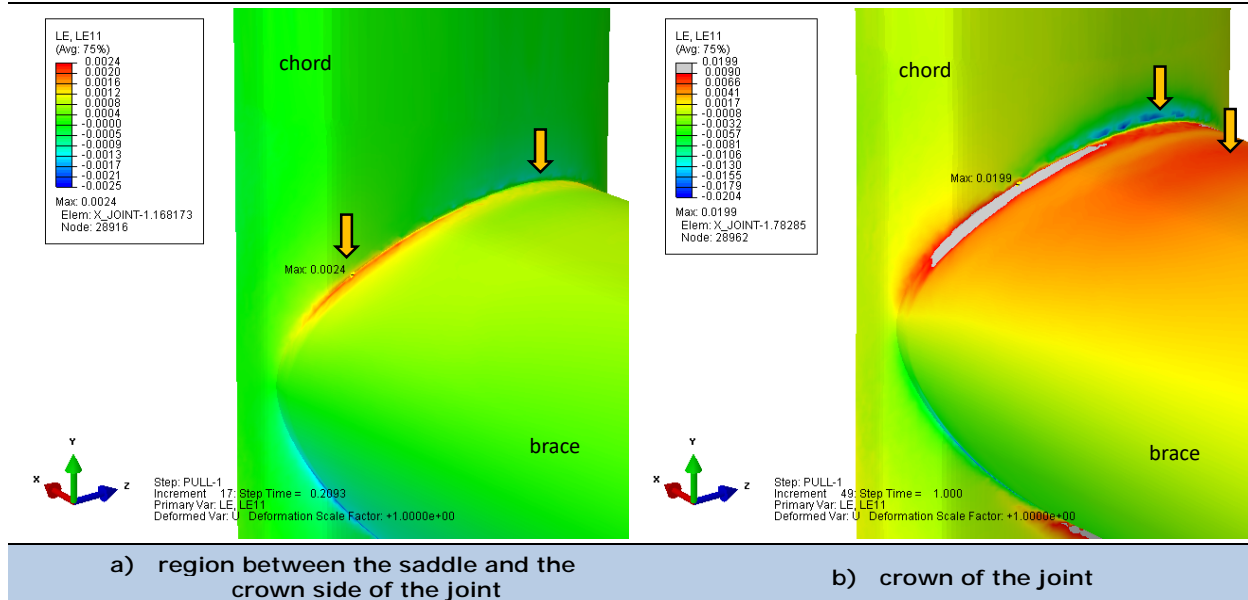


Figure 78 – Strain distribution at critical location of the joint.

The experimental results are in accordance with the prediction of the numerical models in terms of force-displacement response. Moreover, the numerical models were able to predict accurately the location of crack initiation. In all IPB tests the crack initiation was at the area between the saddle and the crown of the joint. The same location was identified numerically as the location with the higher stresses and strains as shown in Figure 78.

RESONANCE TESTING

After reception of the samples, it was observed that the thickness of the braces was lower than initially planned. The effective geometry of the specimens was measured with a 3D scanning system. New simulations were performed with the measured geometries, neglecting the shape of the weld. For sample A, a supplementary model was created with the measured weld geometry.

The purpose of the response analysis is to:

- compare the resonance frequencies between simulations and experimental results
- investigate the stress field along the weld
- compare displacement and strain gauge readings between simulations and experiments.

COMPARISON OF RESONANCE FREQUENCIES

There is a general good agreement between the resonance frequencies as computed and measured. When the weld geometry is included as for sample A, the agreement is almost perfect. All the simulations predict a slightly higher resonance frequency in the in-plane direction compared to the out-of-plane, with a difference of 0.2–0.3Hz. Experimentally, the resonance frequencies for in-plane bending are also slightly larger than for out-of-plane, with a difference of 0 to 0.5Hz.

Table 31 - Overview of computed and measured resonance frequencies

Sample	Resonance frequencies (Hz)				Model name
	Experimental		Finite element		
	IPB	OPB	IPB	OPB	
Nominal			24.0	24.0	
A w weld	24.1	23.7	24.1	23.8	A1WD4
A wo weld			23.9	23.7	A2D1
B	24	23.5	23.8	23.6	BD1
F	24.2	24.2	23.8	23.6	FD1
G	24.5	24	23.8	23.6	G6D1

STRESS DISTRIBUTION ALONG THE WELD

Sample G: Sample G was the first sample to be tested. The first experimental results tend to let think that the compensation predicted from the finite element simulation was too low, and so it was

decided to compensate with 66% (3+2kg). Simulation performed after the test indicate that the highest stress should be obtained on the brace. The hot spot stress at the saddle positions (0 and 180°) are predicted to be quite lower than at the crown position, where the profile would be rather flat.

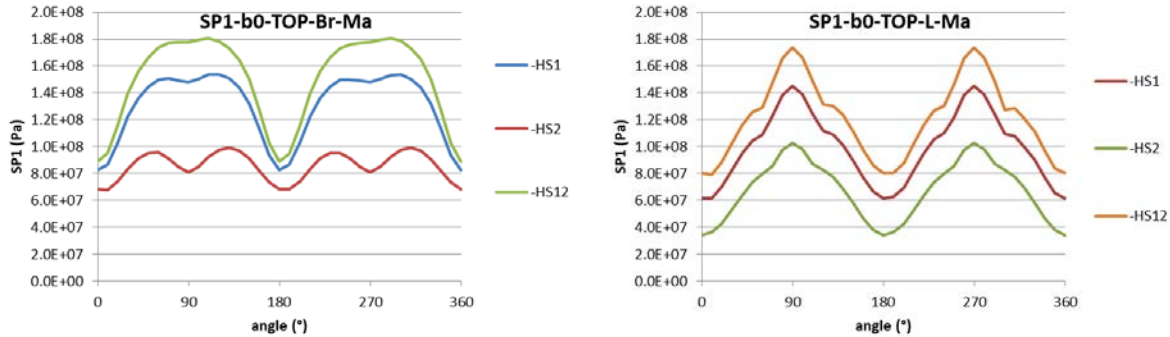


Figure 79 - First principal stress on tour contour at constant distance from the weld toe (HS1 and HS2) and the extrapolated hot spot stress (HS12), along the brace (top) and the chord (below).
Model G6D1, frequency 23.00Hz.

Sample A: Sample A was the second sample to be tested. As it was realized that the compensation for sample G was too high, it was reduced to 3+1.25kg. It is resulting in a more homogeneous stress pattern. There is a difference in prediction between the model with weld and the model without weld. The model with weld predicts higher stresses on the leg / chord at the crown positions (90/270°) and higher stresses on the braces at the saddle positions (0/180°). The model without weld predicts generally higher stresses on the brace.

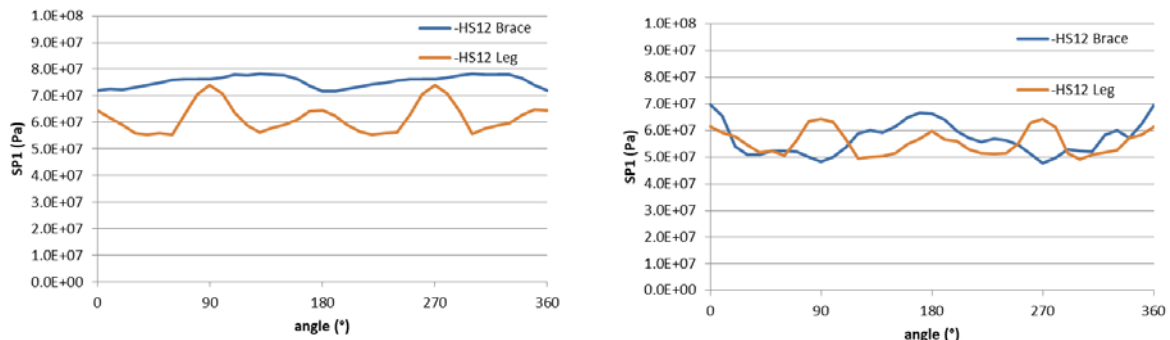


Figure 80 - Hot spot first principal stress on from a contour along the weld toe (HS12) for the brace and chord / leg. Left: For the model without weld. Model A2D1, frequency 23.08Hz. Right: For the model without weld. Model A1WD, frequency 23.17Hz.

Sample B: Sample B was only simulated with a model without weld. The model predicts a rather homogeneous hot spot along the brace, while on the chord/ leg it peaks close to the 90 / 270° positions.

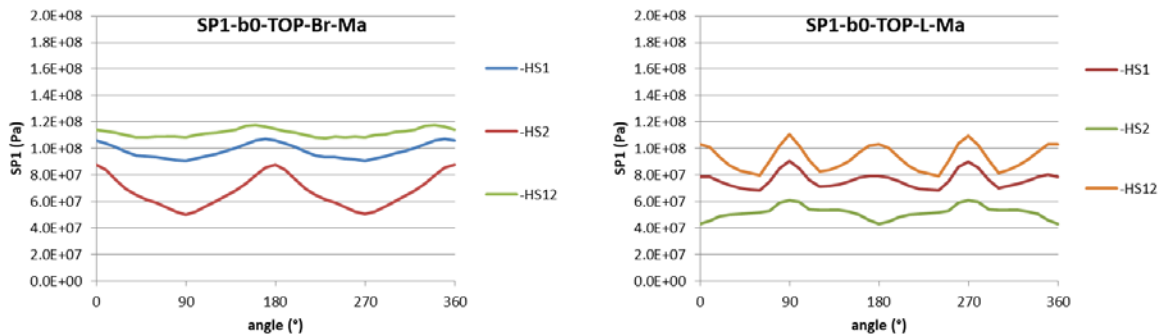


Figure 81 - First principal stress on tour contour at constant distance from the weld toe (HS1 and HS2) and the extrapolated hot spot stress (HS12), along the brace (top) and the chord (below).
Model BD1, frequency 22.83Hz.

Sample F: For sample F, the conclusions are similar to sample B, except that the hot spot stress on the brace at the in-plane bending is slightly lower at 0/180° instead of 90/270°. The hot spot on the leg is on the other hand larger at the 90/270°. It is the only position where it is close to the value on the brace.

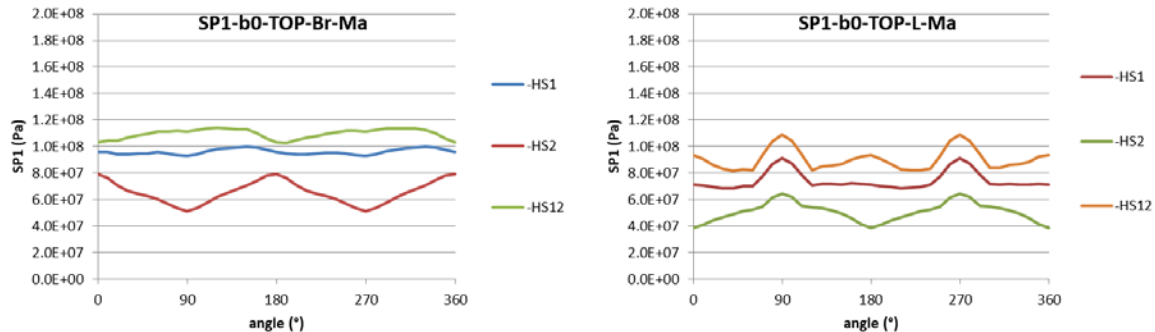


Figure 82 - First principal stress on tour contour at constant distance from the weld toe (HS1 and HS2) and the extrapolated hot spot stress (HS12), along the brace (top) and the chord (below).
Model FD1, frequency 22.85Hz.

STRAIN RESPONSE

The correspondence between the strain gauge readings and the finite element simulations are focused on sample A, as a model with weld and without weld are available. In order to compare the strain readings with finite element results, it is necessary to select the adequate frequency from the finite element simulations. In the ideal case, the same excitation frequency would be chosen for the simulation as in the experiment. However, as the test is performed very close to the resonance frequency, the result is very sensitive to a small variation of the difference between the excitation frequency and the resonance frequency. Furthermore, due to the geometry, the first resonance frequency mode is slightly different from the second one. Although the agreement between the computed eigen frequencies and the experimental ones is very good, one cannot expect that the response to a given excitation will be similar in the simulation and in the experiment unless a very tedious fitting process is performed. This is illustrated in Figure 83. Generally, the experimental displacement is rather close to the finite element one. However, close to the resonance frequency, they deviate significantly. At the test frequency of 23.55Hz, only one displacement is matched (in-plane bending with the weld). Some improvement could be possible by changing the dissipation factor in the simulation, but it will affect both bending modes. Modifying the model to match both displacement at the testing frequency is actually very difficult, because it requires to fit other parameter for in-plane and out-of-plane bending.

As alternative, we propose to scale the results from the finite element simulations by a factor such that the computation results at a given frequency fit with reading of the strain gauge located far from the welds (550mm). The frequency in the computation is chosen such that the ratios of the displacements in-plane and out-of-plane are in the same ratio as in the experiment. (Figure 83) compares the displacements IPB and OPB of the experiment and the simulation. From this comparison, it was decided to compare the results at a frequency of 23.16 Hz for the model where the welds were modelled. For the case where the weld was not present in the model, then the selected frequency is 23.08 Hz.

The difference of resonance frequency IPB and OPB is not exactly the same in the simulation as in the experiment, and therefore the scaling factor is typically different in the OPB and IPB direction. By selecting the frequency as previously, the differences are reduced, but can still be significant. Therefore, two scaling factors are used for IPB and OPB directions. As strain gauges are located at intermediate positions, an intermediate scaling factor is also used. The following formula is proposed for this interpolation, based on the angular position along the brace, which assumes that the forces follow a sinusoidal pattern between IPB and OPB.

$$\text{Scaling} = \sqrt{(\text{Scaling}_{OPB} \cdot \cos\theta)^2 + (\text{Scaling}_{IPB} \cdot \sin\theta)^2}$$

Locating the strain gauges proved to be challenging. They are placed at a given distance from the weld toes, but the laboratory does not have absolute coordinates. Absolute coordinates are necessary on the other hand to locate and extract the strain measurements in the finite element model. Therefore, the strategy to determine the position of the strain gauges in the model was to consider that the strain gauges were at the prescribed distance from the weld toe, in the direction perpendicular to the weld toe. To be able to compare in the model without weld, the absolute coordinates obtained in the model with weld were taken over. Furthermore, the strain gauges are in direction that are not always parallel to the main directions of the samples. The direction corresponding to the intersection between the plane perpendicular to the weld for a given angular position and the surface of the specimen was thus applied as the direction of the strain gauge. To

compare with the experimental results, it is necessary to project the strain tensors on this direction. When the model includes a weld, the disagreement is in general smaller than 4%; if the weld is not modelled, the agreement is slightly poorer, typically 7%. However, to achieve such a good agreement when the weld is not modelled, it is necessary to know accurately the position of the strain gauges, which requires the modelling of the weld.

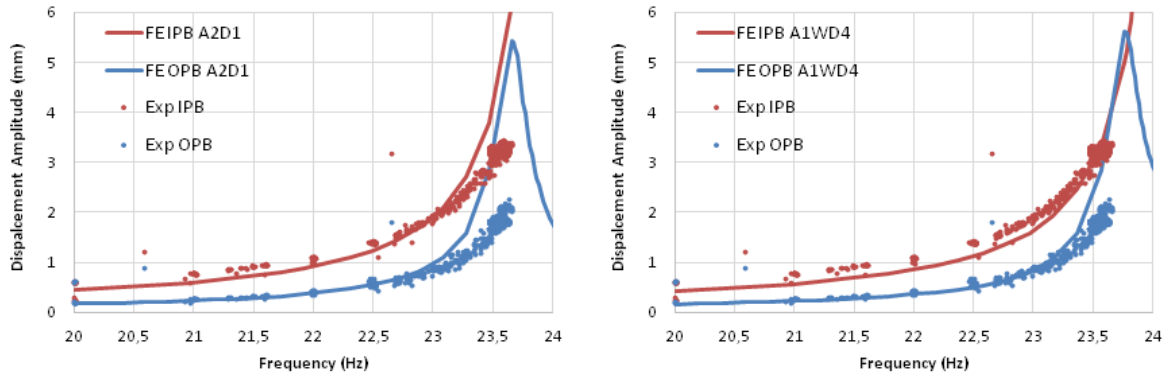


Figure 83 - Displacement at the middle of the sample, experimentally and predicted by finite element simulation for the model without weld (left) and for the model with weld (right).

Table 32 - Comparison of the experimental strain gauge reading (5th column) and the finite element simulation (column FEA). The relative difference is indicated in the last column. Simulation for the model without weld (A2D1).

SG#	Descr.	Br / Leg	Left/Right	Experiment	FEA	23.08Hz
1	ref 12u	Brace	LEFT	250	250	0%
31	ref 12u	Brace	RIGHT	242	244	1%
3	ref 6u	Brace	LEFT	246	250	1%
2	ref 3u	Brace	LEFT	189	189	0%
32	ref 3u	Brace	RIGHT	185	174	6%
4	ref 9u	Brace	LEFT	190	188	1%
5	A 12u	Brace	LEFT	273	222	21%
6	B 12u	Brace	LEFT	189	175	8%
11	A 6u	Brace	LEFT	260	231	12%
12	B 6u	Brace	LEFT	180	174	4%
21	A 12u	Brace	RIGHT	289	229	23%
25	A 6u	Brace	RIGHT	248	226	9%
8	A 3u	Brace	LEFT	382	438	14%
9	B 3u	Brace	LEFT	296	306	3%
14	A 9u	Brace	LEFT	441	399	10%
15	B 9u	Brace	LEFT	300	287	4%
23	A 3u	Brace	RIGHT	399	370	8%
27	A 9u	Brace	RIGHT	402	374	7%
17	A 12u	Leg	LEFT	337	322	5%
18	B 12u	Leg	LEFT	221	220	1%
19	A 3u	Leg	LEFT	331	332	0%
20	B 3u	Leg	LEFT	207	210	1%
29	A 12u	Leg	RIGHT	347	308	12%
30	A 3u	Leg	RIGHT	308	312	1%
7	1u	Brace	LEFT	232	198	16%
10	5U	Brace	LEFT	215	212	1%
13	7u	Brace	LEFT	211	210	1%
16	11u	Brace	LEFT	269	212	24%
22	1u	Brace	RIGHT	277	203	31%
24	5u	Brace	RIGHT	252	199	24%
26	7U	Brace	RIGHT	256	198	26%
28	11u	Brace	RIGHT	236	214	10%

Table 33 - Comparison of the experimental strain gauge reading (5th column) and the finite element simulation (column FEA). The relative difference is indicated in the last column. Simulation for the model with weld (AWD4).

SG#	Descr.	Br / Leg	Left/Right	Experiment	FEA	23.00Hz
1	ref 12u	Brace	LEFT	250	250	0%
31	ref 12u	Brace	RIGHT	242	243	0%
3	ref 6u	Brace	LEFT	246	250	2%
2	ref 3u	Brace	LEFT	189	189	0%
32	ref 3u	Brace	RIGHT	185	173	7%
4	ref 9u	Brace	LEFT	190	188	1%
5	A 12u	Brace	LEFT	273	266	3%
6	B 12u	Brace	LEFT	189	183	3%
11	A 6u	Brace	LEFT	260	263	1%
12	B 6u	Brace	LEFT	180	180	0%
21	A 12u	Brace	RIGHT	289	296	2%
25	A 6u	Brace	RIGHT	248	284	14%
8	A 3u	Brace	LEFT	382	436	13%
9	B 3u	Brace	LEFT	296	306	3%
14	A 9u	Brace	LEFT	441	415	6%
15	B 9u	Brace	LEFT	300	292	2%
23	A 3u	Brace	RIGHT	399	372	7%
27	A 9u	Brace	RIGHT	402	384	4%
17	A 12u	Leg	LEFT	337	351	4%
18	B 12u	Leg	LEFT	221	232	5%
19	A 3u	Leg	LEFT	331	333	1%
20	B 3u	Leg	LEFT	207	211	2%
29	A 12u	Leg	RIGHT	347	341	2%
30	A 3u	Leg	RIGHT	308	310	1%
7	1u	Brace	LEFT	232	227	3%
10	5U	Brace	LEFT	215	272	23%
13	7u	Brace	LEFT	211	252	18%
16	11u	Brace	LEFT	269	272	1%
22	1u	Brace	RIGHT	277	253	9%
24	5u	Brace	RIGHT	252	249	1%
26	7U	Brace	RIGHT	256	256	0%
28	11u	Brace	RIGHT	236	233	1%

In the experiments, the highest hot spot strains were measured on the brace at the saddle, followed by the chord at the crown. Corrected by thickness effect, failure should be predicted at the chord. Cracks were essentially observed at the weld toe on the chord. Breakthrough failure was in three cases through the brace. To the question: why the cracks were at the weld toe on the leg and not on the brace, it seems that the specific geometry of the weld, a weld length without reinforcement, is pointing out that the failure can be at the first sharp intersection, being at the chord. A crack present there could propagate either in the brace or in the leg.

In order to better understand why a crack would propagate either through the chord or through the brace, it is proposed to look at the stress profile starting from the intersection for the model of sample A without weld. The strain gauges are located at 17 and 55mm distance on the brace, plus considering a weld length of 25mm, likely 42 and 80mm. The element size is approximately 10mm. One sees in Figure 84 that the stress is higher at the saddle position (0°) far from the weld, but the stress decreases close to the weld between the strain gauge location and the intersection point. Consequently, the stress derived from an extrapolation of the strain gauges at 42 and 80mm will likely be exaggerated compared to the effective hot spot stress. On the other hand, the stress at the crown is increasing until the weld toe. The values in the last element are likely less representative, but visually a hot spot value of 90MPa seems realistic at the crown, while it would be only 60 MPa at the saddle. On the chord, the strain gauges are located closer to the intersection, and the weld length is more of the order of a few mm. The extrapolation seems linear either for the crown and saddle positions. The lines have different offset and slopes but will finish close to 70-80MPa. This analysis shows that the strain measurements do not always describe the stress condition at the crack location, because the weld shape is moving them away from the crack position. The current analysis shows that the stress condition at the crack location could be similar for the brace and for the chord. It is also possible that the bifurcation that is observed in the experiments is very specific to the geometry of 90° X-joint. A crack present in a weld with a different shape will generally not the possibility to bifurcate towards one member or the other.

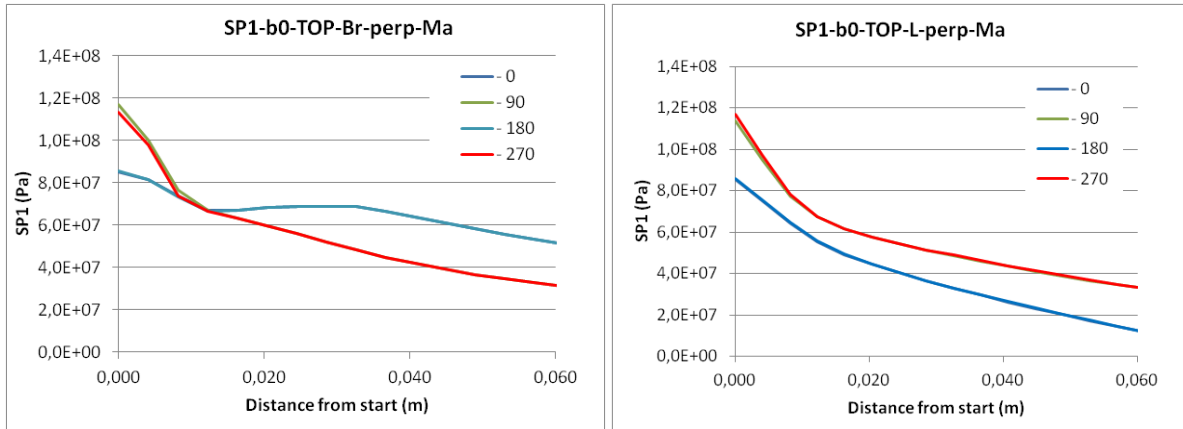


Figure 84 - Comparison of the first principal stress close to the weld toe on the brace (left) and on the chord (right) model A2D1 23.08Hz

TASK 6.3 NUMERICAL PARAMETRIC STUDY

SCFs OF MODULAR JACKET PREFABRICATED JOINTS

Stress concentrations factors were determined by the finite element method for the three main load cases for X-joint: in-plane bending, out-of-plane bending and axial loading. The stress concentration factor is determined by the ratio between the hot spot stress and the nominal stress. Models with solid elements C3D20R and a mesh size of 0.01m or smaller. Compared to the real structure, the braces and chord were made much longer to decrease end effects.

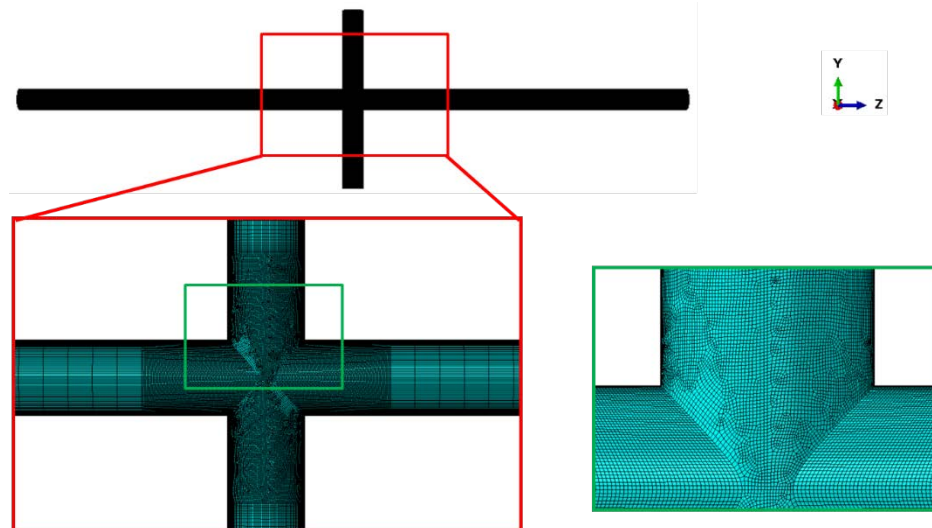


Figure 85 - Illustration of a model for the computation of stress concentration factor

At the end of each brace, two reference points are placed and linked to a ring of nodes. One point is exactly at the end of the brace and the other is at 40cm from the end. In the case of axial force, a force of 1MN is applied on each side in opposite direction. For the OPB and IPB cases, the inner reference point have three displacements blocked, while an horizontal or vertical force is applied on the outer reference nodes for the case OPB or IPB respectively. The analysis of the stress field is applied as in the previous section, where the values (first principal stress) at two contours of points located at a constant distance from the intersection are extracted and extrapolated back to the intersection.

The computation for these cases is presented in Table 34. As in other simulations, the saddle positions are at 3/9h / 0 /180°, while the crown positions are at 12/6h / 90 / 270° (Figure 86). In the computations, no weld geometry was included.

Table 34 - Geometry investigated for the stress concentration factors

Chord									
T	mm	30	35	35	35	35	35	40	10
D	mm	628	638	739	790	841	942	1003	228
L	mm	5300	5300	5300	5300	5300	5300	5300	5300
brace									
t	mm	21	21	21	21	21	21	21	6
d	mm	610	610	711	762	813	914	965	220
theta	°	90	90	90	90	90	90	90	90

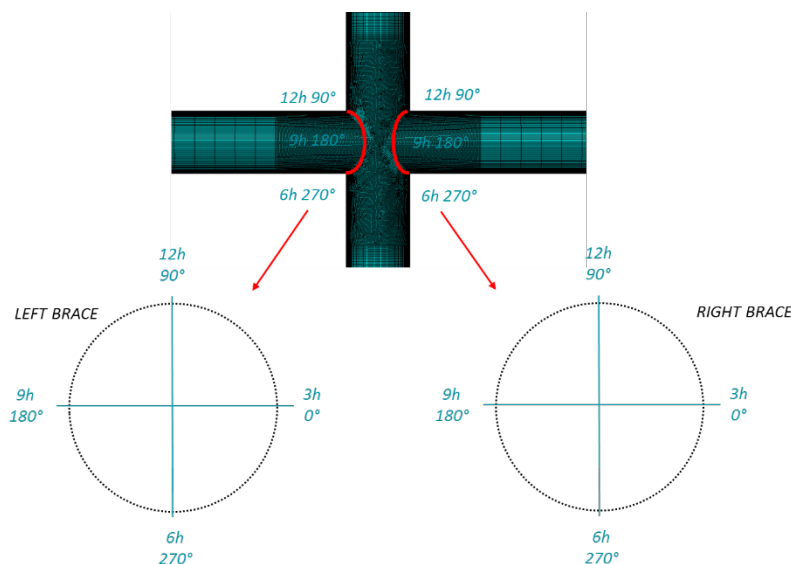


Figure 86 - Location for extraction of the data

An example will be detailed here: the case of chord of 610 outer diameter with wall thickness of 30mm, combined with a brace of thickness 21mm. The other results will only be summarized. Although standard sizes for tubes are given by the outer diameter, it is standard practice in the offshore industry to let the inner diameter match between a can and the rest of a brace or a leg. As a consequence, an X-joint 610-30-21 will actually combine two tubes of outer diameter 628 and 610mm. The distribution of the stress for axial loading is represented in Figure 87. Surprisingly, there is a minimum of the hot spot stress at the saddle on the brace and on the chord exactly at the saddle position. Slightly next to that position, the maximum stress is found. Our first impression was that a mistake was present in the computation or in the interpolation. However, a specific look at the stress distribution show that the chord comes in compression at the saddle point (Figure 88 and Figure 89). The braces are less in tension just in front of the saddle point (Figure 90).

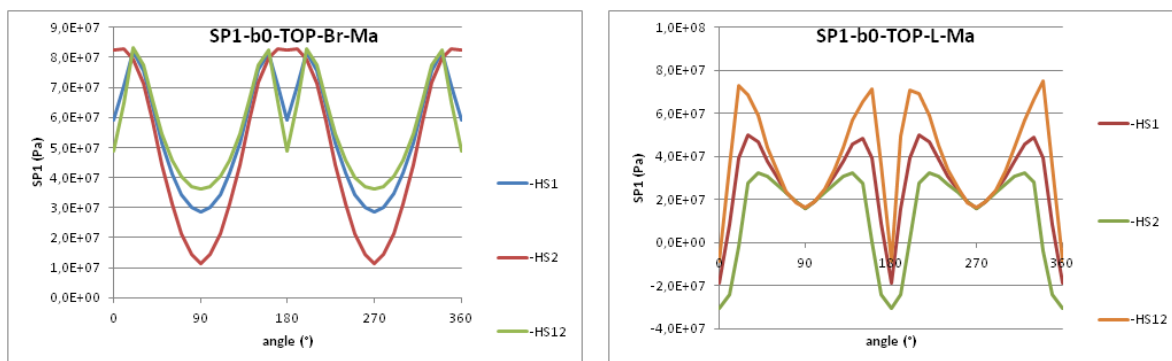


Figure 87 - First principle stress on two contours (HS1 and HS2) at given distance from the intersection between the tubes, and the extrapolated resulting hot spot (HS12) value. Above: values on the brace, below on the chord.

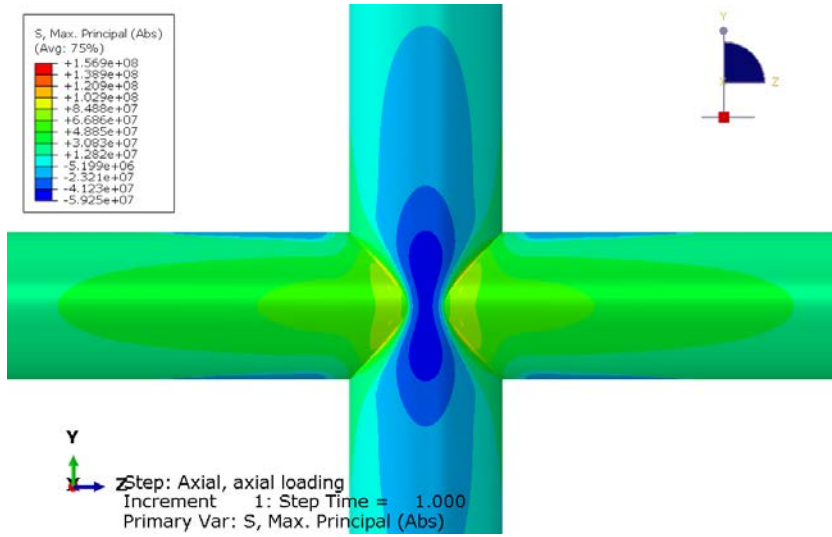


Figure 88 - First principal stress for axial loading of case 610-30-21.

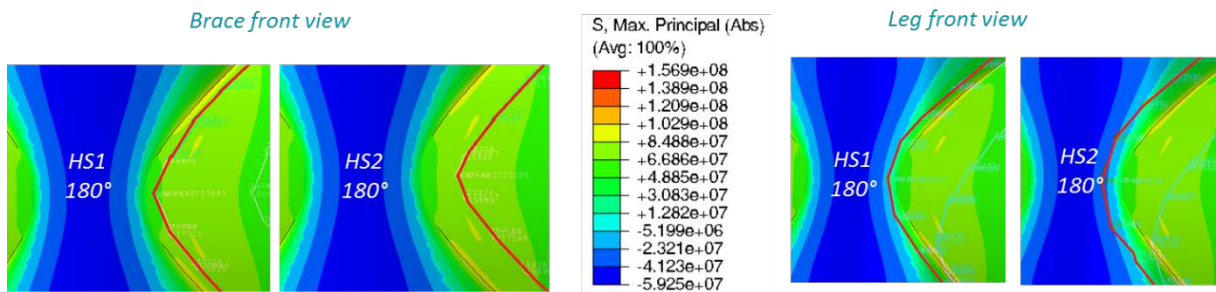


Figure 89 - First principal stress for axial loading of case 610-30-21, with the location of the contours for the extrapolation for the hot spot stress.

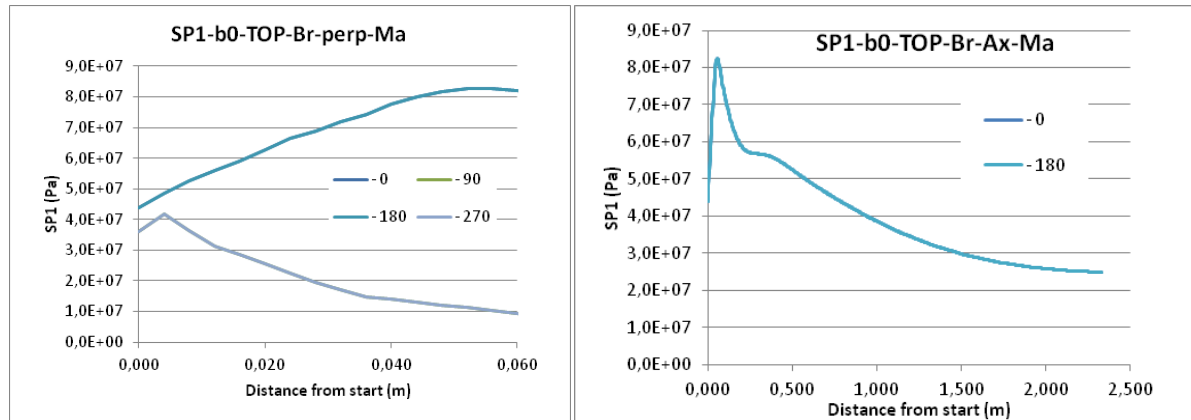


Figure 90 - Evolution of the first principal stress close to the weld toe (0:weld toe).

The values of the hot spot principal stress is then divided by the nominal value to obtain the stress concentration factor. From approximately 2m from the weld toe is the nominal value reached. A table containing the different stress concentration factors for the different angle is then looked for to determine the absolute SCF. The present computation illustrate that it is necessary to look around the complete circumference of the weld for the highest stress concentration factor and not only on a single line.

Table 35 - Example of resulting table for the stress concentration factors for the three load cases for 610-30-21

Angle	Axial force				OPB				IPB			
	HS12 Brace	SCF Brace	HS12 Leg	SCF Leg	HS12 Brace	SCF Brace	HS12 Leg	SCF Leg	HS12 Brace	SCF Brace	HS12 Leg	SCF Leg
0	4.88E+07	1.88	-8.65E+06	-0.33	1.09E+07	1.50	8.88E+06	1.22	3.74E+03	0.00	5.57E+05	0.08
10	6.50E+07	2.50	3.55E+07	1.36	1.27E+07	1.74	1.17E+07	1.61	5.70E+06	0.78	3.20E+06	0.44
20	8.34E+07	3.21	7.31E+07	2.81	1.41E+07	1.95	1.17E+07	1.61	1.16E+07	1.60	1.12E+07	1.54
30	7.76E+07	2.98	6.89E+07	2.65	1.21E+07	1.67	1.15E+07	1.58	1.44E+07	1.98	1.33E+07	1.83
40	6.58E+07	2.53	5.92E+07	2.28	9.28E+06	1.28	9.05E+06	1.25	1.51E+07	2.08	1.55E+07	2.13
50	5.46E+07	2.10	4.39E+07	1.69	6.58E+06	0.90	6.16E+06	0.85	1.48E+07	2.03	1.54E+07	2.13
60	4.58E+07	1.76	3.42E+07	1.32	4.36E+06	0.60	4.15E+06	0.57	1.38E+07	1.89	1.58E+07	2.17
70	4.03E+07	1.55	2.36E+07	0.91	3.29E+06	0.45	2.20E+06	0.30	1.26E+07	1.73	1.46E+07	2.01
80	3.71E+07	1.43	1.87E+07	0.72	2.77E+06	0.38	1.09E+06	0.15	1.11E+07	1.53	1.48E+07	2.04
90	3.61E+07	1.39	1.61E+07	0.62	9.62E+05	0.13	4.88E+03	0.00	1.04E+07	1.43	1.46E+07	2.01
100	3.72E+07	1.43	1.91E+07	0.74	2.78E+06	0.38	1.14E+06	0.16	1.12E+07	1.54	1.51E+07	2.08
110	4.03E+07	1.55	2.50E+07	0.96	3.29E+06	0.45	2.27E+06	0.31	1.25E+07	1.72	1.53E+07	2.11
120	4.59E+07	1.77	3.36E+07	1.29	4.37E+06	0.60	4.11E+06	0.57	1.38E+07	1.90	1.57E+07	2.16
130	5.46E+07	2.10	4.40E+07	1.69	6.57E+06	-0.90	-6.18E+06	-0.85	1.47E+07	2.03	1.54E+07	2.12
140	6.58E+07	2.53	5.70E+07	2.19	9.29E+06	-1.28	-8.74E+06	-1.20	1.51E+07	2.08	1.49E+07	2.05
150	7.77E+07	2.99	6.55E+07	2.52	-1.21E+07	-1.67	-1.10E+07	-1.51	1.44E+07	1.98	1.26E+07	1.74
160	8.24E+07	3.17	7.13E+07	2.74	-1.40E+07	-1.92	-1.16E+07	-1.60	1.15E+07	1.58	1.08E+07	1.49
170	6.54E+07	2.51	3.61E+07	1.39	-1.28E+07	-1.75	-1.18E+07	-1.62	5.72E+06	0.79	4.34E+06	0.60
180	4.88E+07	1.88	-8.65E+06	0.33	-1.09E+07	1.50	8.88E+06	1.22	4.18E+03	0.00	-5.57E+05	-0.08
190	6.49E+07	2.50	4.96E+07	1.91	-1.27E+07	-1.74	-1.19E+07	-1.63	-5.70E+06	-0.78	-6.41E+06	-0.88
200	8.27E+07	3.18	7.05E+07	2.71	-1.40E+07	-1.93	-1.17E+07	-1.60	1.15E+07	-1.59	-1.08E+07	-1.48
210	7.76E+07	2.98	6.89E+07	2.65	-1.21E+07	-1.67	-1.15E+07	-1.58	-1.44E+07	-1.98	-1.33E+07	-1.83
220	6.58E+07	2.53	5.91E+07	2.27	-9.28E+06	-1.28	-9.04E+06	-1.24	-1.51E+07	-2.08	-1.55E+07	-2.13
230	5.45E+07	2.10	4.52E+07	1.74	-6.56E+06	-0.90	-6.32E+06	-0.87	-1.47E+07	-2.03	-1.58E+07	-2.18
240	4.59E+07	1.77	3.41E+07	1.31	-4.37E+06	-0.60	-4.13E+06	-0.57	-1.38E+07	-1.90	-1.58E+07	-2.17
250	4.02E+07	1.55	2.53E+07	0.97	-3.29E+06	-0.45	-2.29E+06	-0.32	-1.25E+07	-1.72	-1.53E+07	-2.11
260	3.71E+07	1.43	1.87E+07	0.72	-2.77E+06	-0.38	-1.09E+06	-0.15	-1.11E+07	1.53	-1.48E+07	-2.03
270	3.61E+07	1.39	1.61E+07	0.62	-9.62E+05	-0.13	4.71E+03	0.00	-1.04E+07	-1.43	-1.46E+07	-2.01
280	3.72E+07	1.43	1.91E+07	0.73	2.77E+06	0.38	1.12E+06	0.15	-1.12E+07	1.54	-1.50E+07	-2.07
290	4.04E+07	1.55	2.44E+07	0.94	3.30E+06	0.45	2.25E+06	0.31	-1.25E+07	1.73	-1.51E+07	-2.08
300	4.59E+07	1.77	3.29E+07	1.26	4.37E+06	0.60	4.04E+06	0.56	-1.38E+07	-1.90	-1.54E+07	-2.11
310	5.46E+07	2.10	4.41E+07	1.69	6.57E+06	0.90	6.19E+06	0.85	-1.48E+07	-2.03	-1.55E+07	-2.13
320	6.58E+07	2.53	5.69E+07	2.19	9.29E+06	1.28	8.73E+06	1.20	-1.51E+07	-2.08	-1.49E+07	-2.05
330	7.76E+07	2.99	6.66E+07	2.56	1.21E+07	1.67	1.11E+07	1.53	-1.44E+07	-1.98	-1.29E+07	-1.77
340	8.24E+07	3.17	7.53E+07	2.90	1.40E+07	1.92	1.17E+07	1.61	-1.15E+07	-1.58	-1.17E+07	-1.61
350	6.53E+07	2.51	3.55E+07	1.37	1.27E+07	1.75	1.17E+07	1.60	-5.72E+06	-0.79	-4.30E+06	-0.59
360	4.88E+07	1.88	-8.65E+06	-0.33	-1.09E+07	1.50	8.88E+06	1.22	3.74E+03	0.00	-5.57E+05	0.08

INFLUENCE OF ASSEMBLY IMPERFECTIONS

The influence of assembly imperfection on the local stress riser with particular reference to the SCF value has been evaluated. The FE model tuned against experimental test on out-of-plane bending loading conditions have been applied. The out-of-plane bending loading being of particular relevance for the out-of-plane assembly imperfections. In this analysis axial misalignments between chord and brace of a magnitude up to 4 mm have been considered. The brace-chord misalignments have been applied both at the extrados (+) and at the intrados (-), as shown in Figure 91.

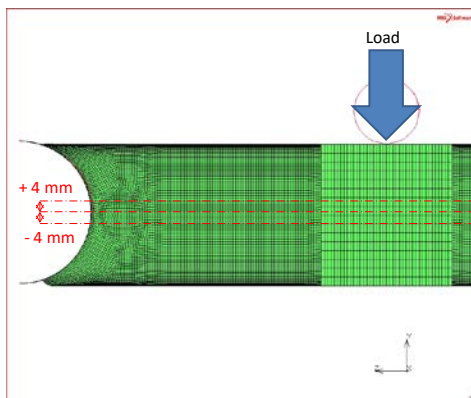


Figure 91 – Brace-chord misalignment.

The maximum stresses along the saddle path are reported in Figure 92 with relevant interpolating curves. In particular the stress intensification is enhanced for misalignments at the extrados (+) where chord is much more forced while the brace is unloaded (Table 36). On the contrary for misalignments at the intrados the chord is unloaded while the fatigue critical location seems to be more likely at the brace-saddle location (Figure 92).

Table 36 – SCF at the chord saddle position: influence of brace-chord misalignments.

Brace-chord misalignment [mm]	0	+ 4 mm	+ 2 mm	- 2 mm	- 4 mm
SCF at chord-saddle position	1.43	2.00	1.65	1.21	0.81

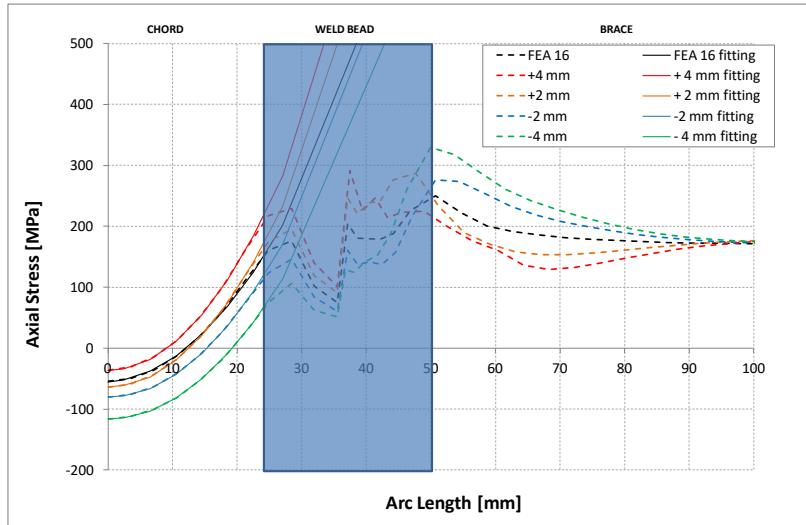


Figure 92 - Axial stress along the chord-saddle-brace position path.

WP7 – IMPACT OF MODULARITY AND QUALITY/COST ANALYSIS

OBJECTIVES AND MAIN OUTCOMES

The aim of this WP is to:

- Evaluate the impact on execution method of the prefabrication process
- Cost analysis of the modular jacket concept.

TASK 7.1 METHOD OF EXECUTION

Since prefabrication can impact differently depending on the assembly stage and phases the knowledge of different assembly steps and accordingly cost splitting is needed.

Two assembly procedures have been considered (Figure 93):

- Horizontal Point-to-point: They assemble one panel (two legs with all their braces). Then they assemble the other, and both parts are raised and assembled one each other.
- Modular by height: prefabricated nodes are available, including "x-type" and then they proceed to assemble it as much as they can in the workshop "by heights".



Figure 93 – Jacket assembly methods: (left) Horizontal-point-to-point; (right) Modular by height.

HORIZONTAL JACKET

Through this methodology, the JACKET is manufactured completely, in one piece, in horizontal position.

The assembly begins with the manufacture of the individual components of the Jacket:

-LEG: The tubes are manufactured independently, from sheet previously curved and welded longitudinally. Several sections of tube may be necessary to create the LEG, joined together by circumferential welding. Welding turning rolls and column & boom welding machines are used and the most commonly used welding method is the submerged arc.

-JOINT and CROSS: It is a complex geometry to be welded and manipulated by a robot.

The assembly sequence will be the following:

- Manufacturing of the complete legs of the Jacket. They include the DK-joints.
- Manufacturing of the main diagonals BRACES. They include the X-joints
- Placing and aligning of the complete legs in a template. Precision measurement of opposite connections.
- Placing and welding of the main diagonals of the BRACES.
- Placing and welding of the secondary diagonals of the BRACES.



Figure 94 - Manufacturing of a side of the JACKET.

For a 4 LEGS Jacket, the above operations must be repeated 2 times.
Next, the lateral auxiliary structures are placed.

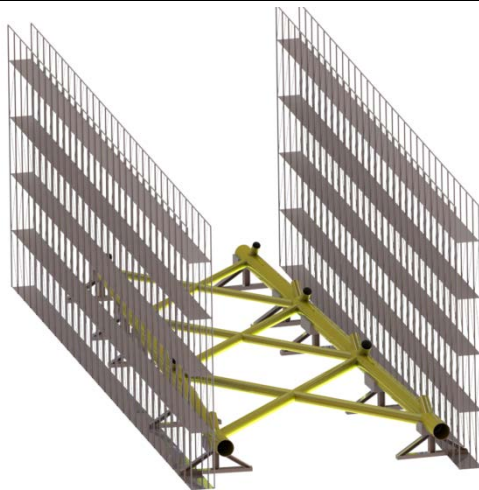


Figure 95 - Placing the lateral auxiliary structures.

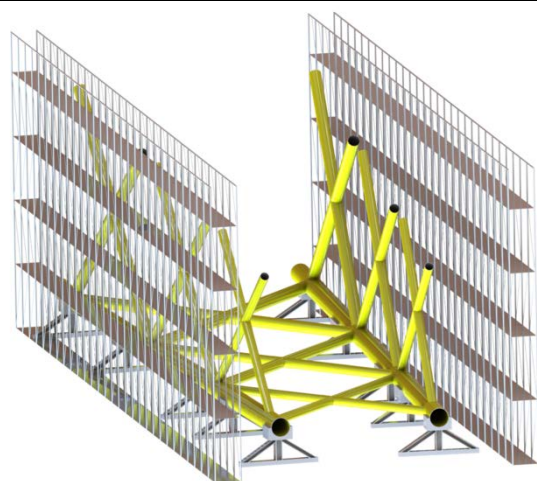


Figure 96 - Placing and welding of the lateral sides.

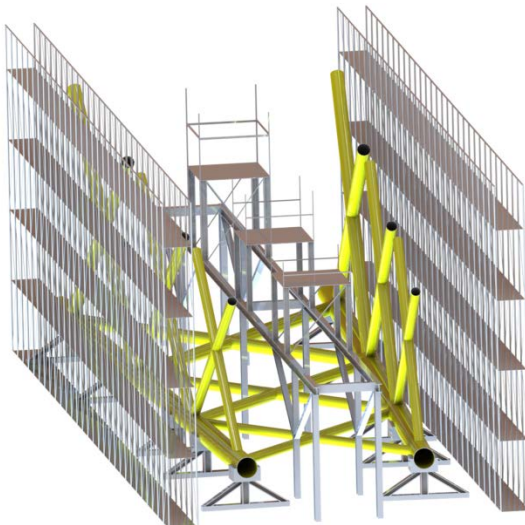


Figure 97 - Placing auxiliary structure for assembling upper side.

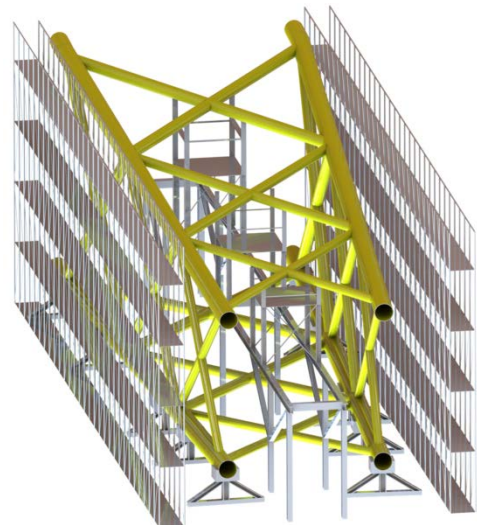


Figure 98 - Placing and welding of the upper side of the Jacket.

The lateral BRACES are manufactured in another area of the workshop and then assembled. The side structures are used as a template. For placing of the upper side, it is necessary to place an auxiliary structure.

VERTICAL JACKET METHODOLOGY

Through this methodology, the JACKET is manufactured in several bodies (FLOORs) independently, which are finally joined together vertically. The number of FLOORs depends on the number of diagonals of the Jacket.

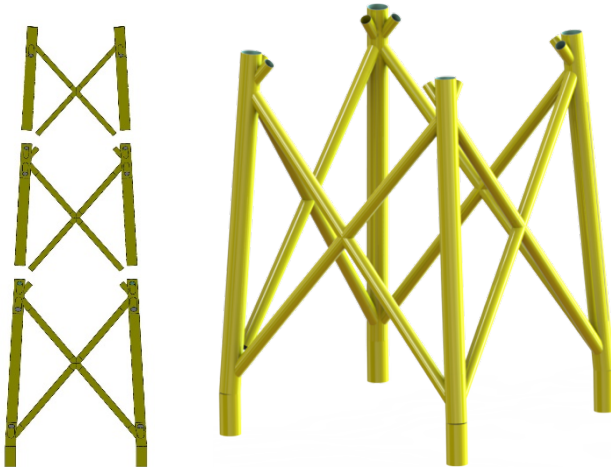


Figure 99 - FLOORS.

In the same way as in the horizontal methodology, the assembly begins with the manufacture of the basic components of the FLOOR: LEGs, JOINTs and CROSSes.

The tubes are manufactured independently, from sheet previously curved and welded longitudinally. Several sections of tube may be necessary to create the LEG, joined together by circumferential welding. Welding turning rolls and column & boom welding machines are used and the most commonly used welding method is the submerged arc. -JOINT and CROSS: It is a complex geometry to be welded and manipulated by a robot.

Once the components are manufactured, the horizontal assembly of each FLOOR of the JACKET begins. To do this, a template is used to maintain the alignment and the precision measurement of opposite connections.

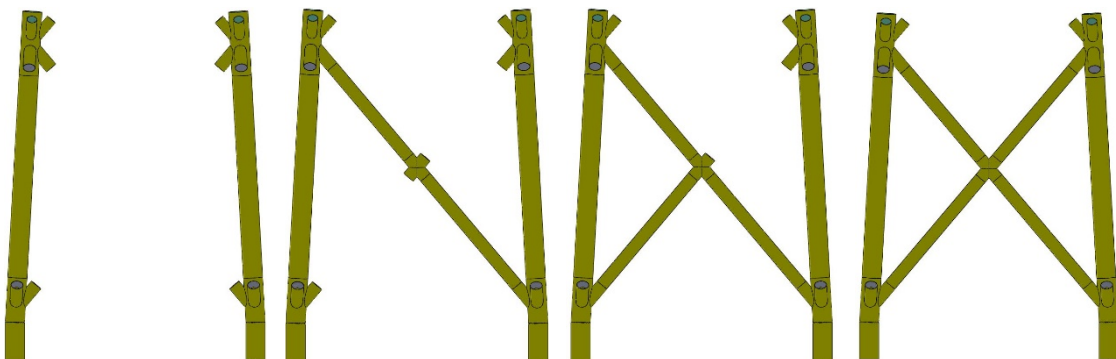


Figure 100 - Manufacturing sequence of a side of the FLOOR.



Figure 101 - One side of the FLOOR.

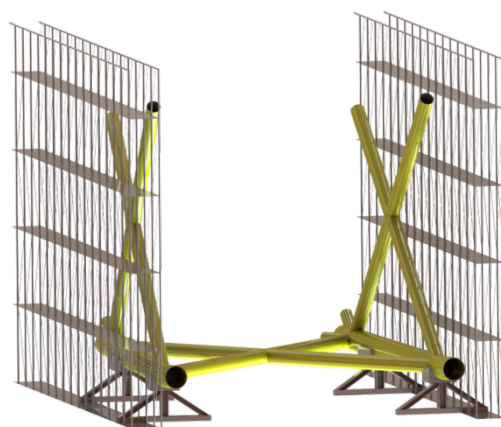


Figure 102 - FLOOR Assembly.

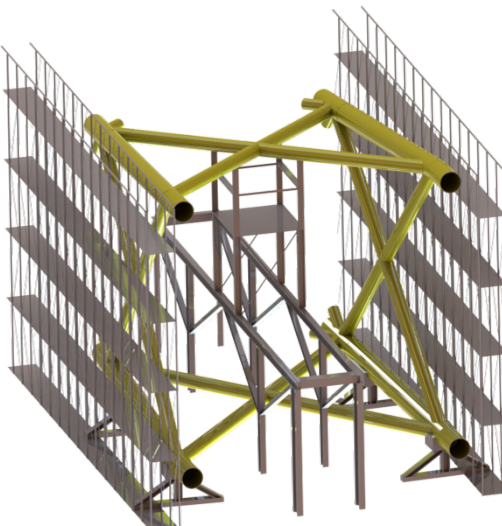


Figure 103 - FLOOR Assembly.

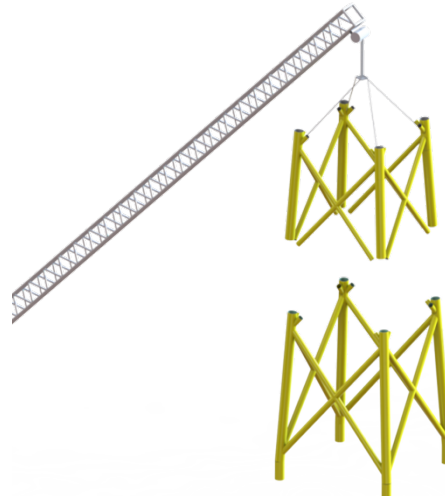


Figure 104 - Lifting up the finished jacket floor.

The SIDES of the FLOORS are manufactured individually of the BRACES, to finally join them together. This assembly can be horizontal, similar to the horizontal methodology explained in the previous section, or vertically. In both cases it is necessary to use an auxiliary structure, to maintain the alignment between the SIDES and BRACES.

Finally, the different JACKET FLOORs are lift to be welded and assembled together. The final result is the Jacket.

TASK 7.2 MODULARITY CONCEPT DEVELOPMENT

COST ANALYSIS MODEL

With the aim of comaprting costs and time of different welding processes and automation levels the actual parameters recorded during welding process are implemented in a cost model.

There are in the literature different approaches for the prediction of the costs in the manufacture of welded joints, according to the most varied standard (e.g. DNV, AWS, ... CWB) and substantially equivalent in results. In this project we are going to apply the AWS method (American Welding Society) widely used for welding processes and highly cosolidated one [3].

To obtain a correct estimate of the costs of the production of a welded steelwork it is necessary to know the best possible about process variables. In aprticular the most importatnt variables to make a correct cost analysis are:

- Labor Cost
- Material Cost
- Overhead Cost

LABOR COST

In order to estimate the labor cost is necessary to know the timing of the various steps that make up the welding activity. The analysis of the working cost is therefore closely linked to the knowledge of the following fabrication phases:

- **Arc Time:** this value is function on many independent process variables, such as welding system, electrical parameters, speed and welding position, type of consumable, geometry of the joint bevel, etc.
- **Handling Time:** summarizes all the work for moving, positioning, grip the piece before and / or during welding including the transport of the steelwork in the final location.
- **Miscellaneous work-place Time:** In this group are included all non-repetitive tasks, but the impact on cost and not easily loadable on the specific contract. For example, the application of anti-spatter, of welding wedge (run-in and/or run-out), the backward support material.

In order to make practical and slim the calculation of labor costs, the three items above mentioned are summarized in a variable practice called "Operator Factor" also called "Duty Cycle". It is defined as the percentage of arc "on" referring to a chosen unit of time. The larger this value, the greater the amount of filler metal melted in the joint with a consequent increase in efficiency of welding operations. Any operation other than direct welding, as the mounting of the piece, its pre, final or intermediate cleaning, tack welding etc...will result in a lowering of the Duty Cycle. In literature there are several tables that summarize the values of such parameter as a function of the welding process, e.g. in Table 37 AWS values are reported. Unfortunately, the field of the "Operator Factor" values is quite wide; it is therefore necessary a knowledge of the production process as accurate as possible.

<i>Method of welding</i>	<i>Operator factor range [percent]</i>
MANUAL	5-30
SEMITAUTOMATIC	10-60
MACHINE	40-90
AUTOMATIC	50-95

Table 37 - "Operator Factor" for some techniques (AWS WHB-5)

Table 38 - Labor Cost for "single-pass" and "multi-pass" in manual or mechanized execution (AWS WHB-5)

SINGLE-PASS	MULTI-PASS
$LC = \frac{0.2 \cdot PR}{TS \cdot OF}$	$LC = \frac{PR \cdot DM}{DR \cdot OF}$
Where: LC = labor cost, [€/m] PR = pay rate, [€/h] TS = travel speed [m/min] OF = operator factor, [percent]	Where: LC = labor cost, [€/m] PR = pay rate, [€/h] DM = deposited metal [kg/m] DR = deposition rate [kg/h] OF = operator factor, [percent]

MATERIAL COSTS

This category is relevant to all the materials used to perform the welding, such as electrodes, wires, flux. The filler material is the one that has much more importance from the cost analysis point of view. The basis of the calculation of the filler metal cost starts from the knowledge of the shape of the joint bevel, and then the cross section from which simple geometric calculations are derived.

Below the calculation scheme proposed by AWS to get to the estimation of the cost for the filler material as a function of the unit of length. Among the different ways for calculating the cost of the filler material we choose the one based on cost per unit length of weld bead performed, in particular:

$$CF = \frac{FP \cdot FC}{DE}$$

Where:

CF = filler metal cost [€/m]

FP = filler metal price [€/kg]

FC = filler metal consumption [kg/m]

DE = deposition efficiency [percent]

Remembering that the weight of the metal actually deposited is a function of the deposition efficiency and typical ranges for the different filler metals are reported below:

FILLER METAL FORM	DEPOSITION EFFICIENCY [PERCENT]
Covered electrodes	55 to 75
Bare solid wire	95 to 99
Flux cored electrodes	80 to 85

Table 39 - Deposition efficiency for different processes (AWS WHB-5)

JOINTS DESCRIPTION

Two (2) different joint configuration have been deeply analysed (Figure 105):

- Girth joint: the pipe-to-pipe butt joint
- X-joint: the intersection at 90° of two braces of similar cross section

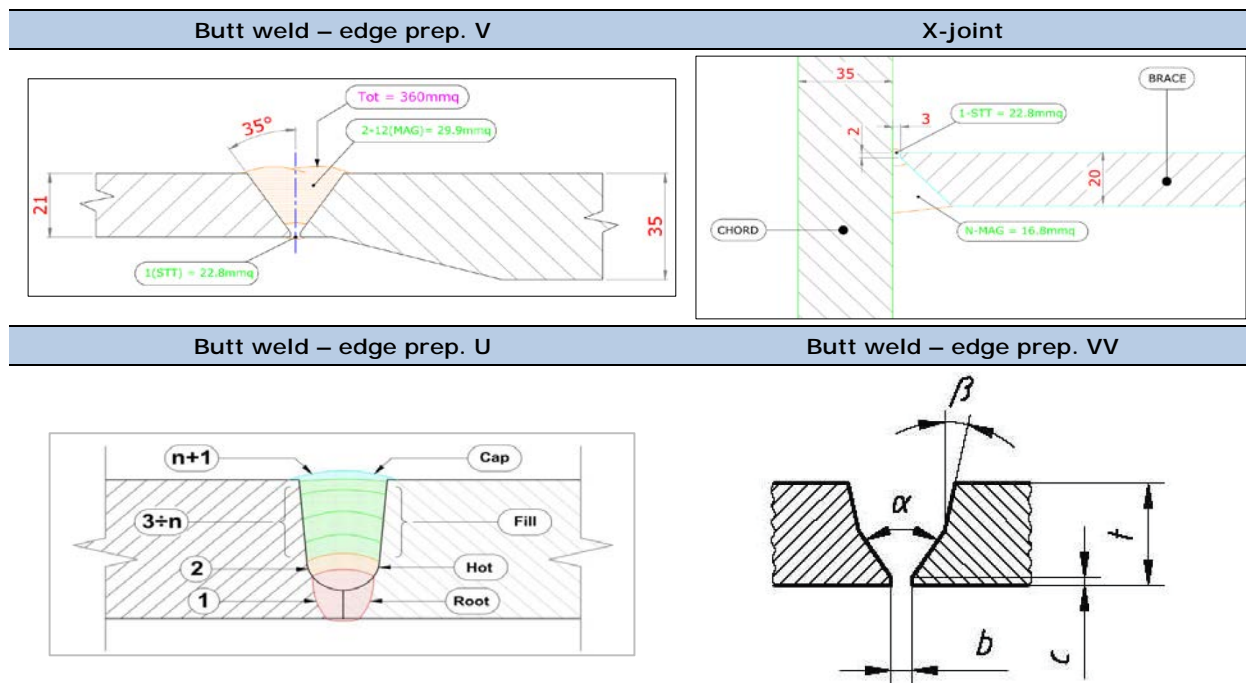


Figure 105 -General joint detail.

The costs and process parameters adopted are reported in Table 40 and Table 41 respectively.

Table 40 – Cost/process parameters for butt joint.

PROCESS		FA-MAG	SA-MAG	FA-MAG	Laser Hybrid
Edge preparation		V	V	U	VV
PR	Pay rate	€/h	30	30	30
OF	Operator factor	0 ÷ 1	0.8 MAG*	0.6 MAG	0.8 0.9 LBW+MAG 0.8 MAG
DR	Deposition Rate	kg/h	1.25 STT 4.3 MAG	1.25 STT 3.3 MAG	2.3 RMD 3.6 MAG 6.2 LBW+MAG 4.7 MAG
FP (FCAW)	Filler Price	€/kg	7	7	7
FP (MAG)	Filler Price	€/kg	2.5	2.5	2.5
FLP	Flux Price	€/kg	4	4	4
GP	Gas Price	€/Nm ³	3	C18	C18/Ar C18/Ar
FR	Flow Rate	l/min	20	20	20

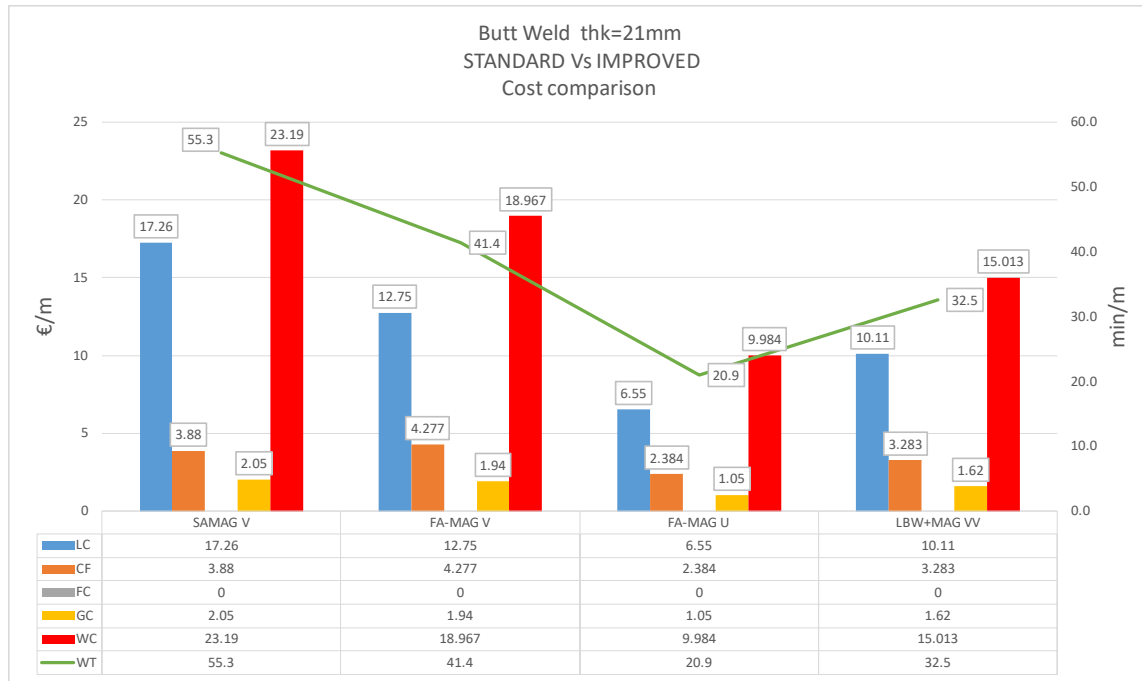
FA Fully automated
 SA Semi automated
 RMD Miller's new Regulated Metal Deposition (RMD™) MIG welding process (modified short-circuit MIG) improves welding quality and productivity
 STT Surface Tension Transfer (STT) welding is a GMAW, controlled short circuit transfer process developed and patented by The Lincoln Electric Company. STT process uses high frequency inverter technology to produce high-quality weld with less spatter and smoke. STT process makes it possible to complete open root welds three or four times faster than GTAW, with low heat input and no lack of fusion

Table 41 – Cost/process parameters for tubular X-joint.

PROCESS		Unit	SA-MAG	FA-MAG
PR	Pay rate	€/h	30	30
OF	Operator factor	0 ÷ 1	0.6 MAG	0.8 MAG*
DR	Deposition Rate	kg/h	1.25 STT 3.3 MAG	1.25 STT 4.3 MAG*
FP (FCAW)	Filler Price	€/kg	7	7
FP (MAG)	Filler Price	€/kg	2.5	2.5
FLP	Flux Price	€/kg	4	4
GP	Gas Price (C18)	€/Nm ³	3	3
FR	Flow Rate	l/min	20	20

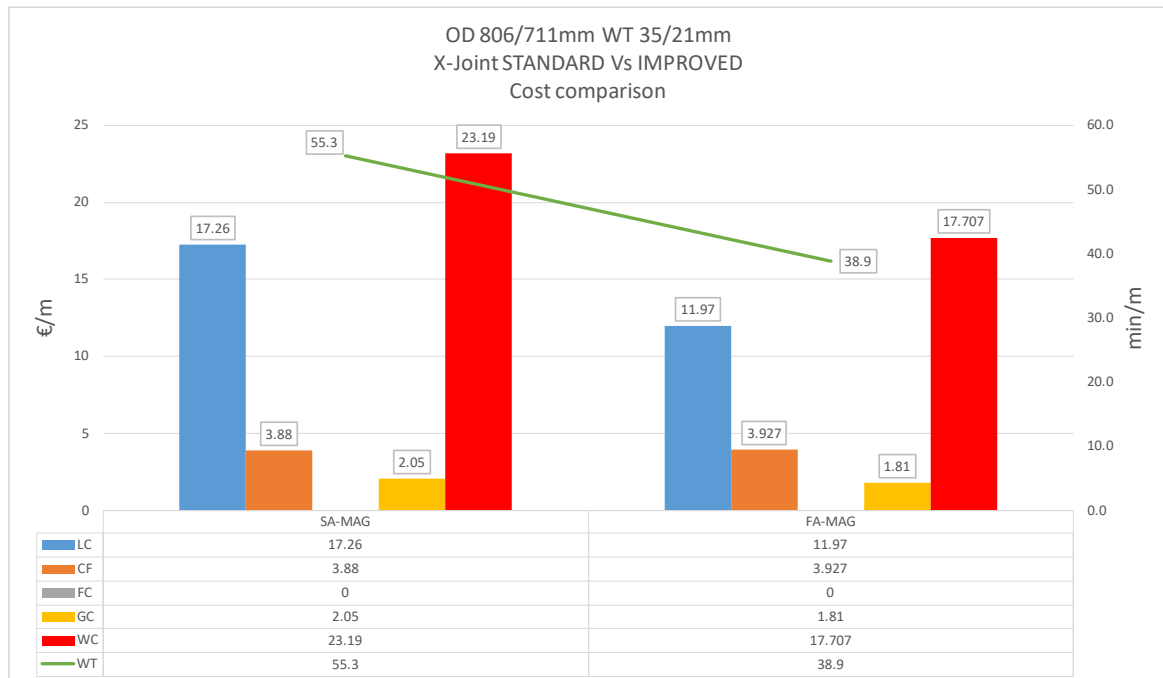
RMD Regulated metal deposition welding process
 STT Surface tension transfer welding process

A detailed cost and time evaluation for the different voices have been performed. The process parameters (Ampere, Voltage, Operator Factor, Deposition Rate) recorded during welding trials of Task 4.4 have been also applied. The results are summarized in Figure 106 and Figure 107 for butt joint and X-joint respectively.



LC: Labor Cost; CF: Filler metal Cost; FC: Flux Cost; GC: Gas Cost; WC: Weld Cost; WT: Weld Time

Figure 106 – Cost and time comparison for tubular butt joint with different welding processes.



LC: Labor Cost; CF: Filler metal Cost; FC: Flux Cost; GC: Gas Cost; WC: Weld Cost; WT: Weld Time

Figure 107 – Cost and time comparison for tubular X-joint with different welding processes.

In particular:

- tubular X-joint a reduction of 24% in total costs and 30% in welding time is estimated applying a fully automated MAG process;
- tubular butt joint for which different process improvements are considered the average savings are reported in the following:

PROCESS	FA-MAG V edge prepar	FA-MAG U edge prepar	LBW+MAG VV edge prepar
Cost reduction	-18%	-57%	-35%
Time reduction	-25%	-62%	-41%

TASK 7.3 INTEGRATION OF STRUCTURAL COMPONENT IN A QUALITY/COST AND OPTIMIZATION ANALYSIS

The costs of the different components of jacket fabrication are evaluated and parameterized, in a sequential way, starting with the reception of the material, bending and welding of a primary tubes, crosses, assembly of the different panels, until getting the final structure.

The assembly steps identified by the analysis in Task 7.1 are considered, in particular:

- 1- Fabrication of CHSs: plates bending and welding to obtain Circular Hollow Sections of needed geometry
- 2- Subsets: assembly of different CHSs to obtain legs and X braces
- 3- Subset assembly: assembly of legs and X braces to obtain jacket

Using a spreadsheet the different parameters involved in the manufacturing process have been implemented: plate bending operations, welding parameters, type of joints, handling and transport times, as well as the associated costs, and depending on the different jacket designs; 3-4 legs, number of floors, etc. The result is a tool that allows to obtain the cost of a jacket based on its design and manufacturing methodology.

The developed tool allows to calculate the manufacturing cost of a jacket according to its design, manufacturing technologies and assembly strategies.

In the followings the main parameters applied in the cost analysis are described and quantified for the different fabrication steps considered.

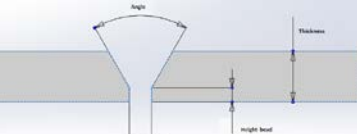
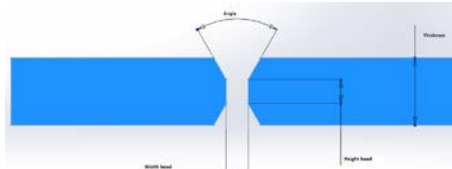
COST AND TIME PARAMETERS

SUPPLY SHEET: The information of the supply plate is inserted containing: length, width and curved maximum width.

Steel plates (S355 grade) cost [€/kg]	Length [mm]	Width [mm]	Maximum Bending radius [mm]
1.00	12000	3000	12000

EDGE PREPARATION: In Table 42 two different edge preparations are detailed. In the analysis reported the default edge preparation is the V one.

Table 42 – Types of edge preparations.

 	Heel width [mm]	Heel height [mm]	Angle [°]	Welding over thickness [%]
	Heel width [mm]	Heel height [mm]	Angle [°]	Welding over thickness [%]
	4	1	60	5%
	4	1	45	5%

In Table 43 the additional time, average cost of labour, machining speed, expressed as percentage, euros and kg / h, respectively.

Table 43 – Machining data.

Extra Time [%]	Average cost of machining [€/h]	Machining speed [Kg/h]
30%	42	10

PLATE BENDING: In Table 44 depending on the CHS geometry the following timings are detailed: positioning of ferrule, placing overhead cranes, preheating, coupling, finishing and cleaning, all of them expressed in minutes. By means of an interpolation within the previous values, the duration each CHS requires for each of these operations is determined. Labour cost considered is 42.00 €/h.

Table 44 – Bending times.

t\D (thickness\diameter)	Item positioning [min]		Bending rolls positioning [min]		Preheat [min]		Hitch [min]		Finish and clean [min]	
	2500	3000	2500	3000	2500	3000	2500	3000	2500	3000
20	15	15	24	28	34	41	46	46	33	40
25	15	15	24	28	37	45	52	52	37	45
30	15	15	24	28	41	49	58	58	41	50
40	15	15	24	28	48	57	70	70	50	60
50	15	15	24	28	55	66	81	81	52	60
60	15	15	24	28	61	74	93	93	58	65

WELDING PROCESS COSTS: The following welding processes have been implemented:

- LSAW, for longitudinal welding and fabrication of CHSs (Table 46 and Table 47)
- MAG semi-automatic (Table 48)
- MAG fully-automatic (Table 48)

The average processes data are considered as reported in the following tables. For the calculation of welding times, in Table 47 the average values of the deposition rate (actual Deposition Rate x Operator Factor) expressed in kg/h depending on the type of process are reported.

Table 45 –Preparation of items inside workshop before welding.

	longitudinal welding [h]	circumferential welding [h]
Item positioning	0.5	6
Fit up	2	4
Cleaning areas to be welded	0.5	1
Removal of welding points	1	3
Transfer intermediate warehouse welded ferrules	1	3
TOTAL [h]	5	17

Table 46 – LSAW cost parameters for CHS fabrication.

Weld material productivity [%]	Flux/weld material ratio	Weld material cost [€/Kg]	Flux material cost [€/Kg]	Labour welding [€/h]
95%	1.5	1.6	1.5	42.00

Table 47 – LSAW deposition rates.

Thickness [mm]	LSAW [kg/h]	SA-MAG [kg/h]	FA-MAG [kg/h]
21	3.04		
25	3.42		
30	3.93		
35	4.31	1.02	3.44
45	4.86		
51	5		
54	5		

Table 48 –MAG/FCAW cost parameters

PROCESS	Weld product [%]	Gas/weld ratio [Kg/Kg]	Weld material cost [€/Kg]	Gas cost [€/Kg]	Labour welding [€/h]	Program Cost [€/geom.]	Deposition rate [kg/h]
Semi automatic MAG	95%	1	1.5*	1.61**	42.00	0	1.02
Fully automatic MAG	95%	1	1.5*	1.61**	42.00	3.000,00	3.05

* ERZO70 S6
** 92%Ar 8%CO₂

STOCKPILING: In this section the timing of the handling and moving during are detailed. The transport at plate material receiving ad during bending operations are estimated 3 hours. Handling/moving times for items are estimate depending on the item dimensions (Table 49). Labour cost considered is 42.00 €/h.

Table 49 - Handling by cranes [minutes]

Weight [kg]						
	1000	5000	9000	13000	17000	21000
Length [mm]	2000	100	110	120	130	140
	7000	160	170	180	190	200
	12000	220	230	240	250	260

INSPECTIONING: An approximate duration is established for the verification of the steel plates before CHS fabrication (10 minutes per plate).

Table 50 contains the types of non-destructive tests (NDT) with which the welded components are inspected. In this case, it is assumed that the NDT to be performed is penetrating liquids, so the parameter that reflects the table is the speed of application of this method in mm / s.

Table 50 – Nondestructive tests on welds.

NDT 1 (Penetrating liquids)	Labor cost inspection [€/h]
Application speed [mm/s]	
10	42

COST AND TIME EVALUATION

The above cost parameters have been used to calculate the total cost of jacket manufacturing, as well as compare to cost benefit in the application of fully automatic processes (FA) with respect to semi automatic one (SA).

The overall results of the comparison are presented in Figure 108 and Figure 109 for the different jacket geometries analyzed. The fabrication costs and times are shared per construction phase, from the base material procurement to the final assembly.

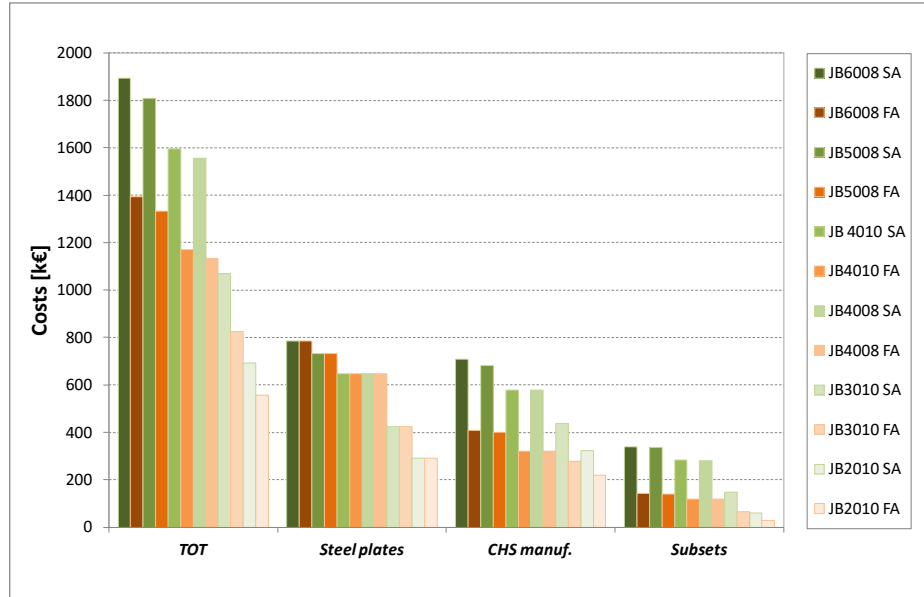


Figure 108 - Summary of costs for the different execution phases.

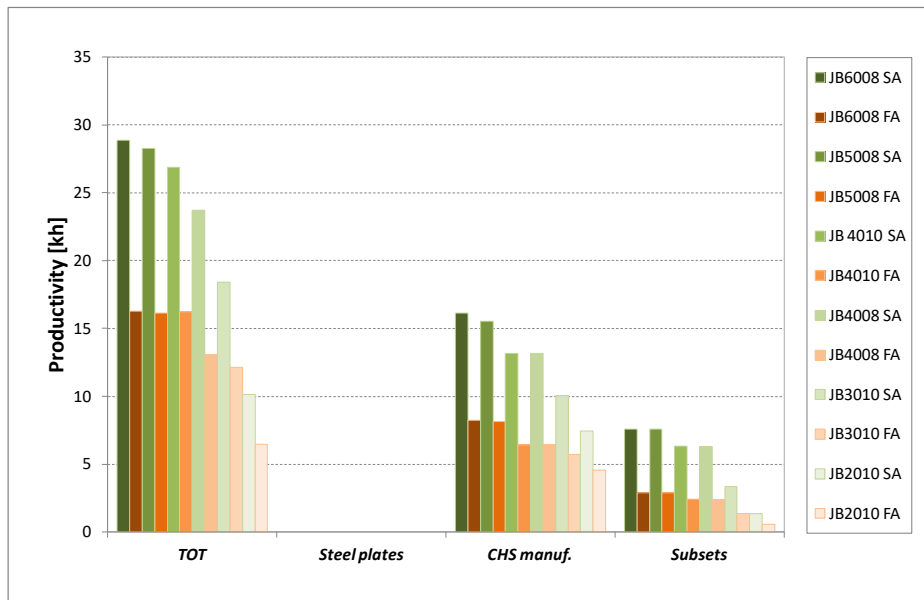


Figure 109 - Summary of times for the different execution phases.

Large part of the evaluated costs are due to the steel plates procuring (between 35% and 51%).

The activities related to the fabrication of tubular elements (Circular Hollow Sections CHS manufacturing) are detailed in Figure 110, comparing semi automatic MAG with longitudinal SAW processes. The automated process LSAW despite the higher consumables cost has so much higher deposition rate that the associated labor cost and manufacturing time are lowered. A total savings of about 36-46% in costs and 39-51% in times is evaluated for this phase

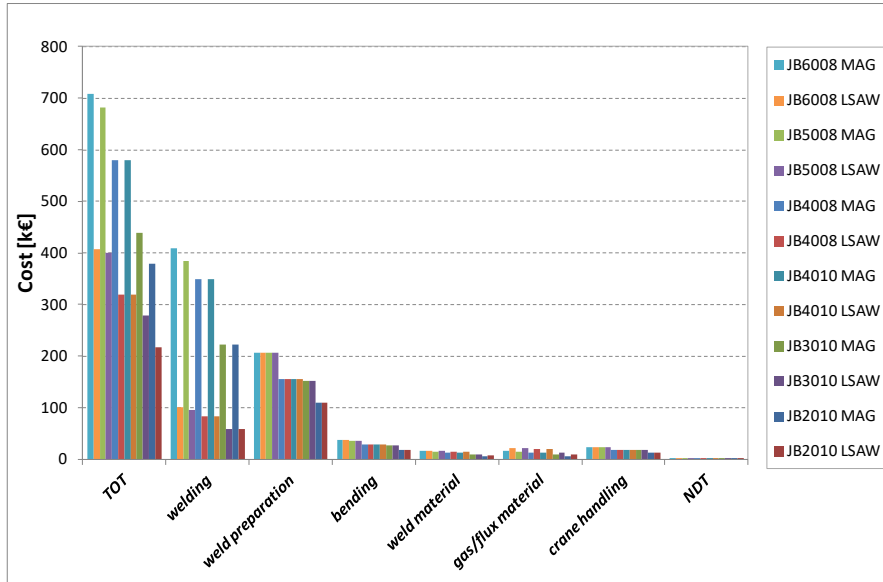


Figure 110 – CHS manufacturing costs.

The prefabricated X-joints as well as orbital mechanized girth welding are implemented at the Subsets assembly stage as detailed in Figure 111. The higher deposition rate of fully automatic/mechanized welding is responsible for its higher productivity evaluated between 56% and 61% of cost reduction and between 57% and 62% of time reductions.

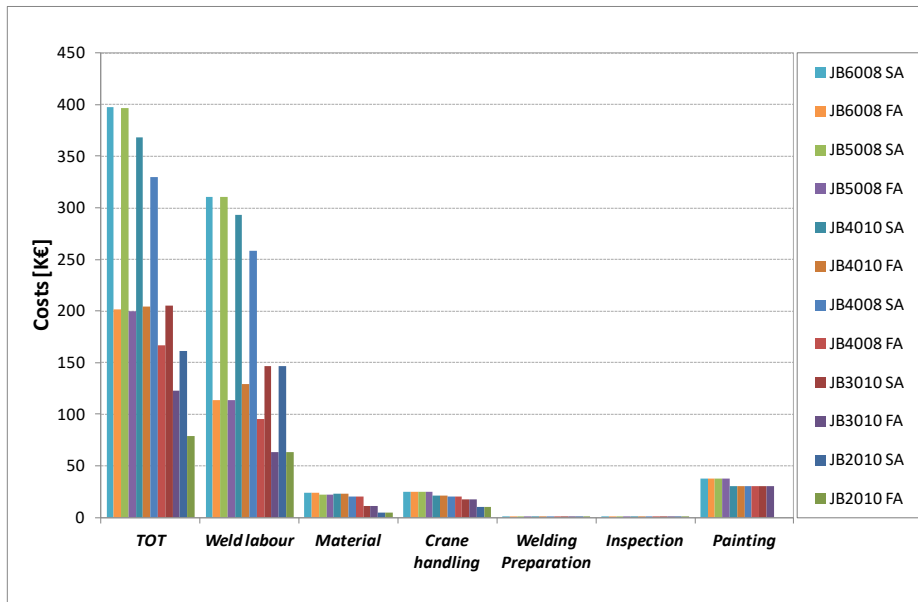


Figure 111 – SUBSETS fabrication costs.

WP8 – DEVELOPMENT OF JABACO MANUAL AND DISSEMINATION OF RESULTS

OBJECTIVES

The main objective of this WP8 is to disseminate results obtained via:

- The development of a Jabaco manual for the Modula Jacket concept (Task 8.1)
- The dissemination of the project achievements by the organization of dedicated workshop (Task 8.2)

TASK 8.1 DEVELOPMENT OF JABACO MANUAL

A free web access database (www.jabaco.it) containing main data developed during the project and potentially useful to the steel industry to develop prefabricated components for offshore wind jackets. In particular it comprises:

- Configuration of the jacket for the 6 different case studied
- Environmental load from the different locations
- In-service stress histories relevant to each of the 6 case studied
- Drawings of standard components developed
- Fine tuning of stress concentration factors
- Allowable fatigue life of standard components
- Fabrication costs for the different case studied

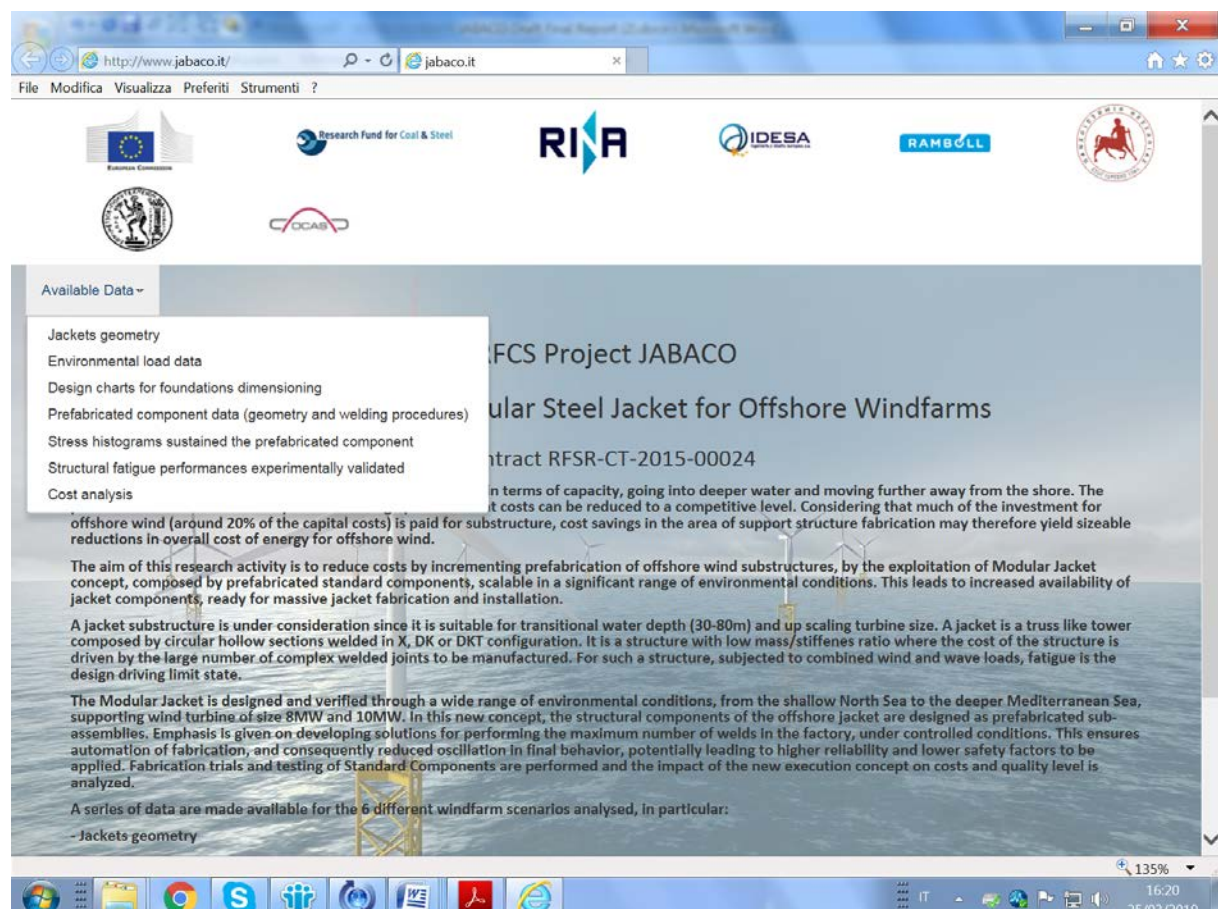


Figure 112 – The front page of Jabaco web site with choice of available data.

TASK 8.2 DISSEMINATION OF RESULTS – DEDICATED WORKSHOP

REPORT FROM GENOA SEMINAR

The seminar was held on 1 October at RINA main office in via Corsica 12, Genoa. It was organised in connection with the Steelmaster 2018 event (<https://www.rina.org/it/media/events/2018/10/01/steelmaster>). With the aim of widen the attending participation the event was supported by the Genoa Engineers Association by the release of 6 CFPs (professional education credits). The seminar flyer and programme is shown in Figure 113.

Seminar

RFCS Project JABACO

Development of Modular Steel Jacket for Offshore Windfarms

Contract RFCSR-CT-2015-00024

1st of October
RINA, via Corsica 12, Genoa, Italy

SEMINAR JABACO

DEVELOPMENT OF MODULAR STEEL JACKET FOR OFFSHORE WINDFARMS

The seminar in Genoa on 1st of October 2018, is dedicated to the presentation of the European project Jabaco, which promotes the development of prefabricated steel jacket for offshore wind farms.

The aim of this project is to reduce offshore wind costs by incrementing prefabrication of substructures, via the development of prefabricated standard components, scalable in a significant range of environmental conditions. This lead to increased availability of jacket components, ready for massive fabrication and installation.

In this new concept, the structural components of the offshore jacket are designed as prefabricated sub-assemblies. Emphasis is given on developing solutions for performing the maximum number of welds in the factory, under controlled conditions. This ensures automation of fabrication, and consequently reduced oscillation in final behaviour potentially leading to higher reliability and lower safety factors to be applied.

The seminar will focus on the results of

- loads analysis at different windfarm locations
- welding trials of prefabricated jacket components with application of fully automated processes
- validation of structural performances via full scale experimental testing
- Cost analysis of the modular jacket concept

The Jabaco Workshop is promoted by Steelmaster 2018, XXII Edition, organized by RINA with the support of ESTEP (European Steel Technology Platform), Federaciel and Ordine degli Ingegneri di Genova.

CONSORTIUM

Coordinator
RINA, Italy

Partners
Ramboll GmbH (Ramboll), Germany
National Technical University of Athens (NTUA), Greece
Ingeniería y Diseño Europeo S.A. (IDESA), Spain
OCAS NV (OCAS), Belgium
University of Thessaly (UTH), Greece

AGENDA

08:30 - 09:15 Registration of participants

09:15 - 09:30 Welcome and Introduction
Guido Chiappa, CEO of RINA-Centro Sviluppo Materiali
Maurizio Michellini, President of Ordine degli Ingegneri della provincia di Genova

09:30 - 10:00 Introduction and project overview: modular Jacket concept
Giuliana Zilli, RINA, Italy

10:00 - 10:30 Wind offshore: state of the art and perspectives of prefabrication
Marc Vollbeck, Ramboll GmbH, Germany

10:30 - 11:00 Met-Ocean Data: relevance to windfarm design
Aero-fluid dynamic analysis of offshore wind turbine
Spyros A. Mavrikos, Dimitris Manolas, National Technical University of Athens, Greece

11:00 - 11:30 Coffee break

11:30 - 12:15 Fatigue of Welded Tubular X-Joints Under In-Plane Bending Loading
Design & Analysis of Seabed Foundation in Structural Systems for Offshore Wind Energy Production
Spyros A. Karamanos, Railis S. Kourkoulis, University of Thessaly, Greece

12:15 - 13:00 Testing of offshore prefabricated joints and development of design recommendations
Philippe Thibaux, OCAS NV, Belgium
(RINA), Italy, tbc

13:00 - 13:30 Fabrication of offshore jacket structures. Automation of welding processes and Cost/Benefits impact.
Ingeniería y Diseño Europeo S.A. (IDESA), Spain, tbc
Marco Monti (RINA), Italy

13:00 - 13:30 Discussion

REGISTRATION

Registration can be made online on the Rina.org website or through the application form which can be downloaded from the site and sent to: steelmaster@rina.org.

Participation is free of charge. However, available seats are limited, so early registration is recommended.

The Jabaco seminar is organized in collaboration with the Order of Engineers of the Province of Genoa. Participation in the Jabaco seminar provides for the release of 6 CFPs.

CONTACTS

For any information you can contact steelmaster@rina.org or mob. +39 335 668247



Figure 113 - Publicity and program for the Genoa seminar.

The seminar was publicised in the following way:

- The seminar was awarded professional training credits from the Engineering Society and was been advertised in its website and
 - E-mail invitation has been sent to the RINA mailing list of steel producers and steelworkers companies
 - Linkedin and Twitter

Ninety-one (91) people attended the seminar, delegates were made up of:

- 71 industrials (steel producers and steelworkers)
 - 9 students or academics from universities
 - 6 delegates from promotion associations
 - 5 consultant engineers

Figure 114 shows the delegates at the seminar.

In Figure 115 the Jabaco team at work after the seminar.



Figure 114 - Genoa seminar.

Figure 115 - Jabaco partners at work after the seminar.

REPORT FROM EDINBURGH SEMINAR

The seminar was held on 3 December at John McIntyre conference centre of Edinburgh, Scotland. It was organised by University of Thessaly in cooperation with Edinburgh University. The seminar flyer and programme is shown in Figure 116. A website of the seminar have been published at <http://jabaco.uth.gr>.

The figure consists of two side-by-side documents. The left document is a 'JABACO WORKSHOP PROGRAM' for Monday, December 03, 2018, at the John McIntyre Conference Centre, Pollock Halls, Edinburgh, Scotland, UK. It features a photograph of two wind turbines on a yellow jacket foundation. The right document is a 'JABACO WORKSHOP' program for the same date and location. Both documents include sections for 'Tentative Schedule', 'Partners', 'Venue', 'Registration', and 'Contact'. The partners listed include RINA, OnderzoeksCentrum voor de Aanwending van Staal NV (OCAS), University of Thessaly (UTH), Volos, Greece, Ramboll GmbH, Hamburg, Germany, National Technical University of Athens (NTUA), Athens, Greece, and Ingeniería y Diseño Europeo S.A. (IDEESA), Gijón, Spain. The venue is John McIntyre Conference Centre (JMCC). Registration can be made online at jabaco.uth.gr. Participation in the workshop is free.

Figure 116 - Publicity and program for the Edinburgh seminar.

Fifty-six (56) people attended the seminar for the vast majority coming from academic institutions.

Figure 117 shows the delegates at the seminar.

In Figure 118 the Jabaco team after the seminar.



Figure 117 - Edinburgh seminar.



Figure 118 - Jabaco partners after the seminar.

EXPLOITATION AND IMPACT OF RESEARCH RESULTS

PUBLICATIONS AND PATENTS

1. T. Papatheocharis, G. C. Sarvanis, P. C. Perdikaris, S. A. Karamanos, "FATIGUE OF WELDED TUBULAR X-JOINTS IN OFFSHORE WIND PLATFORMS", Proceedings of the ASME 38th Conference on Offshore Mechanics & Arctic Engineering, OMAE2019-95812, Glasgow, Scotland, UK, June 2019.
2. T. Papatheocharis, G. C. Sarvanis, P. C. Perdikaris, S. A. Karamanos, "HIGH-CYCLE FATIGUE PERFORMANCE OF WELDED TUBULAR X-CONNECTIONS", International Journal of Fatigue, Special Issue on Fatigue in Structural Integrity of Offshore Energy Industry, to be submitted, April 2019.
3. G. C. Sarvanis, P. C. Perdikaris, S. A. Karamanos, A. D. Zervaki, G. N. Haidemenopoulos, "Fatigue resistance of welded plate T-joint connections made of mild and high-strength steel", Marine Structures, MAST_2019_123, submitted for publication, March 2019.
4. Kourkoulis R., Gelagoti, F, Georgiou I., Karamanos S., Gazetas G., (2017), "On the adequacy of existing foundation schemes for Offshore Wind Turbines subjected to extreme loading", 36th International Conference on Ocean & Arctic Engineering, OMAE2017-61525, June 25-30, Trondheim, Norway
5. Gelagoti, F., Kourkoulis, R., Georgiou, I., Karamanos, S., (2019), "Soil-Structure Interaction Effects in Offshore Wind Support Structures Under Seismic Loading", JOMAE (accepted for publication).
6. M. Antoniou, F. Gelagoti, R. Kourkoulis, I. Georgiou, S. A. Karamanos, "Seabed foundation of jacket wind-platform", 2nd International Conference on Natural Hazards & Infrastructure, ICONHIC, June 2019, Chania, Crete, Greece.

LIST OF FIGURES

Figure 1 - time series of the electrical power for the step-up load case for the 8MW (left) and 10MW (right) OWT.....	7
Figure 2 - Comparison of simulated equivalent fatigue loads according to DLC1.2 but different environmental conditions....	8
Figure 3 - Recurrence of pipe geometries cumulated for the 6 windfarm scenarios.	8
Figure 4 – Experimental data compared with offshore joints fatigue design curves.....	11
Figure 5 – Experimental data fitting of semi automatic (SA) and fully automatic (FA) welded joints.	11
Figure 6 – Damage Factor calculated for the selected critical locations and impact of automated productions benefits (experimental FA values).....	12
Figure 7 - Summary of costs for the different execution phases.....	13
Figure 8 - Windfarm locations under investigation.	14
Figure 9 - Reference soil for jackets design: average sand profile.....	17
Figure 10 - General wind turbine layout and reaction forces at the tower bottom.	18
Figure 11 - Steady state operational curves showing mean (10min) electrical power, rotor speed and pitch angle over mean (10min) wind speed.....	19
Figure 12 - 8MW turbine model: time series of the electrical power of the wind turbine (left) and the side-to-side bending moment (right).	20
Figure 13 - Time series of the electrical power for the step-up load case for the 10MW DTU RWT mounted on a jacket at 50m water depth. The 2 nd option (ω cut-in=5rpm) slightly increases the produced power in the low speed regime.....	21
Figure 14 - Turbine rotor speed, blade pitch and electrical power over the wind speed. The blue vertical line distinguishes the variable speed part from the variable pitch part	21
Figure 15 - Time series of the tower base side-to-side bending moment for the step-up load case for the 10MW DTU RWT mounted on a jacket at 50m water depth. The 2 nd option (ω cut-in=5rpm) slightly reduces the side-to-side bending moment.	22
Figure 16 - Jacket 20m-10MW including typical appurtenances at location L4.	23
Figure 17 - Recurrence of pipe geometries cumulated for the 6 windfarm scenarios.	23
Figure 18 - Load calculation procedure.	24
Figure 19 - Physical modeling in hGAST.....	25
Figure 20 - Definition of wind and wave directions.....	26
Figure 21 - Beginning of the resulting time series of sectional forces at the connection of beam 5 to the K-joint node 30 of the jacket at location L3 (50 m water depth, North Sea) for load case 117	27
Figure 22 - Beginning of the resulting time series of sectional moments at the connection of beam 5 to the K-joint node 30 of the jacket at location L3 (50 m water depth, North Sea) for load case 117	27
Figure 23 – Hot spot stress histograms relevant to most critical X-joint location per windfarm scenario.	30
Figure 24 – Comparison among different fatigue designS-N curves for offshore tubular connections.	31
Figure 25 – Damage Factors of selected critical locations.....	31
Figure 26 - Numerical Methodology FE Mesh.	32
Figure 27 - Representation on the π -plane of the Mohr-Coulomb yield criterion and the three assumed yield criteria of the kinematic hardening model.....	33
Figure 28 - Numerical Methodology validation against (b) API and (c) centrifuge experiments Rosquoët et al (2004).....	33
Figure 29 - Performance of OWT on Jacket Platform for monotonically increasing values of wind and wave loading. Comparison between ‘Beam-on-Springs’ and coupled 3D FEM: vertical displacements at the leeward and windward legs and jacket rotation.	34
Figure 30. Suction Caisson with L/D=3 : finite element mesh configuration.....	35
Figure 31 - Uplifting resistance of suction Caisson in clays: (a) theoretical bearing mechanisms assuming no-suction and full-suction conditions; (b) numerical modeling: snapshots of plastic deformations; (c) effect of suction conditions on the axial bearing capacity of caissons with L/D=2 for different levels of soil inhomogeneity	36
Figure 32 - Seismic Performance of OWT supported on Jackets : (a) Regional Seismicity in the area of the Wind farm; the L'Aquila input motion and its elastic response spectrum; (b) seismic response of a wind-turbine in operation (loading combination LC: G+W+E) and a wind turbine at rest (LC: G+E); time-history of seismic jacket rotation when the foundation is implemented with piles or suction caissons (LC: G+W+E).....	37
Figure 33 - Example design charts. Reference case: 10 MW turbine, pile foundation (D=2.5m), sandy site with $\phi=30^\circ$	38
Figure 34 - Dimensionless design charts for suction caissons in clays: Dimensionless vertical deformation with respect to the vertical factor of safety at the leeward leg.....	38
Figure 35 - Diagram showing how a plate is formed into a tube.....	41
Figure 36 - FEM simulation process.....	42
Figure 37 - Simulation of possible welding configurations	43
Figure 38 - Triaxial state associated to the welding process with penetration Type 3.....	43
Figure 39 - Sequence of welds for making mockup starting at points.....	44
Figure 40 – Robot Welding (TIG+MAG) of jacket X-joint.	45

Figure 41 - (left) Different regions for the preparation of specimens (right) Application of HFMI on laboratory specimens ..	47
Figure 42 - (a) Operator performing the HFMI treatment (b) specimens treated at IDEFAB	47
Figure 43 - Engineering stress-strain curves	48
Figure 44 - Hole drilling (h-d) and X-ray diffraction (x-r) measurements comparison.....	50
Figure 45 - Hardness measurements on (left) semi-automatic traditional weld and (right) fully-automatic weld.....	50
Figure 46 - Weld bead profiles at saddle (left) and crown (right) location.....	50
Figure 47 - Strain map for the external stress raiser: (a) as welded condition (b) after HFMI treatment	51
Figure 48 - Fatigue specimens after testing (HFMI condition).....	52
Figure 49 – Left: Comparison among different fatigue design S-N curves for offshore tubular connections. Right: Standard deviation applied to S-N curves.....	53
Figure 50 - X-joint as delivered to laboratory.....	54
Figure 51 – Experimental results comparison with standard S-N curve.....	54
Figure 52 – Fatigue crack of test ID 6 and ID 7	55
Figure 53 – Number of cycles at failure for each loading block.....	56
Figure 54 – Variable amplitude fatigue data: comparison with constant amplitude ones and API X' design curve.....	56
Figure 55 – Strain gauge instrumentation and measurements (10 cycles at 76kN maximum load on test ID 5 (FA).....	57
Figure 56 – Joint stiffness evolution during the test	57
Figure 57 – Experimental set-up for in-plane bending fatigue tests.	58
Figure 58 – Experimental results; comparison with DNV RP C203 standard S-N curve.....	58
Figure 59 – Though-thickness crack at specimens J-8 and J-9.....	59
Figure 60 – Strain gauge instrumentation.....	60
Figure 61 – Joint stiffness evolution during the test	61
Figure 62 – Resonant fatigue testing rig.....	61
Figure 63 - Comparison between the S-N curve for tubular joints and the experimental results	62
Figure 64 -Illustration of the shape of the weld and the crack location (sample G).....	62
Figure 65 - Finite element model and boundary conditions.....	64
Figure 66 - Out-of-plane bending vertical displacements.	65
Figure 67 – General view of the numerical model.....	65
Figure 68 – Different views of weld part and experimental material curve used in numerical analysis.	66
Figure 69 - Finite element model of the specimen (showing different paths for stress gradient extraction)	66
Figure 70 - Representation of the different mode shapes.	67
Figure 71 - Expected magnitude of the first principal stress in absolute distribution along the brace at a frequency of 23.08Hz, at two distance from the weld toe (HS1 and HS2) and the resulting hot spot stress value (HS12).....	68
Figure 72 - Expected magnitudes of the hot spot stress on the chord and the brace sides for an elliptic loading	68
Figure 73 - Actual joint geometry.....	68
Figure 74 - Finite element model: without weld geometry (FEA 0)and with weld geometry modelled (FEA 16)	69
Figure 75 - Axial strains (brace direction): model vs. experimental.	69
Figure 76 - Maximum principal stresses in axial brace direction.....	70
Figure 77 – Comparison of experimental and numerical results in terms of load - displacement diagram.	70
Figure 78 – Strain distribution at critical location of the joint.....	71
Figure 79 - First principal stress on tour contour at constant distance from the weld toe (HS1 and HS2) and the extrapolated hot spot stress (HS12), along the brace (top) and the chord (below). Model G6D1, frequency 23.00Hz.	72
Figure 80 - Hot spot first principal stress on from a contour along the weld toe (HS12) for the brace and chord / leg. Left: For the model without weld. Model A2D1, frequency 23.08Hz. Right: For the model without weld. Model A1WD, frequency 23.17Hz.....	72
Figure 81 - First principal stress on tour contour at constant distance from the weld toe (HS1 and HS2) and the extrapolated hot spot stress (HS12), along the brace (top) and the chord (below). Model BD1, frequency 22.83Hz.....	72
Figure 82 - First principal stress on tour contour at constant distance from the weld toe (HS1 and HS2) and the extrapolated hot spot stress (HS12), along the brace (top) and the chord (below). Model FD1, frequency 22.85Hz.	73
Figure 83 - Displacement at the middle of the sample, experimentally and predicted by finite element simulation for the model without weld (left) and for the model with weld (right).	74
Figure 84 - Comparison of the first principal stress close to the weld toe on the brace (left) and on the chord (right) model A2D1 23.08Hz.....	76
Figure 85 - Illustration of a model for the computation of stress concentration factor.....	76
Figure 86 - Location for extraction of the data.....	77
Figure 87 - First principle stress on two contours (HS1 and HS2) at given distance from the intersection between the tubes, and the extrapolated resulting hot spot (HS12) value. Above: values on the brace, below on the chord.	77
Figure 88 - First principal stress for axial loading of case 610-30-21.....	78

Figure 89 - First principal stress for axial loading of case 610-30-21, with the location of the contours for the extrapolation for the hot spot stress.	78
Figure 90 - Evolution of the first principal stress close to the weld toe (0:weld toe).	78
Figure 91 – Brace-chord misalignment.....	79
Figure 92 - Axial stress along the chord-saddle-brace position path.....	80
Figure 93 – Jacket assembly methods: (left) Horizontal-point-to-point; (right) Modular by height.....	82
Figure 94 - Manufacturing of a side of the JACKET.....	83
Figure 95 - Placing the lateral auxiliary structures.	83
Figure 96 - Placing and welding of the lateral sides.	83
Figure 97 - Placing auxiliary structure for assembling upper side.	83
Figure 98 - Placing and welding of the upper side of the Jacket.	83
Figure 99 - FLOORs.	84
Figure 100 - Manufacturing sequence of a side of the FLOOR.	84
Figure 101 - One side of the FLOOR.	85
Figure 102 - FLOOR Assembly.....	85
Figure 103 - FLOOR Assembly.....	85
Figure 104 - Lifting up the finished jacket floor.	85
Figure 105 -General joint detail.....	87
Figure 106 – Cost and time comparison for tubular butt joint with different welding processes.....	89
Figure 107 – Cost and time comparison for tubular X-joint with different welding processes.....	89
Figure 108 - Summary of costs for the different execution phases.....	93
Figure 109 - Summary of times for the different execution phases.....	93
Figure 110 – CHS manufacturing costs.....	94
Figure 111 – SUBSETS fabrication costs.....	94
Figure 112 – The front page of Jabaco web site with choice of available data.	96
Figure 113 - Publicity and program for the Genoa seminar.	97
Figure 114 - Genoa seminar.	98
Figure 115 - Jabaco partners at work after the seminar.....	98
Figure 116 - Publicity and program for the Edinburgh seminar.	99
Figure 117 - Edinburgh seminar.	99
Figure 118 - Jabaco partners after the seminar.....	100

LIST OF TABLES

Table 1 - Overview of offshore locations and turbine size.	7
Table 2 - Actual full-scale testing program (Task 5.2 and 5.3).....	10
Table 3 - Overview of boundary conditions for the 6 considered jackets.	14
Table 4 - Statistical analysis of wind, wave and sea level time series at locations L1-L4.....	15
Table 5 - Design values for significant wave height (m), wind speed (m/s) and spectral peak period (sec) for various return periods (in years) for locations L1-L4	16
Table 6 - Wind turbine geometry, structural and operational parameters based on exemplary hub height of 107m LAT.....	20
Table 7 - General Characteristics of DTU 10MW RWT.....	21
Table 8 - Overview of elevations.	22
Table 9 - Offshore wind jackets X-joints geometries	23
Table 10 - Overview of the considered load cases	26
Table 11 - Met-ocean data for the 3 sites in North Sea for the 10MW WT and average values used in the first analysis.....	28
Table 12 - DLCs definition.....	28
Table 13 - Maximum absolute values of the stresses for each joint-type of the jacket for the 3 water depths	29
Table 14 - Geometrical properties and Ephthymiou coefficients for the X-joints under consideration.....	40
Table 15 – Base material mechanical properties.....	41
Table 16 - Summary of Welding Procedure Specifications.....	42
Table 17 – Jabaco project X-joint mock-ups.	45
Table 18 – X joints welding parameters.	46
Table 19 – Girth joint welding parameters.....	46
Table 20 - Charpy V notch tests.....	49
Table 21 - Compressive stresses and local work hardening (FWHM) induced by HFMI on the HAZ	49
Table 22 - Results obtained after the measurements of stress raisers	50
Table 23 - Results obtained in the fatigue tests	51
Table 24 - Actual full-scale testing program (Task 5.2 and 5.3).....	52
Table 25 - Geometrical properties of the X-joints under consideration.....	53
Table 26 – Tabulated experimental results.	54
Table 27 – Variable amplitude loading blocks	55
Table 28 – SCFs evaluated by strain gauges measurements (chord saddle position).....	57
Table 29 – In-Plane bending experimental results.	59
Table 30 – SCFs evaluated by strain gauges measurements (chord crown position).	60
Table 31 - Overview of computed and measured resonance frequencies	71
Table 32 - Comparison of the experimental strain gauge reading (5 th column) and the finite element simulation (column FEA). The relative difference is indicated in the last column. Simulation for the model without weld (A2D1).....	74
Table 33 - Comparison of the experimental strain gauge reading (5 th column) and the finite element simulation (column FEA). The relative difference is indicated in the last column. Simulation for the model with weld (AWD4).	75
Table 34 - Geometry investigated for the stress concentration factors.....	77
Table 35 - Example of resulting table for the stress concentration factors for the three load cases for 610-30-21	79
Table 36 – SCF at the chord saddle position: influence of brace-chord misalignments.	80
Table 37 - “Operator Factor” for some techniques (AWS WHB-5).....	86
Table 38 - Labor Cost for “single-pass” and “multi-pass” in manual or mechanized execution (AWS WHB-5).....	86
Table 39 - Deposition efficiency for different processes (AWS WHB-5).....	87
Table 40 – Cost/process parameters for butt joint.	88
Table 41 – Cost/process parameters for tubular X-joint.	88
Table 42 – Types of edge preparations.	90
Table 43 – Machining data.	90
Table 44 – Bending times.	91
Table 45 –Preparation of items inside workshop before welding.....	91
Table 46 - LSAW cost parameters for CHS fabrication.....	91
Table 47 – LSAW deposition rates.	92
Table 48 –MAG/FCAW cost parameters.....	92
Table 49 - Handling by cranes [minutes]	92
Table 50 – Nondestructive tests on welds.....	92

LIST OF SYMBOLS AND ACRONYMS

1P	rotor rotation frequency
3P	rotor blade passing frequency
c	Soil parameters: Cohesion of soil
cdf	cumulative distribution function
CF	Weld filler metal cost
CoG	center of gravity
Cp	turbine power coefficient
Cq	turbine torque coefficient
Crbm	turbine out-of-plane moment
Ct	turbine thrust coefficient
CHS	Circular hollow section
CV	Sample coefficient of variation (ratio of the standard deviation to the mean value)
DE	Weld deposition efficiency
DLC	Design load case
DR	Deposition rate
d _c	Bearing capacity: Dimensionless depth factor corresponding to N _c
d _q	Bearing capacity: Dimensionless depth factor corresponding to N _q
d _y	Bearing capacity: Dimensionless depth factor corresponding to N _y
D	Diameter
Dr	Soil parameter relative density
DR	Weld deposition rate
E	Elastic modulus
ECMWF	European Centre for Medium-range Weather Forecasts
f	frequency
FA	Fully automatic fabrication process
FC	Weld filler metal consumption
FCAW	Flux cored arc welding
FEM	Finite element model
FLP	Weld flux price
FP	Weld filler metal price
FR	Weld gas flow rate
Fx	wind tower/jacket intersection load in x direction
Fy	wind tower/jacket intersection load in y direction
Fres	resulting load on the principal direction
G	Shear modulus of soil (in terms of effective stress)
Go	Elastic shear modulus of soil at zero shear strain
GP	Weld gas price
GEV	Generalized Extreme Value
HFMI	High frequency impact treatment
HSS	Hot spot stress
Hx	Load parameters: Horizontal load in x-axis
Hy	Load parameters: Horizontal load in y-axis
H _{m_o}	Significant wave height (m); it is a product of the wave spectrum
I	moment of inertia
IPB	In plane bending
IEC	International Electrotechnical Commission
K	Earth pressure coefficient
K _u	Sample kurtosis parameter: a measure of the peakedness of the underlying distribution relative to the normal distribution.
L	Length
LAT	Seawater level of lowest astronomical tide
m	Location parameter of the Generalized Extreme Value or the log-normal distribution; Sample mean value
m	inverse slope of fatigue curve
MAG	Metal active gas welding process
min	Sample minimum value
max	Sample maximum value
M _x	wind tower/jacket intersection moment with respect to x direction
M _y	wind tower/jacket intersection moment with respect to y direction
M _z	wind tower/jacket intersection moment with respect to z direction
M _{res}	resulting moment on the principal direction
n̄	Sample size
N	Number of cycles
NDT	Nondestructive testing
N _c	Bearing capacity: Cohesion factor
N _q	Bearing capacity: Overburden factor

N_y	Bearing capacity: Self weight factor
OD	Outside diameter
OF	Operator factor
OPB	Out of plane bending
OWT	Offshore wind turbine
pa	Atmospheric pressure
pdf	Probability density function
PR	weld labour pay rate
PT	Penetrant liquid non-destructive testing
q	Soil parameter: Overburden pressure
q_H	Mean wave direction (deg); direction from which the sea-state propagate
q_J	Mean wind direction in deg; direction from which the wind blows
RMD	Regulated metal deposition welding process
R	Radius (for rotor or foundation)
rpm	rotation per minute
RT	Radigrafic nondestructive testing
RWT	Reference Wind Turbine
s	Scale parameter of the Generalized Extreme Value or the Rayleigh or the log-normal distribution; Sample standard deviation
S	Stress range in the logarithmic diagram
SA	Semi automatic fabrication process
SAW	Submerged arc welding process
SCF	Stress concentration factor
SD	Standard Deviation
SNCF	Strain concentration factor
STT	Surface tension transfer welding process
S_c	Bearing capacity: Dimensionless shape factor corresponding to N_c
S_q	Bearing capacity: Dimensionless shape factor corresponding to N_q
S_y	Bearing capacity: Dimensionless shape factor corresponding to N_y
S_u	Soil parameters: Undrained shear strength
Sk	Sample skewness coefficient: a measure of the lack of symmetry of the underlying distribution
t	thickness
T	Torsion moment
TI	Turbulence intensity
TIG	Tungsten inert gas welding
T_p	Spectral peak period (s) corresponding to the peak of the wave spectrum
TP	transition piece, the structural element connecting wind tower to the jacket foundation
u_x	Displacement parameters: Horizontal displacement in x-axis
u_y	Displacement parameters: Horizontal displacement in y-axis
U_w	Wind speed (m/s) at 10 m above sea level
V	wind speed or Vertical load in foundation
w	Vertical displacement
WPS	Welding procedure specifications
w.r.t.	seawater level of lowest astronomical tide (LAT).
WT	Wind turbine
WTG	wind turbine generator
x	Shape parameter of the Generalized Extreme Value distribution
a	Dimensionless exponential factor depending on the soil type
γ	Soil parameters: Unit weight of soil
γ'	Soil parameters: Effective unit weight of soil
δ	Soil parameters: Interface friction angle
θ_x	Displacement parameters: Rotation about x-axis
θ_y	Displacement parameters: Rotation about y-axis
θ_z	Displacement parameters: Rotation about z-axis
ϕ	Soil parameters: Friction angle of soil

REFERENCES

- [1] API(2000) Recommended Practice for Planning, Designing and Constructing Fixed Offshore Platforms-Working Stress Design, API RP-2A. American Petroleum Institute, Washington, USA.
- [2] ASTM E739 Standard Practice for Statistical Analysis of Linear or Linearized Stress-Life (S-N) and Strain-Life (ϵ -N) Fatigue Data.
- [3] AWS WHB-5.7 WELDING HANDBOOK - ENGINEERING, COSTS, QUALITY, AND SAFETY
- [4] BS 7608 Guide to fatigue design and assessment of steel products
- [5] CIDECT No.8 Design Guide for circular and rectangular hollow section welded joints under fatigue loading.
- [6] DNV-OS-J101 – Design of Offshore Wind Turbine Structures. Det Norske Veritas, October 2014.
- [7] DNVGL-RP-C203 Fatigue Design of offshore steel structures. 2016.
- [8] DNV (1992) Classification Notes No. 30.4, Foundations. Det Norske Veritas, Oslo, Norway.
- [9] ERA-20C Project (ECMWF Atmospheric Reanalysis of the 20th Century). Research Data Archive at the National Center for Atmospheric Research, Computational and Information Systems Laboratory. <http://dx.doi.org/10.5065/D6VQ30QG>.
- [10] Germanisher Lloyd WindEnergie(2005). Guideline for the Certification of Offshore Wind Turbines.
- [11] IEC 61400-1 : 2005. Wind Turbines-Part 1: Design Requirements.
- [12] IEC 61400-3 : 2008. Wind Turbines-Part 3: Design Requirements for Offshore Wind Turbines.
- [13] ISO 19902 Petroleum and natural gas industries -- Fixed steel offshore structures
- [14] RINA Rules for the Classification of Steel Fixed Offshore Platforms.
- [15] ABAQUS 6.10. (2010). Standard user's manual. Dassault Systèmes Simulia Corp., Providence, RI, USA.
- [16] MSC. Software MARC 2011. User's Manuals.
- [17] Anastasopoulos, I., Gelagoti, F., Kourkoulis, R. & Gazetas, G. (2012). Simplified Constitutive Model for Simulation of Cyclic Response of Shallow Foundations: Validation against Laboratory Tests, Journal of Geotechnical and Geoenv. Eng., ASCE, 137(12), 1154-1168.
- [18] Baarholm, G.S., Haver, S., Økland, O.D., 2010, "Combining contours of significant wave height and peak period with platform response distributions for predicting design response", Marine Structures, 23(2), pp. 147-163, <http://dx.doi.org/10.1016/j.marstruc.2010.03.001>.
- [19] Bampton M. C. C., Craig R. R.: Coupling of substructures for dynamic analyses; in AIAA Journal, Vol. 6, No. 7, pp. 1313-1319, 1968
- [20] Bak, C., Zahle, F., Bitsche, R., Kim, T., Yde, A., Henriksen, L.C., Natarajan, A., Hansen, M.H., "Description of the DTU 10 MW Reference Wind Turbine," DTU Wind Energy Report-I-0092, 2013.
- [21] Bagherpour T, XM. Li, DI Manolas, VA Riziotis (2018). "Modeling of Material Bend-Twist Coupling on Wind Turbine blades", submitted for publication in Journal of Composite Structures.
- [22] P.K. Chaviaropoulos, (2001), "Flap/Lead-lag Aeroelastic Stability of Wind Turbine Blades", Wind Energy 2001; 4, pp183-200
- [23] Cheng, P. W., van Bussel, G. J. W., van Kuik, G. A. M., Vugts, J. H., 2003, "Reliability-based Design Methods to Determine the Extreme Response Distribution of Offshore Wind Turbines", Wind Energy, 6(1), <http://dx.doi.org/10.1002/we.80>
- [24] Coles, S., 2001, "An Introduction to Statistical Modelling of Extreme Values", 209 p., Springer Series in Statistics
- [25] Efthymiou, M.: Development of SCF Formulae and Generalised Influence Functions for use in Fatigue Analysis. Recent Developments in Tubular Joint Technology, OTJ'88, October 1988, London.
- [26] Gourvenec S., H. E. Acosta-Martinez and M. F. Randolph, (2009), "Experimental study of uplift resistance of shallow skirted foundations in clay under transient and sustained concentric loading", Géotechnique 59 (6), 525-537.
- [27] Hansen, M.H. and L.C. Henriksen, "Basic DTU wind energy controller," DTU Wind Energy, Roskilde, Denmark, 2013.
- [28] Houslsby, G.T. and Byrne, B.W. (2005) 'Calculation procedures for installation of suction caissons in sand'. Geotech.Eng., 158(3):135-144.
- [29] J. Jonkman, S. Butterfield, W. Musial, and G. Scott, Definition of a 5-MW Reference Wind Turbine for Offshore System Development.
- [30] Li, L., Gao, Z. and Moan, T., 2013, "Joint Environmental Data At Five European Offshore Sites For Design Of Combined Wind And Wave Energy Devices". In: Proceedings of the 32nd International Conference on Ocean, Offshore and Arctic Engineering, OMAE2013-10156, June 9-14, Nantes, France.

- [31] Manolas D.I., R. V.A., S. V.G (2014). Assessing the importance of geometric non-linear effects in the prediction of wind turbine blade loads. *Computational and Nonlinear Dynamics Journal*, Vol. 10, 041008.
- [32] Manolas, D., "Hydro-aero-elastic analysis of offshore wind turbines," PhD Thesis, NTUA, Athens, 2015
- [33] D. Petot, "Differential Equation Modeling of Dynamic Stall, Recherché Aerospatiale, 1989, 5, 59–72.
- [34] Popko Wojciech et al, 2012, Offshore Code Comparison Collaboration Continuation (OC4), Phase I: Results of Coupled Simulations of an Offshore Wind Turbine with Jacket Support Structure. Trans. ISOPE, Journal of Ocean and Wind Energy, Vol 1, No 1, p. 1.
- [35] Randolph, M.F., Gourvenec,S. (2011), Offshore Geotechnical Engineering.
- [36] Reese L.C., Cox W.R. and Koop, F.D. (1974)'Analysis of laterally loaded piles in sand' Proc. Annu. Offshore Tech. Conf. Houston, Texas, Paper OTC 2080.
- [37] Riziotis, V.A., Voutsinas, S.G., Politis, E.S., Chaviaropoulos, P.K. (2004) "Aeroelastic stability of wind turbines: the problem the methods and the issue," J Wind Energy, 2004, 7, pp 373-392.
- [38] Riziotis, V.A., Voutsinas, S.G., Politis, E.S., Chaviaropoulos, P.K., (2008) "Stability analysis of pitch regulated, variable-speed wind turbines in closed loop operation using a linear eigenvalue approach," J Wind Energy, 2008, 11, pp 517-535.
- [39] Riziotis V.A. and Voutsinas S.G., (1997), "GAST: A general aerodynamic and structural prediction tool for wind turbines", EWEC'97 Dublin Ireland.
- [40] Robertson Amy et al, 2014. "Offshore code comparison collaboration, continuation within IEA wind task 30: phase II results regarding a floating semisubmersible wind system" OMAE 2014, San Francisco, USA.
- [41] Rosquoët F., Garnier J., Thorel L., Canepa Y., 2004, "Horizontal cyclic loading of piles installed in sand: Study of the pile head displacement and maximum bending moment", Proceedings of the International Conference on Cyclic Behaviour of Soils and Liquefaction Phenomena, Bochum, T. Triantafyllidis (Ed.), Taylor & Francis, pp 363-368.
- [42] Rosenblatt, M., Remarks on a multivariate transformation, Ann. Math. Statist., 23(3) (September 1952) 470-472.
- [43] Soukissian, T.H., G. Kalantzi, 2006, "Extreme value analysis methods used for wave prediction", Proceedings of the 16th International Offshore and Polar Engineering Conference, Vol. III, pp. 10-17, ISBN 1-880653-66-4
- [44] Soukissian, T.H., 2013, "Use of multi-parameter distributions for offshore wind speed modelling: The Johnson SB distribution", Applied Energy, Vol. 111, pp. 982-1000. doi: 10.1016/j.apenergy.2013.06.050
- [45] Soukissian, T.H., Tsallis, C., 2015, "The effect of the generalized extreme value distribution parameter estimation methods in extreme wind speed prediction", Natural Hazards, Vol. 78, pp. 1777-1809, Springer Netherlands, <http://dx.doi.org/10.1007/s11069-015-1800-0>
- [46] Thomas von Borstel (Ramboll), "D4.3.1 – Revision 1, Design Report – Reference Jacket," INNWIND.EU project, 2015.
- [47] Xiao-chen YANG, Qing-he ZHANG, 2013, "Joint probability distribution of winds and waves from wave simulation of 20 years (1989-2008) in Bohai Bay", Water Science and Engineering, 6 (3), pp. 296-307

Getting in touch with the EU

In person

All over the European Union there are hundreds of Europe Direct information centres. You can find the address of the centre nearest you at:

https://europa.eu/european-union/contact_en

On the phone or by email

Europe Direct is a service that answers your questions about the European Union. You can contact this service:

- by freephone: 00 800 6 7 8 9 10 11 (certain operators may charge for these calls),
- at the following standard number: +32 22999696 or
- by email via: https://europa.eu/european-union/contact_en

Finding information about the EU

Online

Information about the European Union in all the official languages of the EU is available on the Europa website at: https://europa.eu/european-union/index_en

EU publications

You can download or order free and priced EU publications at: <https://publications.europa.eu/en/publications>. Multiple copies of free publications may be obtained by contacting Europe Direct or your local information centre (see https://europa.eu/european-union/contact_en).

EU law and related documents

For access to legal information from the EU, including all EU law since 1952 in all the official language versions, go to EUR-Lex at: <https://eur-lex.europa.eu>

Open data from the EU

The EU Open Data Portal (<https://data.europa.eu/euodp/en/home>) provides access to datasets from the EU. Data can be downloaded and reused for free, for both commercial and non-commercial purposes.

In the Modular Jacket concept, the structural components of the offshore jacket will be designed as prefabricated sub-assemblies.

Feasible jacket design has been developed in selected 6 windfarm scenarios, ranging from 20m to 60m of water depth and considering wind turbines of both actual 8MW and near future 10 MW power. In view of prefabrication and modularity the components preliminary obtained (DK-joints, X-Joints, tubular) have been considered showing high degree of recurrence for X-joints and tubular in the range of OD600-700mm t=20-35mm for braces and OD1200-1400mm t= 45-50mm for legs.

Foundation analysis have been performed in view of possible application of suction caissons, a solution alternative to the standard piled foundation of increasing interest due to possible reduction of installation costs. Design charts have been developed for both traditional piled foundation and innovative suction caissons.

With the aim of investigate different prefabrication strategies incrementally automated processes, from semi-automatic to fully robotized welding, have been selected. Welding trials have been performed and the prefabricated components have been extensively tested both small scale and full scale in view of evaluate components quality and possible benefits from the structural point of view. In particular, the fatigue behaviour has been investigated since it is of particular impact of offshore structures design.

The AWS-WHB-B5.7 Cost Model has been applied for comparison on the basis of actual process parameters. The outcomes have been extended to the fabrication of a whole jacket leading to the evaluation of cost and time savings in a massive fabrication scenario.

